



GRADUATE SCHOOL
EAST TENNESSEE STATE UNIVERSITY

East Tennessee State University
Digital Commons @ East
Tennessee State University

Electronic Theses and Dissertations

Student Works

5-2020

Climate Variability from 1980 to 2018 and its Effect on Wind Directions, Wind Speeds, and Vog Dispersal in Hawaii

Monica Ayala
East Tennessee State University

Follow this and additional works at: <https://dc.etsu.edu/etd>

Recommended Citation

Ayala, Monica, "Climate Variability from 1980 to 2018 and its Effect on Wind Directions, Wind Speeds, and Vog Dispersal in Hawaii" (2020). *Electronic Theses and Dissertations*. Paper 3776. <https://dc.etsu.edu/etd/3776>

This Thesis - unrestricted is brought to you for free and open access by the Student Works at Digital Commons @ East Tennessee State University. It has been accepted for inclusion in Electronic Theses and Dissertations by an authorized administrator of Digital Commons @ East Tennessee State University. For more information, please contact digilib@etsu.edu.

Climate Variability from 1980 to 2018 and its Effect on Wind Directions,
Wind Speeds, and Vog Dispersal in Hawaii

A thesis

presented to

the faculty of the Department of Geosciences

East Tennessee State University

In partial fulfillment

of the requirements for the degree

Master of Science in Geosciences, Geospatial Analysis

by

Mónica Y. Ayala Díaz

May 2020

Dr. Andrew Joyner, Chair

Dr. Chris Gregg

Mr. William Tollefson

Dr. Ingrid Luffman

Keywords: climate variability, synoptic patterns, atmospheric patterns, vog, Hawaii, Hawai'i

ABSTRACT

Climate Variability from 1980 to 2018 and its Effect on Wind Directions,
Wind Speeds, and Vog Dispersal in Hawaii

by

Mónica Y. Ayala Díaz

Wind patterns in the Pacific Ocean fluctuate seasonally, annually, and decadal, resulting in changes in the dispersal of volcanic smog (vog) across the Hawaiian Islands. A variety of synoptic-scale weather patterns can affect the Islands, creating variability in the direction and intensity of wind patterns. Recent changes in wind profiles were analyzed to identify possible patterns that could influence and increase the dispersion of vog over time on Hawai'i Island and the other Hawaiian Islands to the northwest. Historically, Northeast Trade Winds prevailed for much of the year, shifting vog into the Pacific Ocean southwest of Hawaii and away from the state's principal population centers, but Northeast Trade Winds have shown a 20+% reduction over the past several decades. An increase in the southerly source of prevailing wind increased the frequency and intensity of vog and its impacts on the environment and health and well-being of people across the Islands.

Copyright 2019 by Mónica Y. Ayala Díaz

All Rights Reserved

DEDICATION

This thesis is dedicated to my family and friends that have supported and encouraged through these two years of work and study. Moreover, this is especially dedicated in honor of my paternal grandfather Rubén “Blanco” Ayala Verdejo who I miss dearly and who I always have in my thoughts.

ACKNOWLEDGMENTS

First, I want to give my sincere thanks to Dr. Andrew Joyner for keeping me motivated through the up and downs of this research. For helping me think through and question my results.

Then I want to give my heartfelt thanks to my fellow graduate students and friends Porcha McCurdy and Montana Kruske for always telling me to persevere and helping me work through problems. I want to give thanks to Jake Hansen for his immense help with ArcGIS Pro.

Finally, I want to give thanks to my friends and family that heard my frustrations and supported me in advancing through this stage of my life.

TABLE OF CONTENTS

ABSTRACT.....	2
DEDICATION.....	4
ACKNOWLEDGMENTS	5
TABLE OF CONTENTS.....	6
LIST OF TABLES.....	7
LIST OF FIGURES	9
CHAPTER 1. INTRODUCTION	12
Macro-scale Climate and Weather Patterns	12
El Niño Southern Oscillation.....	14
Pacifica Decadal Oscillation.....	19
Pacific/North American Teleconnection Pattern	21
West Pacific Teleconnection Pattern	22
Northeast Trade Winds	23
Kona Winds	24
Role of Topography on Local Wind Patterns	26
Volcanic Smog (vog)	29
Objectives and Research Questions	30
CHAPTER 2. DATA AND METHODS	32
Data Acquisition and Processing	32
Analysis.....	33
CHAPTER 3. RESULTS	38
CHAPTER 4. DISCUSSION.....	69
CHAPTER 5. CONCLUSIONS AND FUTURE RESEARCH	77
REFERENCES	79
APPENDICES	87
Appendix A: Acronyms	87
Appendix B: Supplemental Figures	89
VITA.....	101

LIST OF TABLES

Table 2.1. Teleconnection Index Names and Acronyms, Dataset used, Date Ranges, and Region they Cover.	33
Table 2.2. Wind Direction in their Degree and Cardinal Direction at 45° angles.	35
Table 3.1. Results of SPSS Spearman Correlation between All Teleconnections.....	48
Table 3.2. Results of SPSS OLS Regression between All Teleconnections and Hilo 1- and 2-Minute Wind Speed.	49
Table 3.3. Results of SPSS OLS Regression between All Teleconnections and Hilo 5-Seconds Wind Speed.	50
Table 3.4. Results of SPSS OLS Regression between All Teleconnections and Kona 2-Minute Wind Speed.	50
Table 3.5. Results of SPSS OLS Regression between All Teleconnections and Kona 5-Seconds Wind Speed.	51
Table 3.6. Results of a Multinomial Logistic Regression of Wind Direction for Hilo1+2 and All Teleconnection Indices in the Pacific. Red Indices showed significance for most of the 8-Cardinal Compass Directions.	52
Table 3.7. Results of a Multinomial Logistic Regression of Wind Direction for Hilo5 and All Teleconnection Indices in the Pacific. Red Indices showed significance for most of the 8-Cardinal Compass Directions.	52
Table 3.8. Results of a Multinomial Logistic Regression of Wind Direction for Kona2 and All Teleconnection Indices in the Pacific. Red Indices showed significance for most of the 8-Cardinal Compass Directions.	53
Table 3.9. Results of a Multinomial Logistic Regression of Wind Direction for Kona5 and All Teleconnection Indices in the Pacific. Red Indices showed significance for most of the 8-Cardinal Compass Directions.	53
Table 4.1. Results of Yearly Wind Direction for Hilo and Kona with predominant NE Direction Winds showing their days and percent. Red years showed an active El Niño event while blue years showed an active La Niña event. Light yellow highlights show 50% or more of predominant NE Winds in Kona. Dark yellow highlights show 30% or more of predominant NE Winds in Hilo.	74
Table 4.2. Results of Wind Direction in the active El Niño event years for Hilo and Kona with predominant NE Direction Winds showing their days and percent. Light yellow	

<p>highlights show 50% or more of predominant NE Winds in Kona. Dark yellow highlights show 30% or more of predominant NE Winds in Hilo.....</p>	75
<p>Table 4.3. Results of Wind Direction in the active La Niña event years for Hilo and Kona with predominant NE Direction Winds showing their days and percent. Light yellow highlights show 50% or more of predominant NE Winds in Kona. Dark yellow highlights show 30% or more of predominant NE Winds in Hilo.....</p>	75
<p>Table 4.4. Results of Wind Direction in the neutral ENSO years for Hilo and Kona with predominant NE Direction Winds showing their days and percent. Light yellow highlights show 50% or more of predominant NE Winds in Kona. Dark yellow highlights show 30% or more of predominant NE Winds in Hilo.....</p>	76
<p>Table 4.5. Results of 5-Year Interval Wind Direction for Hilo and Kona with prevailing NE Direction Winds.</p>	76

LIST OF FIGURES

Figure 1.1. The Niño Regions over the Pacific Basin.....	16
Figure 1.2. Region of the Pacific Decadal Oscillation over the northern Pacific basin, poleward from 20° North.	20
Figure 1.3. Map showing Kona Winds and Trade Winds over the Hawaiian Islands and the occurrence of wetter conditions on the Windward side of islands and dryer condition on the Leeward side. Infrequent Kona winds bring rain to the Leeward side.	25
Figure 1.4. Locations and elevations of the four southernmost most volcanoes on Hawai’i Island and weather stations at the two international airports. Contour interval is 200m.....	27
Figure 3.1. Wind roses for Hilo show 1-minute and 2-minute wind speeds and directions from 1980-2018 (A) and 5-second wind speeds and directions from 1998 to 2018 (B) based on the eight primary cardinal directions. Wind roses for Kona show 2-minute wind speeds and directions from 1998-2018 (C) and 5-second wind speeds and directions from 1999-2018 (D) based on eight primary cardinal directions.	39
Figure 3.2. Wind roses for Hilo showing 1-minute and 2-minute wind direction and wind speed observations subset into ~5-year time periods.....	41
Figure 3.3. Wind roses for Hilo showing 5-second wind direction and wind speed observations subset into ~5-year time periods (overlapping with the time periods in Figure 3.2)..	43
Figure 3.4. Wind roses for Kona showing 1-minute and 2-minute wind direction and wind speed observations subset into ~5-year time periods.....	45
Figure 3.5. Wind roses for Kona showing 5-second wind direction and wind speed observations subset into ~5-year time periods (overlapping with the time periods in Figure 3.4)..	47
Figure 3.6. Hilo WD1+2 from 1980-2018 shows the wind direction in comparison with the index. The primary y-axis (left) shows wind direction values in degrees and the secondary y-axis (right) shows the Niño3.4 index values while the date is shown on the x-axis. The Neutral threshold is at 30 according to the index value.....	54
Figure 3.7. Hilo WD1+2 from 1980-2018 shows the wind direction in comparison with the index. The primary y-axis (left) shows wind direction values and the secondary y-axis (right) shows the PNA index values while the date is shown on the x-axis. The Neutral threshold is at 30 according to the index value.....	55
Figure 3.8. Hilo WD1+2 from 1980-2018 shows the wind direction in comparison with the index. The primary y-axis (left) shows wind direction values and the secondary y-	

axis (right) shows the ONI index values while the date is shown on the x-axis. The Neutral threshold is at 30 according to the index value.....	55
Figure 3.9. Hilo WD1+2 from 1980-2018 shows the wind direction in comparison with the index. The primary y-axis (left) shows wind direction values and the secondary y-axis (right) shows the TNI index values while the date is shown on the x-axis. The Neutral threshold is at 30 according to the index value.....	56
Figure 3.10. Hilo WD5 from 1998-2018 shows the wind direction in comparison with the index. The primary y-axis (left) shows wind direction values and the secondary y-axis (right) shows the Niño3.4 index values while the date is shown on the x-axis. The Neutral threshold is at 30 according to the index value.....	57
Figure 3.11. Hilo WD5 from 1998-2018 shows the wind direction in comparison with the index. The primary y-axis (left) shows wind direction values and the secondary y-axis (right) shows the PNA index values while the date is shown on the x-axis. The Neutral threshold is at 30 according to the index value.....	58
Figure 3.12. Hilo WD5 from 1998-2018 shows the wind direction in comparison with the index. The primary y-axis (left) shows wind direction values and the secondary y-axis (right) shows the ONI index values while the date is shown on the x-axis. The Neutral threshold is at 30 according to the index value.....	58
Figure 3.13. Hilo WD5 from 1998-2018 shows the wind direction in comparison with the index. The primary y-axis (left) shows wind direction values and the secondary y-axis (right) shows the TNI index values while the date is shown on the x-axis. The Neutral threshold is at 30 according to the index value.....	59
Figure 3.14. Kona WD2 from 1998-2018 shows the wind direction in comparison with the index. The primary y-axis (left) shows wind direction values and the secondary y-axis (right) shows the Niño3.4 index values while the date is shown on the x-axis. The Neutral threshold is at 30 according to the index value.....	60
Figure 3.15. Kona WD2 from 1998-2018 shows the wind direction in comparison with the index. The primary y-axis (left) shows wind direction values and the secondary y-axis (right) shows the PNA index values while the date is shown on the x-axis. The Neutral threshold is at 30 according to the index value.....	61
Figure 3.16. Kona WD2 from 1998-2018 shows the wind direction in comparison with the index. The primary y-axis (left) shows wind direction values and the secondary y-axis (right) shows the ONI index values while the date is shown on the x-axis. The Neutral threshold is at 30 according to the index value.....	61
Figure 3.17. Kona WD2 from 1998-2018 shows the wind direction in comparison with the index. The primary y-axis (left) shows wind direction values and the secondary y-axis	

	(right) shows the TNI index values while the date is shown on the x-axis. The Neutral threshold is at 30 according to the index value.....	62
Figure 3.18.	Kona WD5 from 1998-2018 shows the wind direction in comparison with the index. The primary y-axis (left) shows wind direction values and the secondary y-axis (right) shows the Niño3.4 index values while the date is shown on the x-axis. The Neutral threshold is at 30 according to the index value.....	63
Figure 3.19.	Kona WD5 from 1998-2018 shows the wind direction in comparison with the index. The primary y-axis (left) shows wind direction values and the secondary y-axis (right) shows the PNA index values while the date is shown on the x-axis. The Neutral threshold is at 30 according to the index value.....	64
Figure 3.20.	Kona WD5 from 1998-2018 shows the wind direction in comparison with the index. The primary y-axis (left) shows wind direction values and the secondary y-axis (right) shows the ONI index values while the date is shown on the x-axis. The Neutral threshold is at 30 according to the index value.....	64
Figure 3.21.	Kona WD5 from 1998-2018 shows the wind direction in comparison with the index. The primary y-axis (left) shows wind direction values and the secondary y-axis (right) shows the TNI index values while the date is shown on the x-axis. The Neutral threshold is at 30 according to the index value.....	65
Figure 3.22.	Graph for Hilo WS1+2 from 1980-2018 shows wind speed in miles per hour (mph) with linear trendline and R-square in the upper right corner.....	66
Figure 3.23.	Graph for Hilo WS5 from 1998-2018 shows wind speed in miles per hour (mph) with linear trendline and R-square in the upper right corner.....	67
Figure 3.24.	Graph for Kona WS2 from 1998-2018 shows wind speed in miles per hour (mph) with linear trendline and R-square in the upper right corner.....	67
Figure 3.25.	Graph for Kona WS5 from 1999-2018 shows wind speed in miles per hour (mph) with linear trendline and R-square in the upper right corner.....	68

CHAPTER 1. INTRODUCTION

Wind patterns in the Pacific Ocean fluctuate seasonally, annually, and decadal, resulting in changes in volcanic smog (vog) dispersion across the Hawaiian Islands. Vog is a volcanic hazard that causes hazy air pollution originating from volcanic eruptions on Hawai'i Island and is easily carried by wind currents. A variety of synoptic-scale weather patterns can affect the Islands, creating variability in the direction and intensity of wind patterns.

Atmospheric patterns have recently shown changes in their dynamics, such as a reduction in the dominant Northeast Trade Winds. To better understand impacts on the frequency of wind speed and direction in the Hawaiian Islands, global/regional-scale atmospheric patterns are examined along with more local-scale patterns and topographic influences. Intra- and inter-annual temporal trends are analyzed to test possible relationships with atmospheric patterns and other potential climatological changes that may influence vog dispersion and, consequently, the health and well-being of Hawaiian residents.

Macro-scale Climate and Weather Patterns

Changes in climate and weather patterns occur around the world with many regions experiencing increased extreme event frequencies (e.g., droughts, floods, etc.) and temperature anomalies. In the Pacific Ocean, vast wind fields and circulation patterns drive short- and long-term trends (Wyrski and Meyers, 1976). The mid-latitude westerlies and low latitude easterly trade winds are the most dominant prevailing global wind patterns. Trade winds are the result of Earth's rotation, which causes the wind to move in a southwest direction in the northern hemisphere, and a northwest direction in the southern hemisphere. For both hemispheres, trade winds move towards the equator because of the deflecting force caused by the Coriolis Effect (Burstyn, 1966). These atmospheric wind patterns influence other major processes, including

oceanic circulation patterns (i.e., thermohaline circulation) and the displacement of high- and low-pressure systems (Wunsch, 2002). In a 60° belt across the equator (from 30° North to 30° South) these curved prevailing winds (trade winds) flow generally from east to west (i.e., from the northeast in the Northern Hemisphere and southeast in the Southern Hemisphere).

Teleconnections patterns refer to macro-scale pressure and atmospheric circulation anomalies in various regions of the world, covering large geographic areas. These patterns exhibit variability over a range of temporal scales, with ‘phases’ or anomalies occurring over days, weeks, months, years, and even decades, resulting in fluctuations in intra/inter-annual and/or intra/inter-decadal weather patterns. They often influence local climatic responses in various regions (e.g., Hansen and Mavromatis, 2001; Hardy and Henderson, 2013; Casanueva-Vicente et al., 2014; Zhu and Li, 2016). Moreover, they reflect changes in the jet stream and atmospheric circulation “wave” oscillations, which in turn can affect storm tracks, the intensity of the jet stream, air pressure, rainfall, temperature, and wind, among others. Some teleconnections can span entire ocean basins and continents and are referred to as planetary-scale. All teleconnections exhibit positive and negative phases that differ from one another in atmospheric geopotential height, location, pressure, intensity, variability, etc. In the Pacific Ocean, a variety of different teleconnections are present, however the El Niño Southern Oscillation (ENSO) pattern is the most well-known and predominant with various oceanic time-series and indices developed for analysis (e.g., Niño 3.4 Index, Niño 4 Index, Multivariate ENSO Index V2, Bivariate ENSO Time Series, Oceanic Niño Index, and Trans-Niño Index). The Pacific Decadal Oscillation (PDO) is also analyzed using an oceanic time series, while the Pacifica/North America (PNA) and West Pacific (WP) patterns are analyzed using atmospheric time-series.

Various datasets and models are used to construct indices and time series. These include the International Comprehensive Ocean-Atmosphere Data Set (ICOADS), National Center of Environmental Prediction (NCEP)/ National Center of Atmospheric Research (NCAR) Reanalysis 1 (R1) model, and Hadley Center sea ice and sea surface temperature (SST) model (HadISST). Datasets and models can be found in variety of versions, scales, and time periods. The ICOADS represents the most extensive dataset, extending from 1800 to the present. The majority of the datasets have a global coverage (in grid format) and data subsets are available from the National Oceanic and Atmospheric Administration's (NOAA) Physical Science Division (PSD) or Climate Prediction Center (CPC) websites (<https://www.ncep.noaa.gov/>; <https://www.cpc.ncep.noaa.gov/>).

El Niño Southern Oscillation

El Niño Southern Oscillation is a periodic fluctuation with more distinct seasonal to inter-annual global climate variations (Klaus and Timlin, 2011). Longer fluctuations can span two to seven-year intervals and the index can indicate anomalies in air pressure and sea surface temperature (SST). Monitoring of the ENSO focuses on SST anomalies with the Southern Oscillation Index (SOI) being one of the first standardized indices for observing the sea level pressure differences in the Pacific. Impacts from the ENSO occur throughout the year, but it was originally identified because of its effects in the east Pacific on equatorial South America with changes in water temperature and upwelling (Tedeschi et al., 2016; Wyrtki, 1975). In contrast, sea level barometric pressure (i.e., the force exerted by the atmosphere at sea level or zero meters elevation) fluctuations between stations at Tahiti, French Polynesia and Darwin, Australia are influenced by the Southern Oscillation indicating bimodal variations (Allan et al., 1991). Moreover, the SOI can measure and quantify these pressure differences.

The ENSO teleconnection spans the equatorial Pacific Ocean region, however its effects in the Pacific can affect the outcomes in the Atlantic Ocean and other regions due to the wide area covered by the anomalies (e.g., Herceg Bulić and Kuckarski, 2007; Ralph et al., 2003; Smith et al., 2007; Whan and Zwiers 2017). The changes in SST can be of $\pm 3^{\circ}\text{C}$ ($\sim 6^{\circ}\text{F}$), which can have major impacts on global weather patterns. Usually when Darwin exhibits a low-pressure zone and Tahiti exhibits a high-pressure zone the atmospheric circulation flows east to west. This causes a westward flow of the warm surface water generating rain in the western Pacific, including Australia. This particular process, if strong, is associated with a La Niña event. The ENSO varies between positive (warm) and negative (cool) events/phases, termed El Niño or La Niña. In an El Niño event, the trade winds weaken and cause warm surface water to build up in the eastern Pacific basin. Conversely, for a strong El Niño event to occur the pressure difference between Darwin and Tahiti must weaken, which often causes parts of the western Pacific to experience harsh drought conditions (especially Australia) (Chiew et al., 1998; Wang and Hendon, 2007). This in turn can generate heavy rainfall in parts of equatorial South America (mainly the west coast) (Grimm and Tedeschi, 2009). These processes are extremely dependent on each other (i.e. if trade winds strengthen or weaken it can affect the pressure gradient which in turn affects SST, which can impact pressure gradients as well). The pressure gradient is the change in air pressure over distance, thus if this gradient is strong then airflow is faster between high- and low-pressure areas. According to Trenberth (1997), El Niño occurs approximately 31% of the time compared to La Niña, which occurs 23% of the time.

The ENSO is divided in regions, first designated by dividing the regions in four over the equatorial Pacific from the longitudes 160° East to 80° West (Rasmusson and Carpenter, 1982) (Figure 1.1). Moreover, the wide variety of ENSO indices and time-series calculate specific

aspects and regions of this global atmospheric circulation pattern. The first region is Niño 1+2, which is recognized as “the traditional Niño region along the South American coast” and is the only region where the range of study is South of the Equator (Trenberth and Stepaniak, 2001). The second region is Niño 3, which has been used extensively for analysis and predictions of ENSO, however more recent data indicate that the ENSO interactions span further west than the region encompasses (Trenberth, 1997). The third region is the Niño 4 which covers the central equatorial Pacific. The last region is Niño 3.4, a composite of portions from the Niño 3 and Niño 4 regions. For the purpose of this research, the focus will be on regions 3.4 and 4.

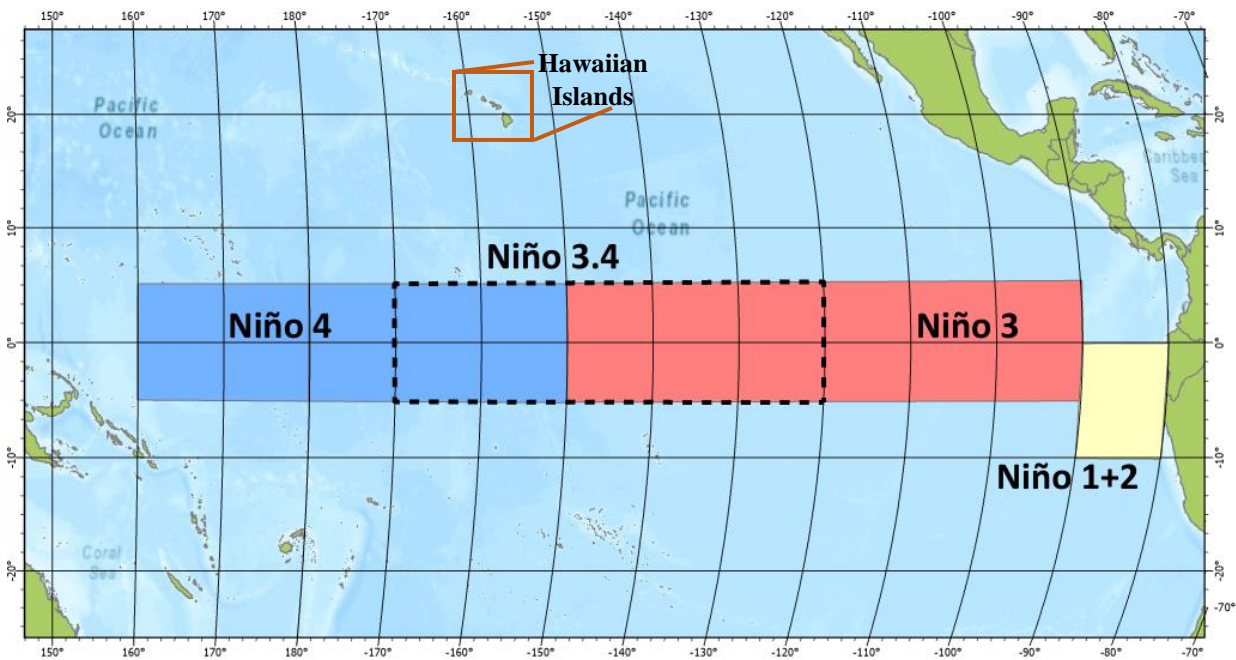


Figure 1.1. The Niño Regions over the Pacific Basin.

Barnston et al. (1997) established the Niño 3.4 region by analyzing the SSTs in the area comprising portions of region 3 and region 4 which maximizes the ENSO signal and makes this the preferred time-series currently used by the majority of researchers. This region encompasses the areas from longitude 170° West to 120° West and latitude 5° South to 5° North in the equatorial Pacific, essentially the East Central Tropical Pacific. For this time-series, if SST

anomalies are $\geq 0.5^{\circ}\text{C}$ (0.9°F) this is characteristic of warm phase conditions (El Niño/positive), but if the reverse SST anomalies are $\leq -0.5^{\circ}\text{C}$ (-0.9°F) then this is characteristic of cool phase conditions (La Niña/negative). This is a recognized threshold for this time-series and it is a standard used for most ENSO studies (NCEI, 2020). Moreover, the Niño 3.4 time-series is calculated using the HadISST version 1 (HadISST1) dataset. Data for the Niño 3.4 time-series spans from 1870 CE to the present.

Essentially, the Niño 4 analyzes SST anomalies. This region encompasses the areas from longitudes 160° East to 150° West and latitudes 5° South to 5° North, covering the central Equatorial/Tropical Pacific (Trenberth, 1997; Trenberth and Stepaniak, 2001). The region that Niño 4 covers tends to have less variance compared to the other regions of El Niño. These time-series calculations use the HadISST1 dataset. The Niño 4 dataset covers a time period from 1950 to the present. This time-series is used to analyze the Trans-Niño Index (TNI) in conjunction with the Niño1+2 index (Trenberth and Stepaniak, 2001; NCEI, 2020). The Niño 4 index is considered a better option to define the La Niña events compared to the Niño 3.4 index based on SST anomalies in the area (Trenberth and Stepaniak, 2001; NCEI, 2020). In this region it is typical to have SSTs at or above the threshold (-0.5°C), therefore indicating a deep convection annually in the tropical Pacific. An anomaly in SSTs of -0.5°C in this region can cause water temperatures to be below the standard threshold, resulting in a major westward flow. This westward flow is the origin of the deep convection in the tropical Pacific basin. The westward flow is associated with the Darwin and Tahiti pressure difference with Darwin having a low-pressure zone and Tahiti a high-pressure zone (Trenberth and Stepaniak, 2001; NCEI, 2020).

The Oceanic Niño Index (ONI) analyzes SSTs in the region from longitudes 170° West to 120° West and latitudes 5° South to 5° North in the equatorial Pacific, which is the same region

as the Niño 3.4 (NCEI, 2020). A peculiar aspect of this index is that it is closely dependent on the Niño 3.4 SST anomalies. The time-series uses averaged SST anomalies over a three month-period that ends with the current month and gives a resulting value for the ONI. However, if the ONI displays five consecutive values with warm or cool phase conditions, then this indicates an El Niño or La Niña event. The ONI data cover a period from 1950 to the present. This time-series has the same threshold as Niño 3.4, which is of $\pm 0.5^{\circ}\text{C}$ (0.9°F).

The Transitional "Trans" Niño Index is a dataset that calculates the ENSO using the HadISST and the NCEP (National Center for Environmental Prediction) OI (Optimum Interpolation) SST datasets (Trenberth and Stepaniak, 2001). This index uses the normalized SST anomalies averaged in differences between the Niño 1+2 region (latitude: 0° South to 10° South, longitude: 90° West to 80° West) and Niño 4 (latitude: 5° South to 5° North, longitude: 170° West to 120° West) (Trenberth and Stepaniak, 2001). This is due to the Niño3.4 being “approximately thought as the sum of these two indices, N3.4 and TNI are approximately orthogonal at zero lag” (Trenberth and Stepaniak, 2001). This time-series measures the SST gradient between the central (Niño 4) and eastern equatorial (Niño 1+2) Pacific (Trenberth and Stepaniak, 2001). If results for this are large (positive) values, it signifies that the Niño 1+2 has negative values and the Niño 4 has positive values meaning this is a “central Pacific El Niño” event. The opposite happens if TNI has negative values, which marks a “central Pacific La Niña” event. This index covers a period from 1870 CE to the present.

The Bivariate ENSO Time-series (BEST) is modeled to analyze long periods of the ENSO teleconnection phases. This time-series incorporates the often neglected atmospheric portions that the Niño 3.4 does not measure in the eastern tropical Pacific; this is done by adding the SOI that measures the pressure differences between Darwin and Tahiti (Smith and

Sardeshmukh, 2000). The values for both time-series (Niño 3.4 and SOI) must initially be standardized by month. The standardization has to be calculated separately to have a mean of zero and a standard deviation of one. This process should include the entirety of the period that is being analyzed before adding the SST values of the Niño 3.4 and pressure values from the SOI (Smith and Sardeshmukh, 2000). These processes result in the BEST time-series; however, the values for the index must be averaged first for each month before running a mean over a three- or five-month period (Smith and Sardeshmukh, 2000). This index covers a period from 1870 CE to the present.

The Multivariate ENSO Index Version 2 (MEI V2), in contrast to other datasets, focuses on combining five variables (sea level pressure (SLP), SSTs, surface zonal winds (U), surface meridional winds (V), and Outgoing Longwave Radiation (OLR)) and then creates a single dataset to calculate the ENSO. Wolter and Timlin (1993) developed the original MEI by acquiring data from marine ship observations derived from the Comprehensive Ocean-Atmosphere Data Set (COADS) records, now is known as the International COADS (ICOADS). The original MEI calculations used six variables related to ocean-atmosphere conditions that included SSTs and near-surface air temperature (Wolter and Timlin, 1998). This index analyzes and monitors the Tropical Pacific and has data from 1979 to the present.

Pacifica Decadal Oscillation

A teleconnection pattern that has a long duration with comparable climate and weather impacts to ENSO is the Pacific Decadal Oscillation (PDO), which spans a region from North America across the northern Pacific Ocean (Mantua et al., 1997). The phases, or modes, for this teleconnection can last 20-30 years, however the short observational record of the time-series makes it difficult to define specific aspects of the PDO (Deser et al., 2012; Mantua et al., 1997).

PDO variability is centered in the northern Pacific basin, covering an area poleward of 20° North, but it is strongly correlated with patterns in the tropical and southerly regions of the Pacific Ocean (Mantua and Hare, 2002). Modes of the PDO are identified by SST anomalies towards the tropical and northeast Pacific Ocean, with warm and cool anomalies indicative of each phase. Both SSTs and sea level pressure (SLP) are used to analyze the PDO. According to Mantua and Hare (2002), the positive (warm) phase is associated with below-average SLP that spans the North Pacific along with warm SSTs across the North American Pacific coast and cool western North Pacific SSTs. This process is reversed during the negative (cool) phase with cool SSTs along the North America Pacific coast and above-average SLP that spans the North Pacific with warm western North Pacific SSTs.

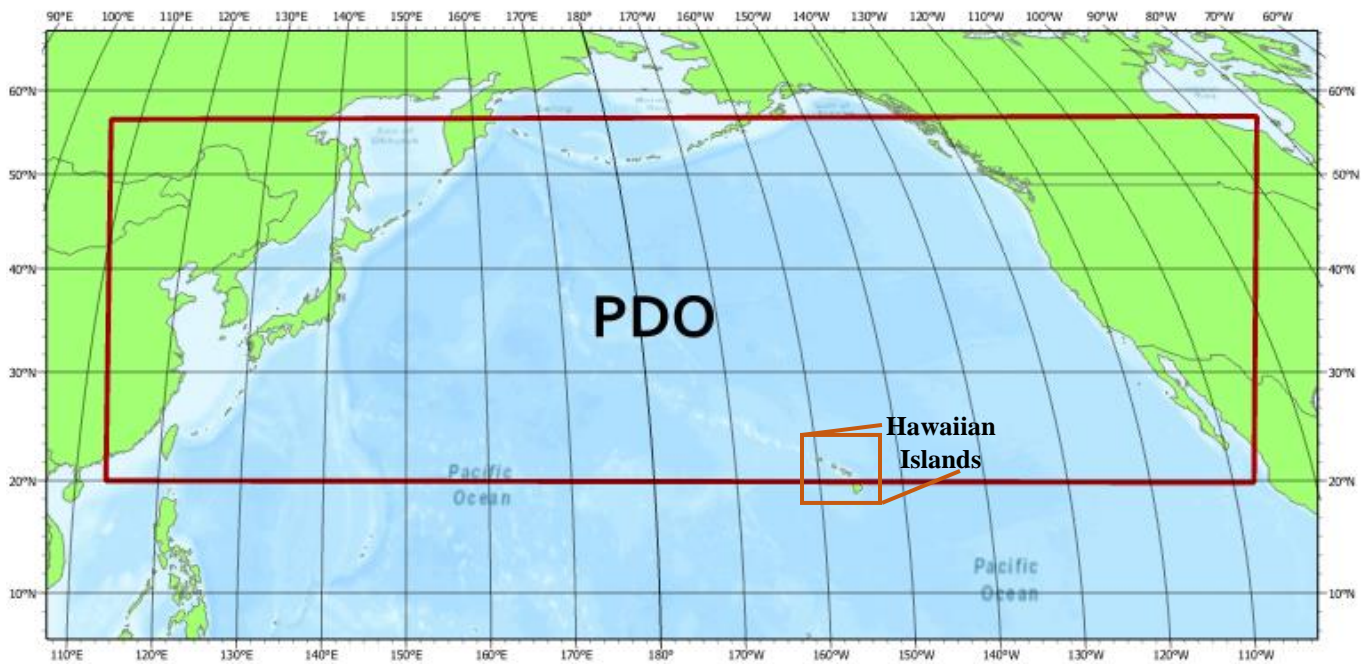


Figure 1.2. Region of the Pacific Decadal Oscillation over the northern Pacific basin, poleward from 20° North.

Pacific/North American Teleconnection Pattern

As the name implies, the Pacific/North American (PNA) teleconnection pattern is located in that region. This teleconnection is one of the most noticeable in the extra-tropics of the Northern Hemisphere, with a low-frequency variability. Strong fluctuations in the intensity and location of the East Asian jet stream are associated with the PNA (Franzke et al., 2011). The PNA's positive phase is represented by an intensified East Asian jet stream displaced eastward and exiting towards the western United States. In the intermountain region of North America and near Hawaii, the positive phase of the PNA teleconnection exhibits an above-average height. The negative phase has a westward retraction of the jet stream toward eastern Asia, which blocks a portion of the activity in the high latitudes of the North Pacific and causes a strong split-flow in the central North Pacific (Franzke et al. 2011). The PNA tends to be associated with the ENSO because its positive phase correlates with El Niño and its negative phase correlates with La Niña.

The Rotated Principal Component Analysis (RCPA) is used to identify and analyze major teleconnection patterns in the Northern Hemisphere including the North Atlantic Oscillation (NAO) and the PNA. Developed and used by Barnston and Livezey (1987), this method isolates major macroclimatic patterns for every month to then create a time-series for the teleconnection. The monthly mean is analyzed, which is standardized by 500 millibars (mb) height anomalies. The pressure anomalies are obtained from the Climate Data Assimilation System (CDAS) for the region poleward of 20° North latitude; these are standardized for the base period monthly means and standard deviations. In this research, the base period encompasses January 1980 to December 2018. Moreover, the RCPA analysis is based on the entire flow field and not on specific locations for height anomalies.

West Pacific Teleconnection Pattern

The West Pacific (WP) teleconnection is another Northern Hemisphere pattern and it is analyzed with the RCPA procedure as well. The WP teleconnection influences temperature and precipitation anomalies. According to Wallace and Gutzler (1981) and Barnston and Livezey (1987), this pattern shows a low-frequency variability spanning the North Pacific in all months of the year. However, in the winter and spring seasons, the teleconnections display North-South dipole anomalies with two centers: one over the Kamchatka Peninsula and the other over portions of southeast Asia and the western subtropical North Pacific. From the winter to summer seasons, the anomalies are associated with a strong northward shift that is equivalent to the prevalent northward shift of the East Asian jet stream or Pacific jet stream. Consequently, strong positive or negative phases for this teleconnection are linked to zonal and meridional variations with changes in intensity and locations in the area of the East Asian jet stream (Barnston and Livezey, 1987). The WP positive phase affects different locations with different anomalies. Higher latitudes of the Northern Hemisphere observe above-average annual precipitation, while in the winter and spring seasons below-average precipitation spans over the mid-latitudes of the North Pacific Ocean. Furthermore, in lower latitudes of the western North Pacific above-average temperatures in the winter and spring seasons are detected, while in eastern Siberia below-average temperatures are detected throughout all seasons. The WP index is analyzed using the RCPA method at 500mb and the National Center of Environmental Prediction (NCEP)/ National Center of Atmospheric Research (NCAR) Reanalysis 1 dataset (<https://www.esrl.noaa.gov/psd/data/gridded/data.ncep.reanalysis.html>).

Northeast Trade Winds

Trade winds are synoptic-scale atmospheric winds flowing from east to west generally in the tropics. The trade winds are located in a region between the horse latitudes and equator; the horse latitudes encompass an area between 30° North and 30° South. This wind field is considered one of the most constant around the globe with yearly trades having minimum variation (Wyrtsky and Meyers, 1976). Northeast (NE) trade winds, when blowing over or between the Hawaiian Islands, can have a speed of 5-20 knots (kn) (5.7-23 miles per hour (mph)), which is faster than average wind speeds over the open ocean (Chen and Nash, 1994; Schroeder, 1993). Conversely, these trade winds are affected by the semi-permanent North Pacific high-pressure zone, also known as the subtropical high-pressure ridge, located to the northeast of the Hawaiian Islands (Daingerfield, 1921; Garza et al., 2012). According to Wyrtsky and Meyers (1976), in the Pacific Ocean the main wind fields are the NE trades and the Southeast (SE) trades with the NE trades having less overall coverage area compared to the SE trades. Respectively, each trade wind field is at their strongest when each is in their corresponding spring and winter seasons. Compared to the SE trade winds, the NE trade winds are stronger but cover a smaller area (Wyrtsky and Meyers, 1976). Northeast trade winds are influenced by climatic events such as ENSO, PDO, and others (Garza et al., 2012). Schroeder (1993) claims that the east to northeast trade winds have an approximate wind speed of 4-10 meters per second (m s^{-1}) (8.9-22 mph) that is constant during the year (about 70% of the time); the dominance is especially strong during the summer (e.g., 92% of winds in August are within this wind speed range). The trades are slightly stronger in winter seasons as well (Kauahikaua and Tilling, 2014).

A trade wind inversion layer is recognized to be present at approximately 2 km above sea level (ASL) (Chen and Nesh, 1994). This inversion layer is, also, known as a thermal inversion layer. This layer divides an area where air temperature increases or remains constant with increasing altitude, which is contrary to the normal pattern of temperature change with altitude gain. Moreover, this thermal inversion can block atmospheric flow and trap pollution, in other words, it separates wind directions above and below 2 kilometers (km) (Schroeder, 1993). Upper level winds at this height are variable and they do not always follow the same wind direction patterns as the dominant surface level trade winds.

Kona Winds

“Kona” Winds are a term given by Hawaiian residents when prevailing winds are from the opposite direction to the trade winds. These are otherwise known as southerly or southwesterly winds and they influence local and regional weather patterns across the Hawaiian Islands (Daingerfield, 1921). Kona is a word of Polynesian origin that means “leeward”. However, Kona Winds are given their name when the typically leeward side becomes the windward side (Daingerfield, 1921). In Hawaii, the windward eastern side of the Islands is wetter with much higher annual rainfall compared to the western leeward side, which is generally drier. Some areas on the windward side of Hawai’i Island receive over 200 inches of rain annually, while some areas on the leeward side receive less than 10 inches of rain annually (<http://climate.geography.hawaii.edu/>).

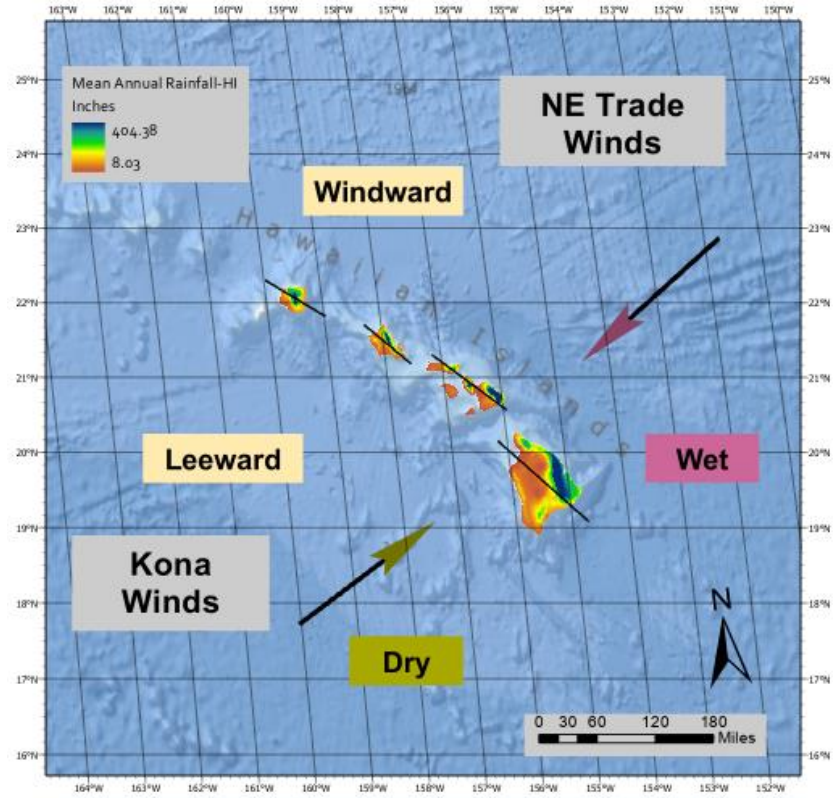


Figure 1.3. Map showing Kona Winds and Trade Winds over the Hawaiian Islands and the occurrence of wetter conditions on the Windward side of islands and dryer condition on the Leeward side. Infrequent Kona winds bring rain to the Leeward side.

Kona Winds on the island of O‘ahu are considered “volcano weather” due to the wind pattern generating increased precipitation conditions and hazy conditions at times due to the presence of vog during volcanic eruptions on the Island of Hawai‘i (Lyons, 1899). These Kona Winds strengthen when the subtropical high-pressure zone in the NE weakens typically in the winter months (Daingerfield, 1921). This indicates a reversal in the pressure gradient in the area (Daingerfield, 1921). Nevertheless, the strengthening of the Kona Winds is dependent on another pressure system—namely the nearly permanent Aleutian low-pressure zone located in the northwest Pacific (Daingerfield, 1921).

Role of Topography on Local Wind Patterns

Hawai'i Island is a volcanic island located in the North Pacific Ocean and is part of the Hawaiian Islands Chain, located approximately between 19° North to 22° North and 154° West to 160° West (Garza et al., 2012). These islands are located in the southwest and south of the widely known subtropical high-pressure zone, resulting in persistent NE trade winds over the islands in the summer season and variable winds in the winter season (Daingerfield, 1921; Garza et al., 2012). Disturbances during the winter season are caused by various synoptic phenomena such as mid-latitude frontal systems and Kona storms, among others (Garza et al., 2012).

Hawai'i Island, otherwise known as the “Big Island” due to its large size compared to the remaining occupied islands (Maui, Moloka'i, Kaho'olawe, O'ahu, Kaua'i and Ni'ihau), is located at 19°34'North 155°30'West and consists of five subaerially exposed volcanoes (Kīlauea, Mauna Loa, Hualālai, Mauna Kea, and Kohala). Only three of the volcanoes are currently considered active (Kīlauea, Hualālai, and Mauna Loa). The island has a diameter of approximately 140 km with topography dominated by its shield volcanoes (Yang et al., 2008). The last major volcanic activity on Hawai'i Island was from Kīlauea volcano, when 24 fissures opened along the volcano's Lower East Rift Zone from May to August, 2018. During this time there was also collapse of the summit region of the volcano and demise of a lava lake that was active since 2008. The highest elevations on the island are the summits of Mauna Kea with an elevation of 13,796 feet (ft) (4,205 meters (m)) ASL and Mauna Loa with an elevation of 13,681 ft (4,170 m) ASL (GVP, 2013b; GVP, 2013c). Moreover, these two volcanic peaks are above the trade wind inversion layer and cause orographic blocking (Cheng and Feng, 2001). Additionally, Mauna Loa covers approximately half of the surface area of the island.

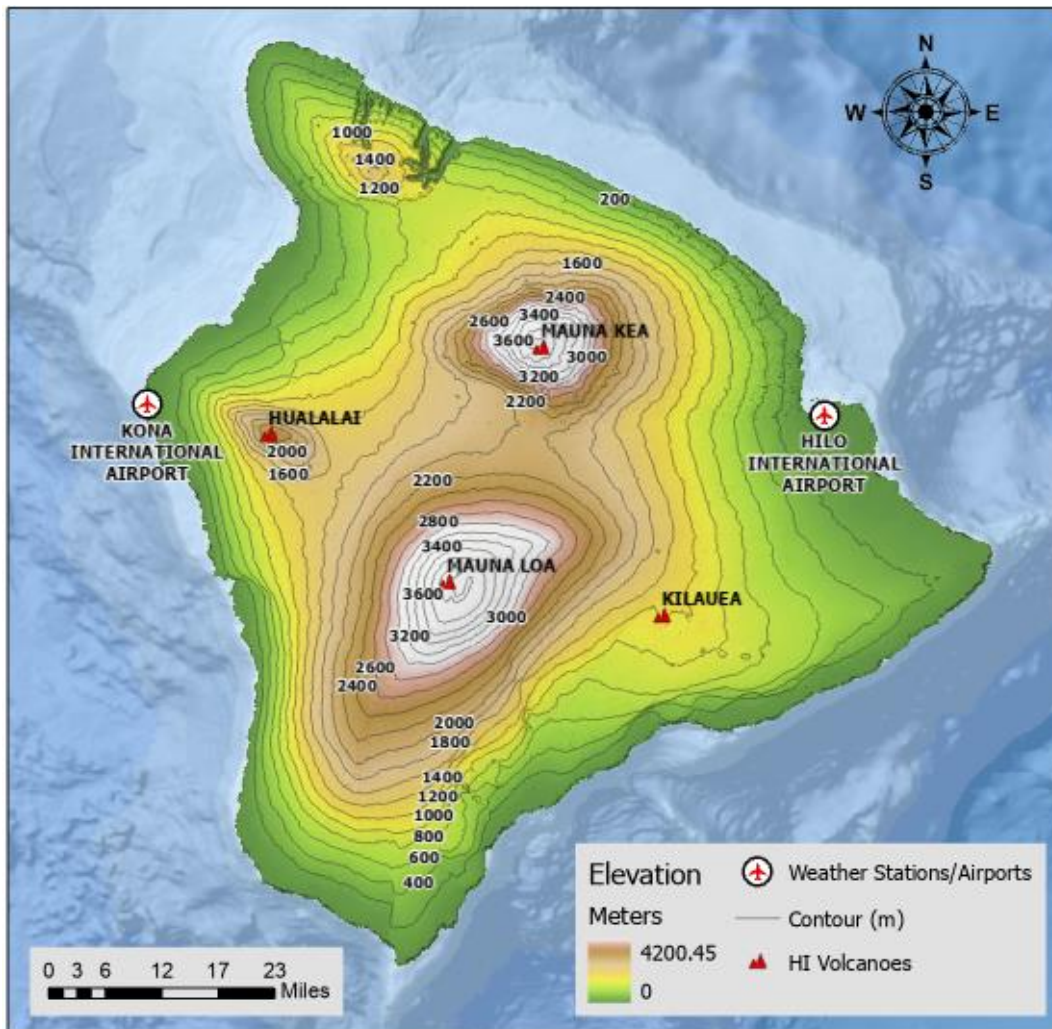


Figure 1.4. Locations and elevations of the four southernmost most volcanoes on Hawai'i Island and weather stations at the two international airports. Contour interval is 200m.

Volcanic eruptions are largely driven by the gas phase in magmas and may be explosive or effusive, or both. Pyroclasts erupted during explosive volcanism may span grain sizes ranging from ash (<2 millimeters (mm)) to lapilli (2-64mm) and larger blocks and bombs (>6mm). However, for this research the focus will be on volcanic gas emissions, which occur during both effusive and explosive volcanism. The gasses can vary in composition and can accompany an eruption or precede it (Kauahikaua and Tilling, 2014). Importantly, the majority of Mauna Loa's vents are above 2 km (2000 m) while Kilauea vents are all at or below the summit (1.2 km ASL, 4,009 ft ASL) (Kauahikaua and Tilling, 2014).

Volcanic emissions of gasses during effusive and explosive eruptions are then circulated in the atmosphere and, depending on the wind patterns and topography, these can be broadly dispersed (Kauahikaua and Tilling, 2014; Sutton et al., 2000). According to Swanson et al. (2011), plume emissions that are below 2 km are typically dispersed to the southwest by the NE trade winds. In contrast, if the plume emissions occur above 2 km, these are normally dispersed east and/or northeast by the jet stream. This is associated with the trade wind inversion layer located approximately 2 km ASL.

Compared to the other islands in Hawaii, Hawai'i Island experiences flow splitting of the trade winds that is attributed to the topography of the island, where trade winds move around the island (Garza et al., 2012; Chen and Nash, 1994). Due to the mountain heights being above the common height of trade wind inversions (approx. 2 km) wind flow below 2 km is forced to split on the windward side and move around the island (Yang et al., 2008). However, two counter-rotating vortices (“eddy” currents) to the leeward side of the Kona coast from the dominant flow of the NE trade winds cause a massive wake in that area that is unable to drift over Mauna Loa and Mauna Kea (Yang et al., 2008). This “eddy” current allows vog to be dispersed north along the Kona coast. In this pattern the vog drifts clockwise from Kīlauea to the south of Mauna Loa and up the west (Kona) side and toward Maui, O‘ahu and Kaua‘i.

Mauna Loa volcano erupts more frequently than Kīlauea, most recently in 1984. Similar to gasses erupted at Kilauea, emissions from Mauna Loa have also been reported throughout the entire island chain. The gas emission distribution is attributed to emittance above 2 km and above the inversion layer, which causes the gasses to be propelled northeast (Kauahikaua and Tilling, 2014). After the volcanic gas emissions drift below 2 km, these are then propelled back to the islands by the NE trade winds (Kauahikaua and Tilling, 2014).

Volcanic Smog (vog)

The term “pyroclast” can be applied to air fall deposits and pyroclastic flow and surge deposits (Schmid, 1981). Pyroclastic deposits are an accumulation of pyroclasts that can be unconsolidated (tephra) or consolidated (pyroclastic rock) (Schmid, 1981). Pyroclasts are erupted during explosive and effusive volcanism are generally referred to as “tephra” and particles with a grain size of <2mm (2000 micrometers (μm)) in diameter are characterized as volcanic ash (Horwell and Baxter, 2006). Particulate matter (PM) <2.5 μm is finer than a human hair (Camara and Lagunzad, 2011) and combines with a variety of volcanic gasses to create vog (e.g. sulfuric acid aerosols, sodium sulfate, and sulfur compounds, among other chemicals) (Camara and Lagunzad, 2011). The volcanic gas emissions of Kīlauea volcano are composed primarily of water vapor (H_2O), carbon dioxide (CO_2), and sulphur dioxide (SO_2). SO_2 emissions accompany all eruptions however vog contains these gas and acid particles with toxic contaminants such as ozone and hydrocarbons that are easily transportable by the wind (Poland et al., 2014). Vog can result in acid rain due to interactions with the atmosphere and cause damage to agricultural crops (Poland et al., 2014). Additionally, Sutton et al. (2000), reported that this acid rain “can leach lead from metal roofs into household water supplies”, and that in 1988 some 40% of residential drinking water sources on rain catchment systems in the Kona Districts were contaminated (Elias and Sutton, 2017).

Some of the major health hazards due to long-term exposure of vog is concurrent pulmonary effects, which include: sore throat, cough, breathlessness; and eye symptoms such as irritation, itchiness, tearing, etc. with signs of conjunctival injection, papillary reaction, eyelid swelling, etc. (Halliday et. al, 2018; Camara and Lagunzad, 2011). Moreover, some studies of residents from areas not affected by vog have reported an increase in pulmonary, nasal and eye

problems (Longo et al., 2008). This can be attributed to a combination of the prevailing wind directions over Hawai'i and the terrain, which causes the exposure of volcanic emissions at different rates across the island (Chow et al., 2010).

Hawai'i Island, with its mountainous terrain, experiences orographic blocking that affects local-scale circulations on the island, especially in areas with weak trade wind flow like Kona (Yang et al., 2008; Chen and Nash, 1994). Hilo, located in the east of the island, and Kohala, located in the northern end of the island, are usually protected by prevailing NE trade winds (Chow et al. 2010). Hilo is affected by katabatic flows as well; these flows are descending cold dense bodies of air (Garza et al., 2012). Kohala is, additionally, protected from wind reversals by Mauna Kea, the tallest point on the island (Chow et al., 2010). In contrast, the Kona coast, located along the west flanks of Mauna Loa and Hualālai volcanoes, receives vog particles from the NE trade winds, which carries it clockwise around the southern part of the island (Chow et al., 2010). Kona Winds can combine with the diurnal offshore and onshore wind patterns associated with sea and land breezes causing the vog particles to remain on the Kona coast for extended periods of time (Chow et al., 2010).

Objectives and Research Questions

The goal of this thesis is to analyze weather station data in Hawai'i (specifically in Hilo and Kona) and teleconnection indices to determine if a noticeable change in wind patterns has occurred over time and how these changes may be related to larger oscillations, phases, and patterns. For example, global, regional, and local atmospheric patterns influence hazard potential in Hawai'i, particularly hazards related to vog. Possible long-term changes in wind patterns may result in increased exposure to vog across the Hawaiian Islands during future eruptions. Research questions for this thesis are as follows:

1. While Garza et al. (2012) identified a decrease in Northeast Trade Winds, to what extent have those trends continued over the most recent decade and are data collected by land-based weather stations in Hawai'i representative of this trend?
2. Considering the reported reduction in Northeast Trade Winds over time, how are these changes connected to atmospheric patterns and, importantly, how may these changes alter the impacts of vog and other hazards in the Hawaiian Islands?

CHAPTER 2. DATA AND METHODS

Data Acquisition and Processing

All teleconnection patterns and time-series data were acquired from the National Oceanic and Atmospheric Administration (NOAA)'s Climate Prediction Center (CPC). Monthly wind data were acquired from NOAA's Climate Data Online (CDO) portal selecting the Global Summary of the Month (GSOM) in CSV format with geographic location and atmospheric variables of wind speed (WS) and wind direction (WD) in standard units. Wind data were recorded at two airport weather stations in Hawai'i: Hilo International Airport and Ellison Onizuka Kona International Airport at Keāhole. For purposes of this research, the weather stations were labeled as Hilo and Kona. Hilo wind data range from 1980 to the present and the weather station elevation is 11.6 m above mean sea level (MSL). Kona wind data range from 1998 to the present while the weather station is 13.1 m above MSL. The elevation for both of the weather stations had no changes throughout the studied years (i.e., the stations were not moved or altered). The anemometer pole height (in meters) for Hilo was 6 m prior to 1998 and from 1998-present it has been 10 m according to Garza et al. (2012). The Kona station has recorded data since 1998 and experienced no change in the anemometer height. According to Cardone et al. (1990), a +/-5m shift in the anemometer height results in variability of less than 5%. Following Cardone et al. (1990), a correction of the data is unnecessary for the anemometer height change at the Hilo weather station considering the minimal change in variability that occurs. Prior to 1998, wind speed and direction were measured using 1-minute intervals (identified as WS/WD 1), while wind speed and direction measured 1998-present are recorded using 2-minute and 5-second intervals (identified as WS/WD 2 and WS/WD 5). The data

provided for WD was in azimuth degrees (0°-360°) where 0° and 360°=north, 90°=east, etc. In the case of WS, the standard unit of measurement was miles per hour (mph).

Table 2.1. Teleconnection Index Names and Acronyms, Dataset used, Date Ranges, and Region they Cover.

Teleconnection Indices	Acronym	Dataset Used	Region	Data Date Range
East Central Tropical Pacific SST Index	Niño3.4	HadISST1	5N-5S, 170W-120W	1870-present
Pacific Decadal Oscillation Index	PDO	Various	Poleward of 20N in the Pacific basin	1900-present
West Pacific Index	WP	NCEP R1		1950-present
Pacific/North Atlantic Index	PNA	NCEP R1		1950-present
Bivariate ENSO Time-series Index	BEST	HadISST1		1870-present
Multivariate ENSO Time-series Index	MEI V2	ICOADS	Tropical Pacific	1979-present
Central Tropical Pacific SST Index	Niño4	HadISST1	5N-5S, 160E-150W	1870-present
Oceanic Niño Index	ONI	NOAA ERSST V5	5N-5S, 170W-120W	1950-present
Trans-Niño Index	TNI	HadISST1	Difference Niño 1.2 and Niño 4	1870-present

The teleconnection time-series data had different neutral points where some were neutral at zero and others were neutral at twenty-seven. The SST values are in degrees Celsius (°C) for all teleconnections. In this research, the neutral was changed and calculated to be thirty for all time-series, to create a standard central value across all time-series. This method avoids negative values and varying neutral points and is better for statistical analysis and interpretation.

Analysis

Wind roses for wind direction and speed were generated using Microsoft Excel, along with additional box and whisker graphs to further analyze and visualize the data. First, wind direction variables were changed from degree direction to one of eight cardinal directions using the following formula:

$$= LOOKUP(MOD(A1,360),\{0,45,90,135,180,225,270,315,360\},$$

$$\{"N","NE","E","SE","S","SW","W","NW","N"\})$$

According to Garza et al. (2012), the wind rose plot with the eight-point compass is the most standard method for expressing the WD. It uses the four cardinal points (north, east, south, and west) in conjunction with the four ordinal points (northeast, southeast, southwest, and northwest). This research uses the defined wind observations between 22.5° and 67.5° to identify prevailing NE trade winds and observations between 67.9° and 112.5° to identify dominant east trade winds over the Hawaiian Islands following Garza et al. (2012). Each wind observation encompasses a 45° angle.

Afterward, wind roses were created from 1980 to 2018 using both wind direction and speed in a pivot table and then grouping the WS into three categories and showing the values in their grand-total. Values were then organized in a radar chart to visualize the directions and create a wind rose. These wind roses were generated for each station. Data were further divided by five-year interval to examine possible variability in more detail. For the five-year periods, wind roses were created with WD according to each month and compared to verify dominant WD. Then the data were further divided by year to investigate trends and dominant wind directions; wind roses were generated for each case as well. WS was graphed for both stations throughout the time period.

All teleconnections patterns were graphed using Microsoft Excel as well. These were graphed using a custom combination chart with the WD (in degree direction) along the y-axis, and the date along the x-axis. Additionally, the neutral point “30” (equivalent to 0°C) was indicated in all graphs. As previously mentioned in the El Niño Southern Oscillation section these time-series have thresholds. For the Niño 3.4, Niño 4 and ONI teleconnection graphs these thresholds were added to indicate El Niño values (>30.5) equivalent to 0.5°C and La Niña values

(<29.5) equivalent to -0.5°C. Another two thresholds were added designate Strong El Niño values (>31.5) equivalent to 1.5°C and Strong La Niña values (<28.5), equivalent to -1.5°C.

Table 2.2. Wind Direction in their Degree and Cardinal Direction at 45° angles.

Wind Direction	
Degree Direction	Cardinal Direction
0 – 22.5	N
22.6 – 67.5	NE
67.6-112.5	E
112.6-157.5	SE
157.6-202.5	S
202.6-247.5	SW
247.6-292.5	W
292.5-337.5	NW
337.5 – 360	N

The IBM Statistical Product and Service Solutions (SPSS) Statistics program version 25 was used for statistical analysis (IBM, 2017). All statistical analysis was performed for Hilo and Kona respectively. First, a correlation diagnostic was performed on all variables (all teleconnections, WS, and WD) to verify if a parametric or non-parametric correlation exist. Then a Spearman rank-order correlation coefficient (Spearman’s correlation), which is a non-parametric correlation, is tested between all teleconnections using bivariate correlations analysis. This test calculates the direction and strength of the relationship between two variables. For the analysis, it is specified to give flags (asterisk-*) beside values that are significant ($p<0.05$). As a result, the test gives a correlation table where the correlation coefficient values with asterisks are the most important.

Next, an Ordinary Least Square (OLS) Regression (OLS Regression) of WS was conducted; this method was used to assess teleconnection indices as well. An OLS Regression is used when the value of a variable may be used to predict the value of another variable. For the OLS Regression model, WS was the dependent variable and teleconnection index values served as the independent variables. Three tables were produced from this analysis: Model Summary, ANOVA (which generates a report on how well the regression analysis fits the data, more specifically the dependent variable), and Coefficients (which provides information on the predicted variable from the independent variables).

A Multinomial Logistic Regression (MLR) was used to predict a nominal dependent variable (WD in this study) based on independent variables (index values). The MLR was processed eight times, once for each WD. Some advantages of the MLR is its flexibility in using nominal or continuous independent variables and allowing variables to interact with one another to improve prediction of the nominal dependent variable. This analysis results in five important tables.

The first is a Goodness-of-Fit table that provides two measures that are used to assess how well the model fits the data by presenting significance using a Pearson and a Deviance chi-square statistic. The chi-square statistic is used to identify the relationship between two categorical variables and test for independence. The second table provides the Model Fitting Information. The third table displays various pseudo R-square (R^2) measurements (Cox and Snell, Nagelkerke, and McFadden) in which MLR considers these similar to R^2 values from an OLS Regression which analyzes the proportion of variance explained by a model. The fourth table is the Likelihood Ratio Test that demonstrates which of the independent variables (teleconnection indices) are statistically significant. The final table shows the Parameters

Estimates or Coefficient of the Model and includes the significance (sig.) and the coefficient in exponentiated values.

An OLS Regression analysis was conducted for WS vs time where the dependent variable is WS and the independent variable is the studied years for Hilo 1- and 2-minute (1980 to 2018), Hilo 5-secondseconds (1998 to 2018), Kona 2-minute (1998 to 2018,) and Kona 5-secondseconds (1999 to 2018) wind observations to examine the magnitude of time coefficient and the statistical significance of these values. Finally, an OLS Regression analysis was conducted for frequency of NE trade winds vs. time. The dependent variable was frequency of NE trade winds in days in the studied years for Hilo 1- and 2-minute, Hilo 5-secondseconds, Kona 2-minute, and Kona 5-second,seconds and the independent variable is time (studied years).

CHAPTER 3. RESULTS

Wind roses showing wind speed and direction were created for each weather station and each observation type (1- and 2-minute and 5-second) over their entire periods of record. In Figure 3.1, a wind rose (A) shows combined 1-minute and 2-minute wind observations (WS/WD1+2) from 1980 to 2018 in Hilo indicating that ~44% of prevailing winds originated from the east. Southeast winds had approximately ~13% prevalence. North winds recorded the second highest prevalence at ~22%. Northeast winds were prevalent over ~14% of the period of record. And winds from all other directions (South, Southwest, West, and Northwest) experienced less than ~5% over the period of record. A second wind rose (B) shows 5-second wind observations (WS/WD5) from 1998 to 2018 in Hilo indicating that 41% of prevailing winds originated from the east. North winds recorded the second highest prevalence at 21%. Northeast winds occurred 16% over the period of record and southeast winds occurred 12% over the period of record. South and northwest winds were observed less than 5% over the period of record, while no west winds were recorded. A third wind rose (C) shows 2-minute wind observations (WS/WD2) from 1998 to 2018 in Kona indicating that 44% of prevailing winds originated from the northeast. North winds recorded the second highest prevalence at 24%. South winds occurred 11% over the period of record and east winds had minimal wind dominance with 8% prevalence. Southeast, southwest, west, and northwest winds were observed less than 5% over the period of record. A fourth wind rose (D) shows 5-second wind observations (WS/WD5) from 1999 to 2018 in Kona indicated that 45% of prevailing winds originated from the northeast. North winds recorded the second highest prevalence at 22%. South and east winds occurred 10% over the period of record. Southeast, southwest, west, and northwest winds were observed less than 5% over the period of record.



Figure 3.1. Wind roses for Hilo show 1-minute and 2-minute wind speeds and directions from 1980-2018 (A) and 5-second wind speeds and directions from 1998 to 2018 (B) based on the eight primary cardinal directions. Wind roses for Kona show 2-minute wind speeds and directions from 1998-2018 (C) and 5-second wind speeds and directions from 1999-2018 (D) based on eight primary cardinal directions.

Additional wind roses were created from Hilo weather station data (1- and 2-minute observations) after partitioning the data into ~5-year time intervals (Figure 3.2). Approximately 50% of prevailing winds originated from the east in 1980-1984, 23% originated from the southeast, and ~12% originated from the north (Figure 3.2A). In the subsequent 5-year period (1985-1989), approximately 23% of prevailing winds originated from the east, 23% originated from the southeast, and 25% originated from the north (Figure 3.2B). From 1990-1994, approximately 33% of winds originated from the east, 25% originated from the northeast, and 32% originated from the north (Figure 3.2C). In the subsequent 5-year period (1995-1999), approximately 55% of winds originated from the east and 27% originated from the north (Figure 3.2D). From 2000-2004, approximately 47% of winds originated from the east, 25% originated from the north, and 22% originated from the northeast (Figure 3.2E). In the subsequent 5-year period (2005-2009), approximately 53% of winds originated from the east, 18% originated from the north, and 17% originated from the northeast (Figure 3.2F). From 2010-2014, approximately 52% of winds originated from the east, 12% originated from the north, and 15% originated from the southeast (Figure 3.2G). In the subsequent 4-year period (2015-2018), approximately 42% of winds originated from the east, 27% originated from the north, and 21% originated from the southeast (Figure 3.2H).

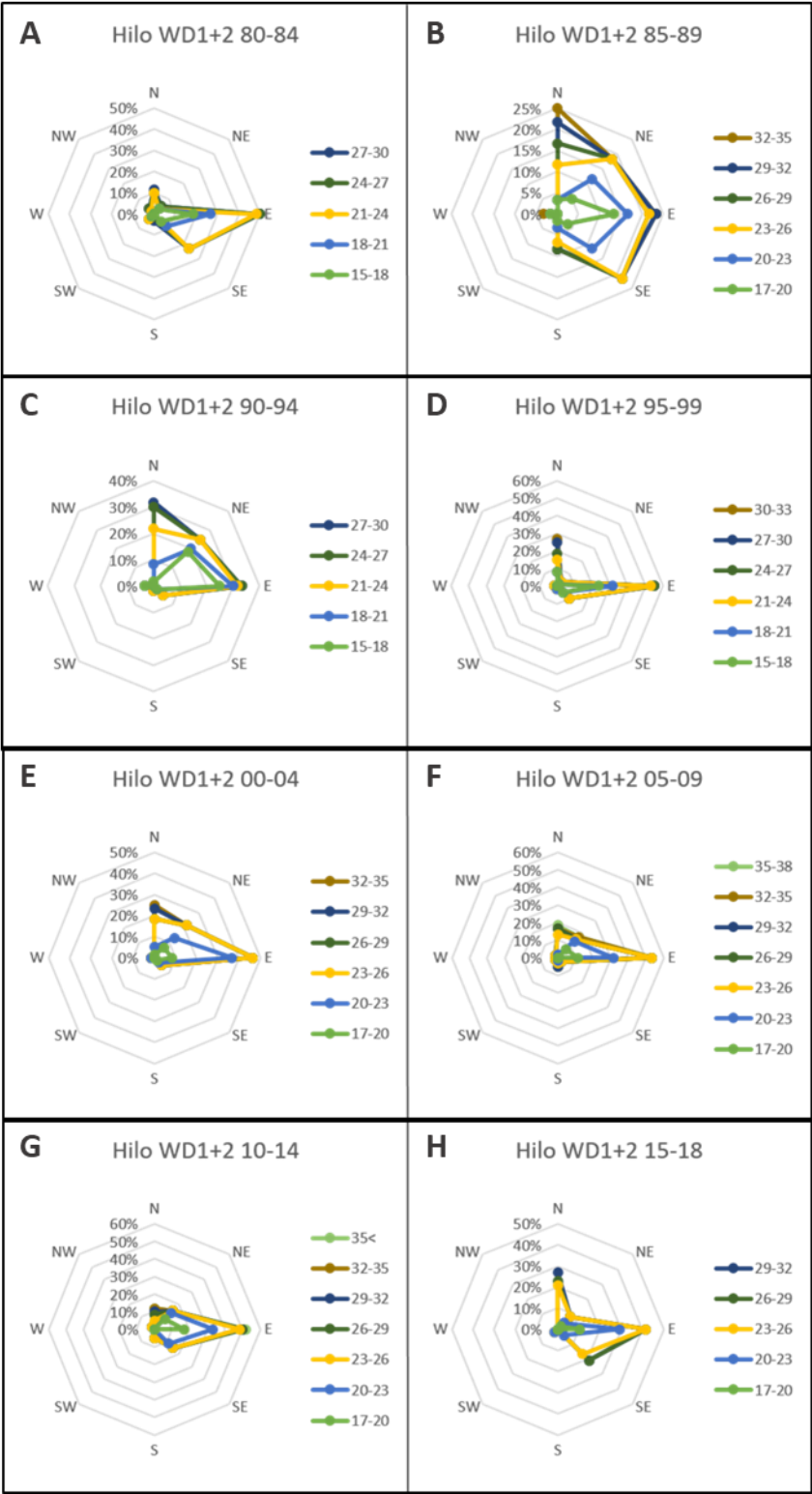


Figure 3.2. Wind roses for Hilo showing 1-minute and 2-minute wind direction and wind speed observations subset into ~5-year time periods.

Using 5-second observation data, wind roses were also created for time periods that overlapped with the previous Hilo time periods (Figure 3.3) Approximately 63% of prevailing winds originated from the east in 1998-1999 and ~17% originated from the northeast (Figure 3.3A). In the subsequent 5-year period (2000-2004), approximately 32% of prevailing winds originated from the east, 23% originated from the north, and 25% originated from the northeast (Figure 3.3B). From 2005-2009, approximately 47% of winds originated from the east, 15% originated from the northeast, and 17% originated from the north (Figure 3.3C). In the subsequent 5-year period (2010-2014), approximately 41% of winds originated from the east, 17% originated from the northeast, and 17% originated from the north (Figure 3.3D). From 2015-2018, approximately 38% of winds originated from the east, 29% originated from the north, and 21% originated from the southeast (Figure 3.3E).

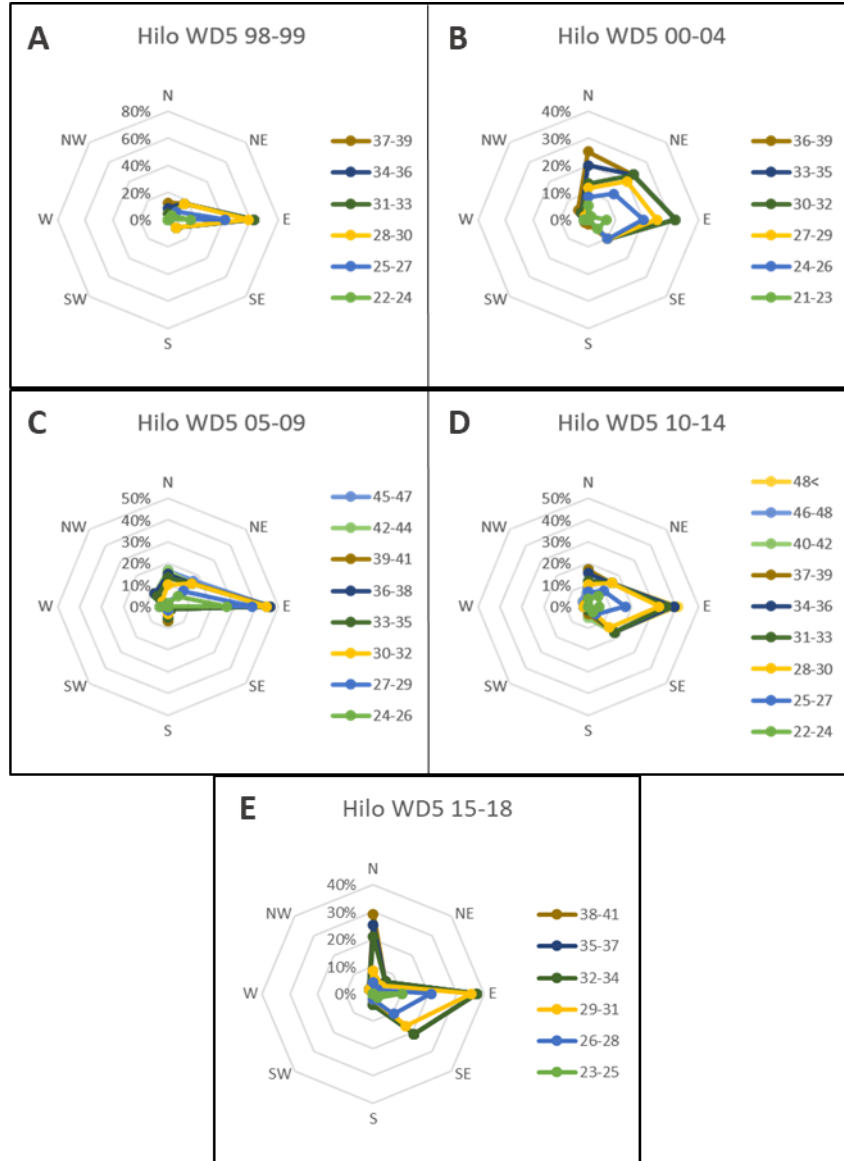


Figure 3.3. Wind roses for Hilo showing 5-second wind direction and wind speed observations subset into ~5-year time periods (overlapping with the time periods in Figure 3.2).

Data subsets were also created for Kona using 1- and 2-minute observation data to create wind roses (Figure 3.4). Approximately 58% of prevailing winds originated from the northeast in 1998-1999, 13% originated from the north, and 13% originated from the east (Figure 3.4A). In the subsequent 5-year period (2000-2004), approximately 47% of prevailing winds originated from the northeast, 18% originated from the north, 18% originated from the east, and 12% originated from the south (Figure 3.4B). From 2005-2009, approximately 50% of winds originated from the northeast, 20% originated from the north, and 10% originated from the south (Figure 3.4C). In the subsequent 5-year period (2010-2014), approximately 40% of winds originated from the northeast, 28% originated from the north, and 13% originated from the south (Figure 3.4D). From 2015-2018, approximately 40% of winds originated from the north, 31% originated from the northeast, and 13% originated from the south (Figure 3.4E).

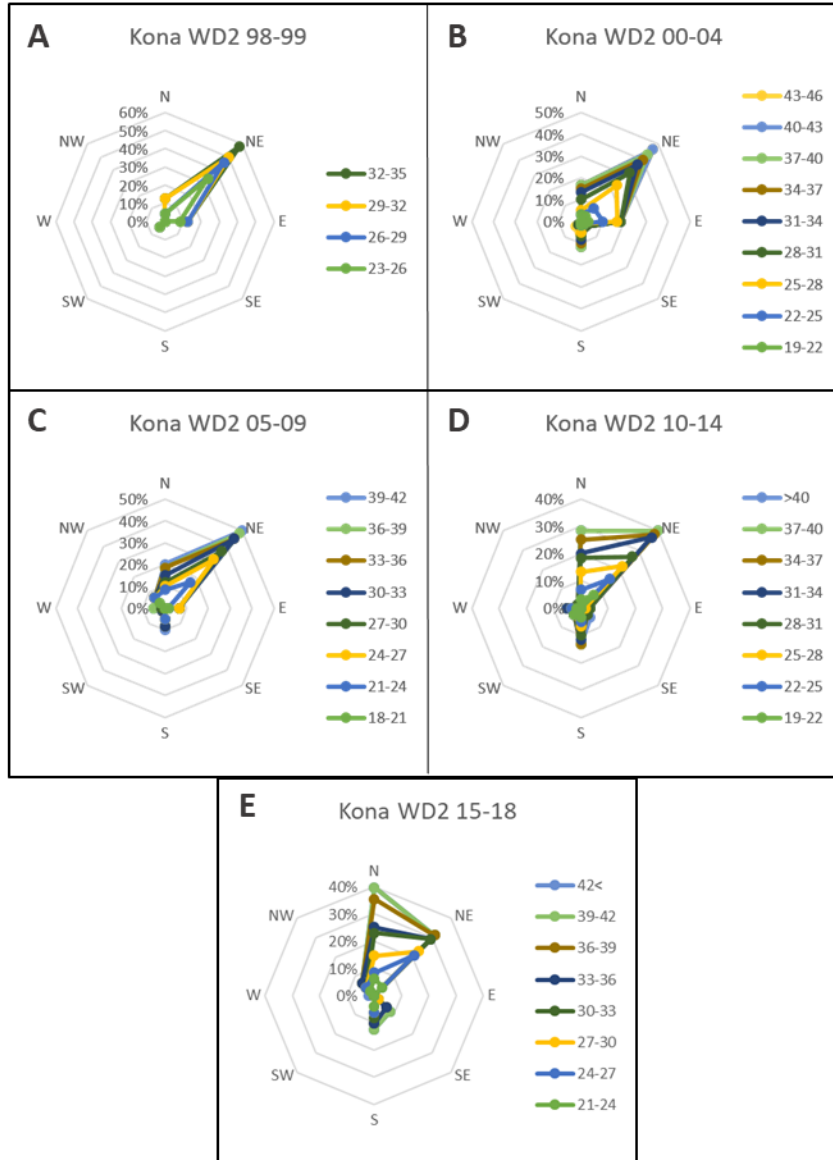


Figure 3.4. Wind roses for Kona showing 1-minute and 2-minute wind direction and wind speed observations subset into ~5-year time periods.

Additional data subsets were created for Kona using 5-second observation data to create wind roses (Figure 3.5). Approximately 83% of prevailing winds originated from the northeast in 1998-1999 and 17% originated from the east (Figure 3.5A). In the subsequent 5-year period (2000-2004), approximately 48% of prevailing winds originated from the northeast, 17% originated from the east, and 12% originated from the south (Figure 3.5B). From 2005-2009, approximately 50% of winds originated from the northeast, 15% originated from the north, and 7% originated from the east (Figure 3.4C). In the subsequent 5-year period (2010-2014), approximately 39% of winds originated from the northeast, 31% originated from the north, and 12% originated from the east (Figure 3.5D). From 2015-2018, approximately 39% of winds originated from the northeast, 34% originated from the north, and 14% originated from the south (Figure 3.5E).

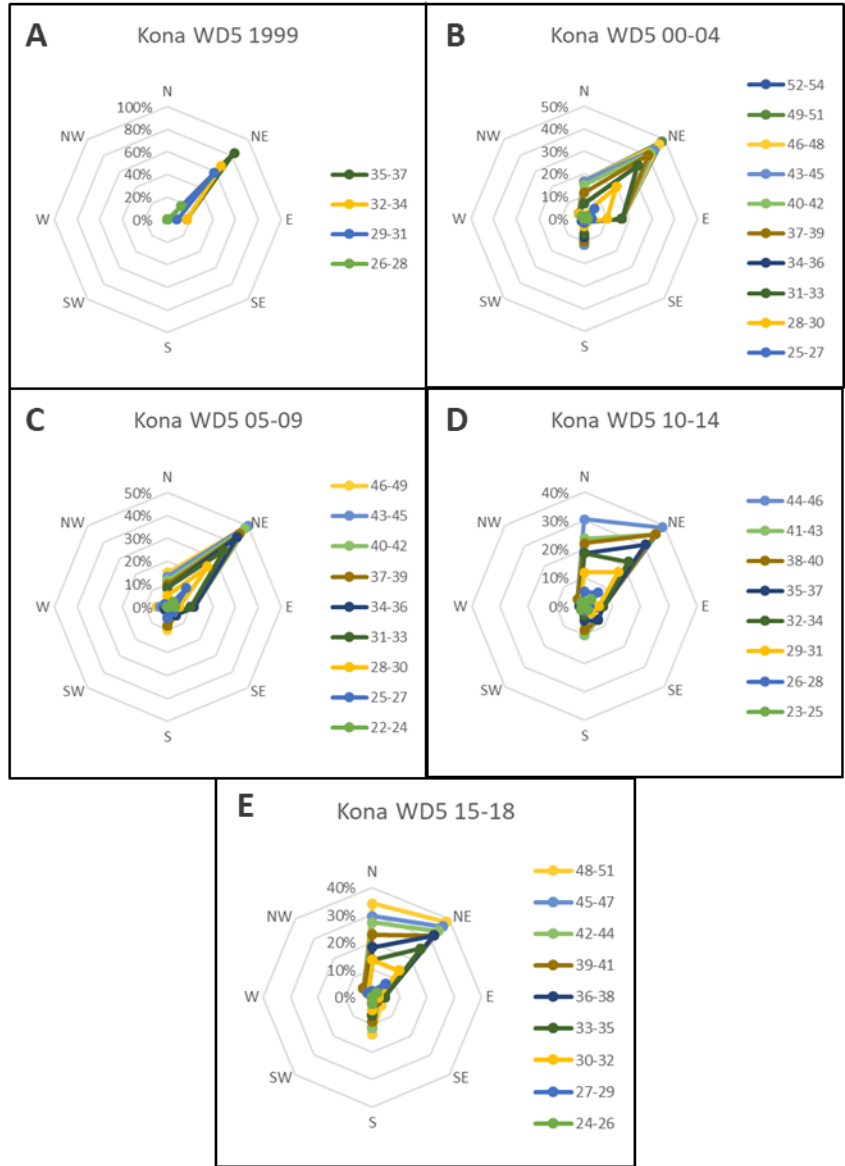


Figure 3.5. Wind roses for Kona showing 5-second wind direction and wind speed observations subset into ~5-year time periods (overlapping with the time periods in Figure 3.4).

The Spearman rank-order correlation coefficient results (Table 3.1) have cells with dashes meaning that there is no significance ($p>0.05$). The TNI time-series shows negative results between TNI and other time-series signifying a moderate negative correlation. Conversely, the other teleconnections show positive correlation between the time-series. Some have high R-values but other have low R-values (i.e. Best vs. PNA shows $r=0.146$). The WP index only has a positive correlation with the MEI V2 index. In contrast, MEI V2 has correlations with all time-series.

Table 3.1. Results of SPSS Spearman Correlation between All Teleconnections.

Correlation Coefficients --- Spearman's rho									
Teleconnections Indices	Niño3.4 Index	PDO Index CPC	WP Index	PNA Index	BEST Index	MEI V2 Index	Niño4 Index	ONI Index	TNI Index
Niño3.4	-	.423**	-	.107*	.810**	.749**	.799**	.874**	-.288**
PDO	.423**	-	-	.249**	.429**	.498**	.328**	.426**	-
WP	-	-	-	-	-	.118*	-	-	-
PNA	.107*	.249**	-	-	.146**	.141**	-	.136**	-
BEST	.810**	.429**	-	.146**	-	.901**	.817**	.914**	-.352**
MEI V2	.749**	.498**	.118*	.141**	.901**	-	.776**	.911**	-.301**
Niño4	.799**	.328**	-	-	.817**	.776**	-	.868**	-.577**
ONI	.874**	.426**	-	.136**	.914**	.911**	.868**	-	-.382**
TNI	-.288**	-	-	-	-.352**	-.301**	-.577**	-.382**	-
**. Correlation is significant at the 0.01 level (2-tailed).									
*. Correlation is significant at the 0.05 level (2-tailed).									

The results for the OLS Regression of WS vs. all teleconnections are shown in Tables 3.2-3.5 with values in red (in the significance column) indicating a statistically significant coefficient ($p \leq 0.05$), while values in black were not statistically significant ($p > 0.05$). Table 3.2 shows a significant relationship between the WS and four teleconnection indices (Niño 3.4, Niño 4, ONI, and TNI indices). Table 3.3 shows a significant relationship with four teleconnection indices (Niño 3.4, PDO, Niño 4, and ONI indices). Table 3.4 shows a significant relationship with five teleconnection indices (Niño 3.4, PDO, Niño 4, ONI, and TNI indices). Lastly, in Table 3.5 a significant relationship is identified with four teleconnection indices (Niño 3.4, PDO, WP, and ONI indices).

Table 3.2. Results of SPSS OLS Regression between All Teleconnections and Hilo 1- and 2-Minute Wind Speed.

Coefficients		
	Unstandardized Coefficients	Sig.
(Constant)	49.763	0.001
Niño3.4 Index	-1.374	0.000
PDO Index	0.148	0.418
WP Index	0.247	0.132
PNA Index	0.151	0.376
BEST Index	-0.067	0.875
MEI V2 Index	-0.509	0.286
Niño4 Index	-2.531	0.000
ONI Index	3.395	0.000
TNI Index	-0.351	0.026
a. Dependent Variable: WSF1+2		

Table 3.3. Results of SPSS OLS Regression between All Teleconnections and Hilo 5-Seconds Wind Speed.

Coefficients		
	Unstandardized Coefficients	Sig.
(Constant)	51.929	0.065
Niño3.4 Index	-2.828	0.000
PDO Index	0.900	0.010
WP Index	0.320	0.272
PNA Index	-0.361	0.259
BEST Index	-0.297	0.659
MEI V2 Index	0.234	0.793
Niño4 Index	-3.074	0.004
ONI Index	4.928	0.000
TNI Index	-0.534	0.066
a. Dependent Variable: WSF5		

Table 3.4. Results of SPSS OLS Regression between All Teleconnections and Kona 2-Minute Wind Speed.

Coefficients		
	Unstandardized Coefficients	Sig.
(Constant)	55.882	0.163
Niño3.4 Index	-2.476	0.013
PDO Index	1.016	0.040
WP Index	0.507	0.217
PNA Index	-0.668	0.138
BEST Index	-0.132	0.890
MEI V2 Index	0.392	0.756
Niño4 Index	-6.942	0.000
ONI Index	8.554	0.000
TNI Index	-1.033	0.014
a. Dependent Variable: WSF2		

Table 3.5. Results of SPSS OLS Regression between All Teleconnections and Kona 5-Seconds Wind Speed.

Coefficients		
	Unstandardized Coefficients	Sig.
(Constant)	-20.131	0.630
Niño3.4 Index	-4.140	0.000
PDO Index	1.631	0.001
WP Index	0.955	0.016
PNA Index	-0.758	0.081
BEST Index	-1.104	0.241
MEI V2 Index	0.812	0.567
Niño4 Index	-2.890	0.064
ONI Index	7.584	0.000
TNI Index	-0.220	0.624
a. Dependent Variable: WSF5		

The results for the MLR are shown in Tables 3.6-3.9 with an “x” indicating a statistically significant coefficient ($p \leq 0.05$), while those with no “x” were not statistically significant ($p > 0.05$). Table 3.6 shows a major relationship between the WD and three teleconnections (Niño 3.4, Niño 4, and ONI indices). Table 3.7 shows a major relationship with five teleconnections (Niño 3.4, WP, BEST, ONI and TNI indices). Table 3.8 shows a relationship with three teleconnections (Niño 3.4, PNA, and TNI indices). Lastly, in Table 3.9 a major relationship is identified with three teleconnections (PNA, MEI V2, and ONI indices).

Table 3.6. Results of a Multinomial Logistic Regression of Wind Direction for Hilo1+2 and All Teleconnection Indices in the Pacific. Red Indices showed significance for most of the 8-Cardinal Compass Directions.

Indices	N	NE	E	SE	S	SW	W	NW	HILO WD1+2
Niño3.4 Index	X	X	X	X		X		X	
PDO Index CPC	X	X	X						
WP Index	X	X		X				X	
PNA Index		X	X	X					
BEST Index	X	X	X						
MEI V2 Index									
Niño4 Index	X	X	X	X				X	
ONI Index	X	X	X	X		X	X	X	
TNI Index			X					X	

Table 3.7. Results of a Multinomial Logistic Regression of Wind Direction for Hilo5 and All Teleconnection Indices in the Pacific. Red Indices showed significance for most of the 8-Cardinal Compass Directions.

Indices	N	NE	E	SE	S	SW	W	NW	HILO WDS
Niño3.4 Index	X	X	X	X				X	
PDO Index CPC									
WP Index	X	X	X	X	X			X	
PNA Index	X	X							
BEST Index	X	X	X	X	X			X	
MEI V2 Index									
Niño4 Index		X						X	
ONI Index	X	X	X	X		X		X	
TNI Index	X	X	X	X				X	

Table 3.8. Results of a Multinomial Logistic Regression of Wind Direction for Kona2 and All Teleconnection Indices in the Pacific. Red Indices showed significance for most of the 8-Cardinal Compass Directions.

Indices	N	NE	E	SE	S	SW	W	NW	KONA WD2
Niño3.4 Index	X	X		X			X	X	
PDO Index CPC									
WP Index	X			X				X	
PNA Index		X	X	X			X	X	
BEST Index									
MEI V2 Index									
Niño4 Index									
ONI Index	X	X		X			X		
TNI Index	X	X		X	X			X	

Table 3.9. Results of a Multinomial Logistic Regression of Wind Direction for Kona5 and All Teleconnection Indices in the Pacific. Red Indices showed significance for most of the 8-Cardinal Compass Directions.

Indices	N	NE	E	SE	S	SW	W	NW	KONA WDS
Niño3.4 Index	X	X		X			X		
PDO Index CPC	X	X						X	
WP Index									
PNA Index	X	X	X		X		X		
BEST Index									
MEI V2 Index	X	X		X			X	X	
Niño4 Index									
ONI Index	X	X		X		X	X	X	
TNI Index									

Wind direction observations from 1- and 2-minute recordings in Hilo were plotted and compared to various teleconnection index values and thresholds in Figures 3.6-3.9 (Niño3.4, PNA, ONI, and TNI respectively). Values below the neutral threshold, 30 in the index, are indicative of colder SSTs while values above the neutral threshold are indicative of warmer SSTs. Values above the red line for Figures 3.6 and 3.9 indicate a positive value for El Niño, while values below the blue line indicate a positive value for La Niña. Typically, if values are over 31.5 in the index these are considered to be strong El Niño events. Conversely, the opposite is true if values are below 28.5 in the index, these are considered to be strong La Niña events. According to the results from Hilo WD1+2 observations in Figures 3.6-3.9, easterly winds (67.6-112.5 degrees) are predominant. Results for other teleconnections (PDO, WP, BEST, MEI V2, and Niño4) are presented in Appendix B.

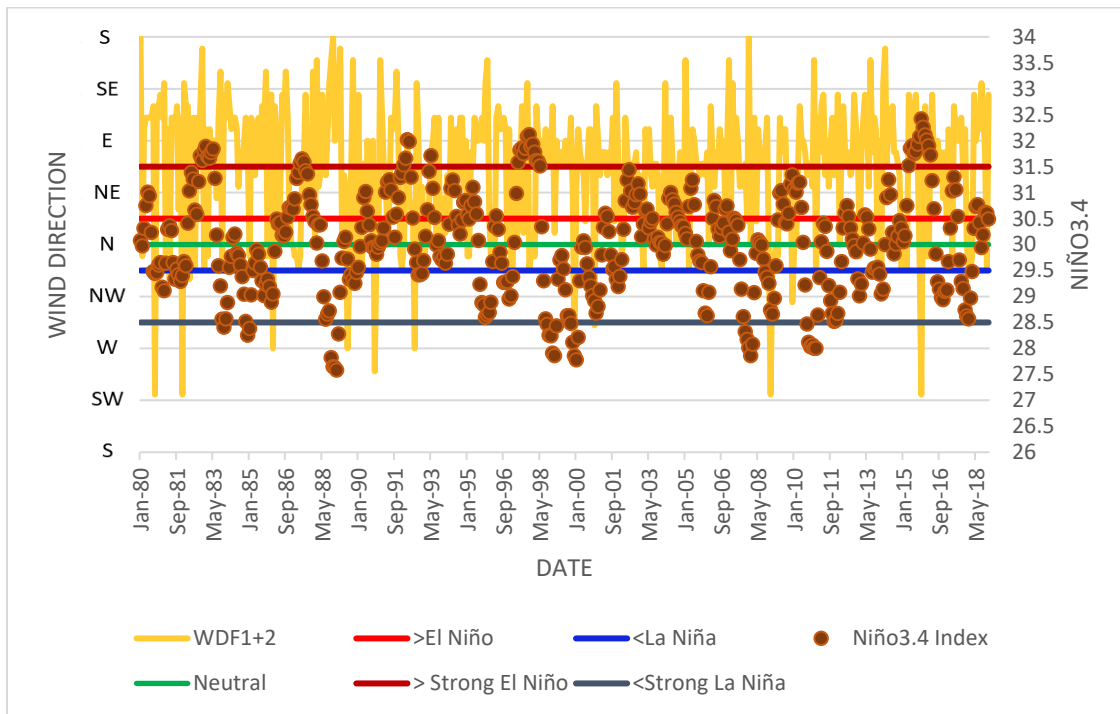


Figure 3.6. Hilo WD1+2 from 1980-2018 shows the wind direction in comparison with the index. The primary y-axis (left) shows wind direction values in degrees and the secondary y-axis (right) shows the Niño3.4 index values while the date is shown on the x-axis. The Neutral threshold is at 30 according to the index value.

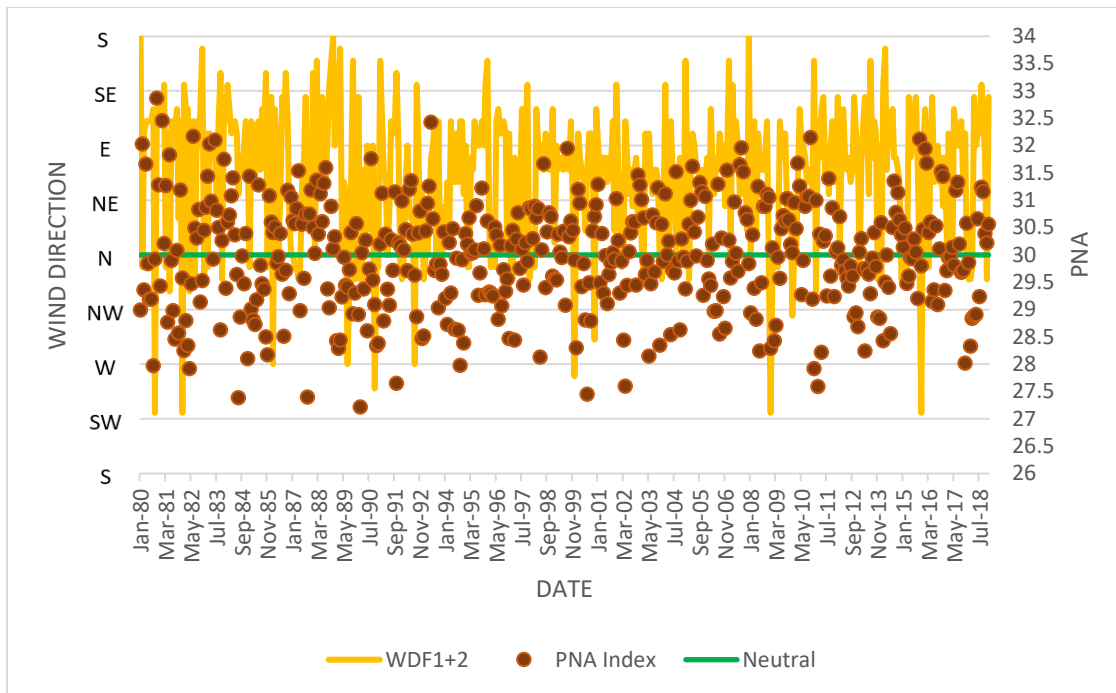


Figure 3.7. Hilo WD1+2 from 1980-2018 shows the wind direction in comparison with the index. The primary y-axis (left) shows wind direction values and the secondary y-axis (right) shows the PNA index values while the date is shown on the x-axis. The Neutral threshold is at 30 according to the index value.

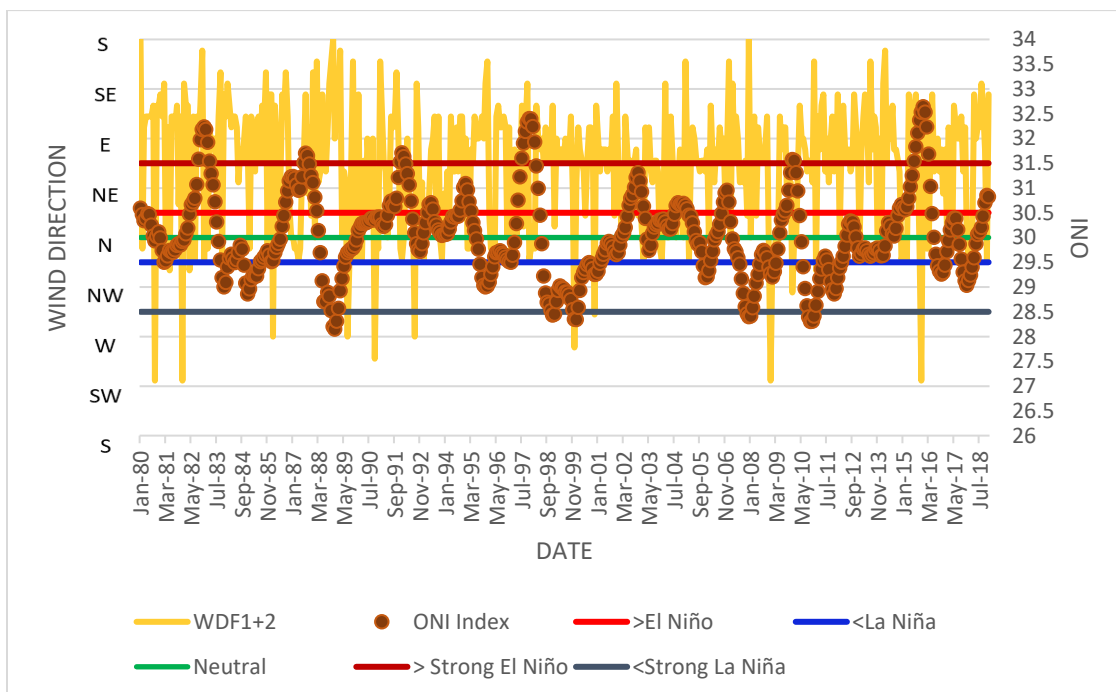


Figure 3.8. Hilo WD1+2 from 1980-2018 shows the wind direction in comparison with the index. The primary y-axis (left) shows wind direction values and the secondary y-axis (right) shows the ONI index values while the date is shown on the x-axis. The Neutral threshold is at 30 according to the index value.

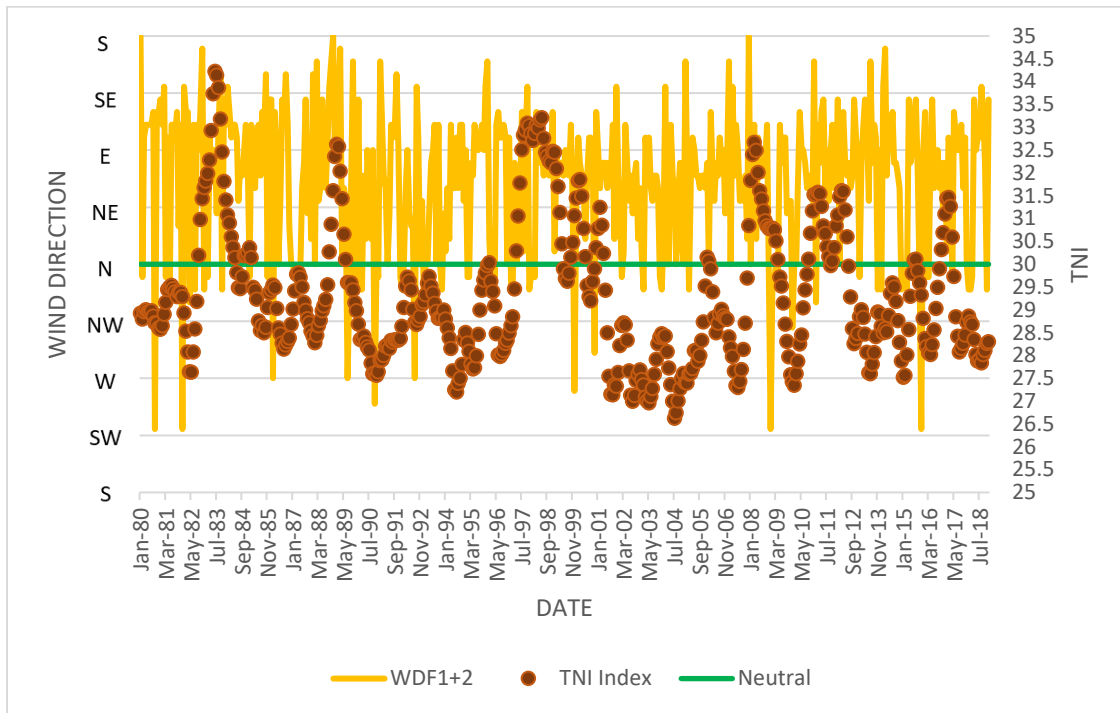


Figure 3.9. Hilo WD1+2 from 1980-2018 shows the wind direction in comparison with the index. The primary y-axis (left) shows wind direction values and the secondary y-axis (right) shows the TNI index values while the date is shown on the x-axis. The Neutral threshold is at 30 according to the index value.

Wind direction observations from 5-second recordings in Hilo were also plotted and compared to various teleconnection index values and thresholds in Figures 3.10-3.13 (Niño3.4, PNA, ONI, and TNI respectively). Results for other teleconnections (PDO, WP, BEST, MEI V2, and Niño4) are presented in Appendix B.

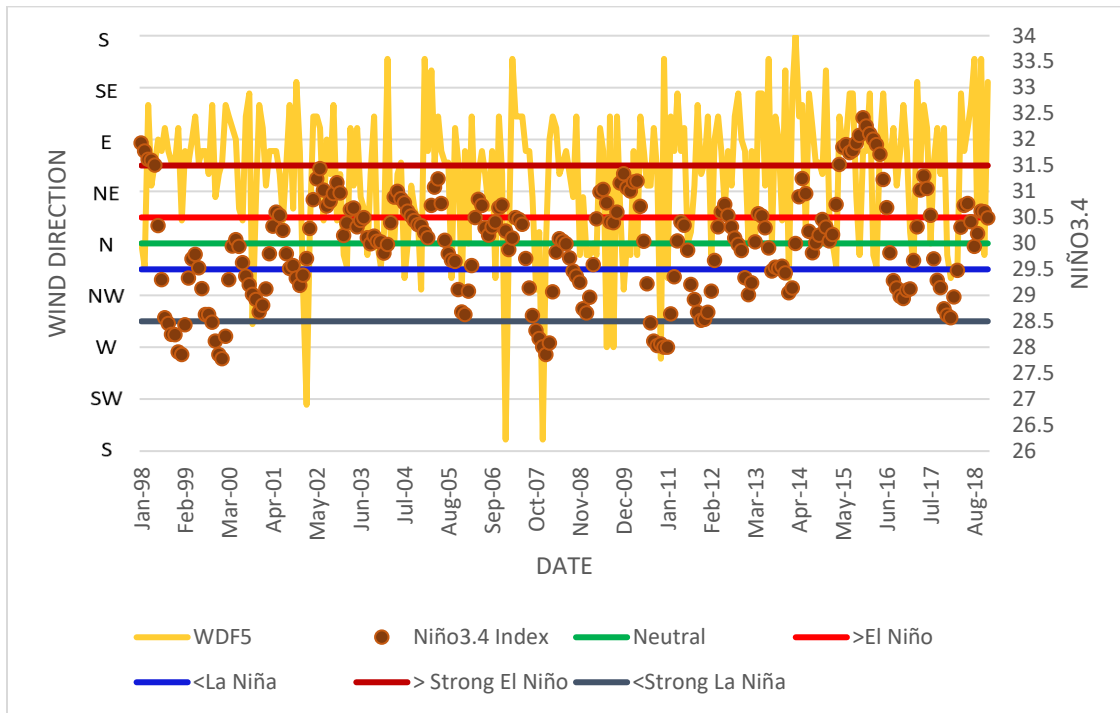


Figure 3.10. Hilo WD5 from 1998-2018 shows the wind direction in comparison with the index. The primary y-axis (left) shows wind direction values and the secondary y-axis (right) shows the Niño3.4 index values while the date is shown on the x-axis. The Neutral threshold is at 30 according to the index value.

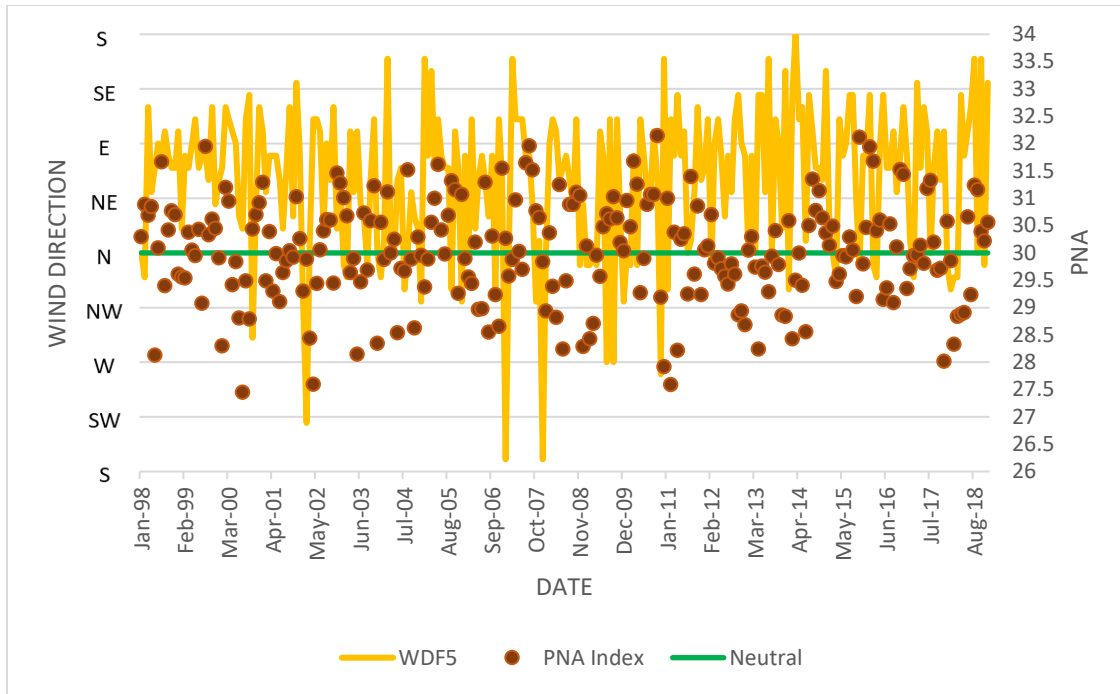


Figure 3.11. Hilo WD5 from 1998-2018 shows the wind direction in comparison with the index. The primary y-axis (left) shows wind direction values and the secondary y-axis (right) shows the PNA index values while the date is shown on the x-axis. The Neutral threshold is at 30 according to the index value.

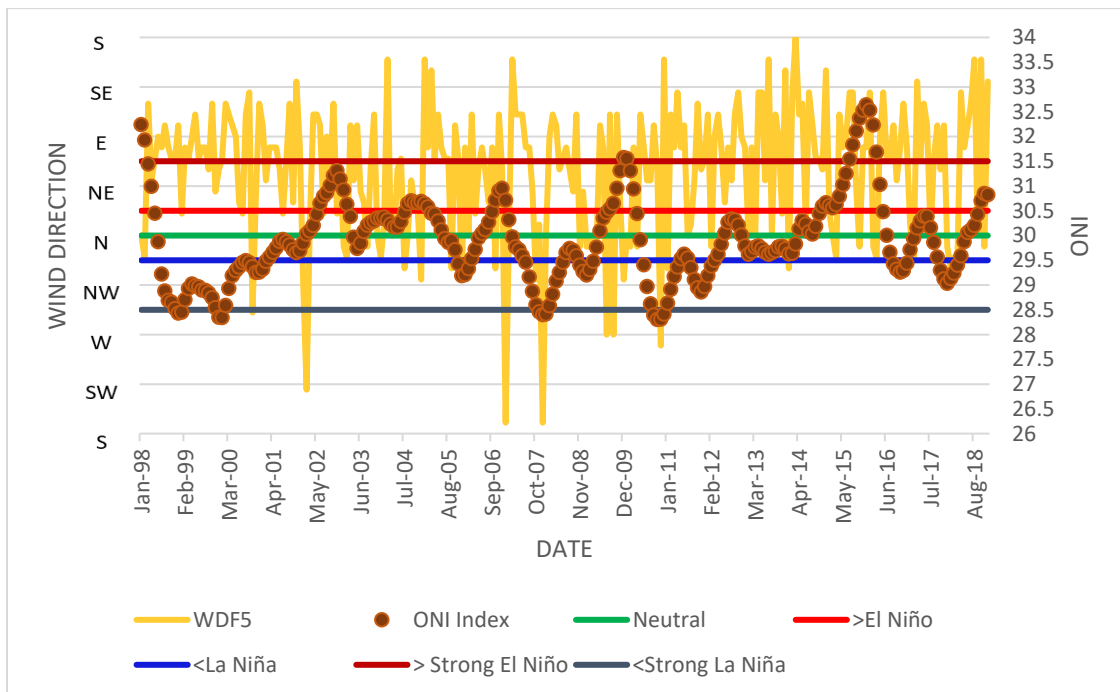


Figure 3.12. Hilo WD5 from 1998-2018 shows the wind direction in comparison with the index. The primary y-axis (left) shows wind direction values and the secondary y-axis (right) shows the ONI index values while the date is shown on the x-axis. The Neutral threshold is at 30 according to the index value.

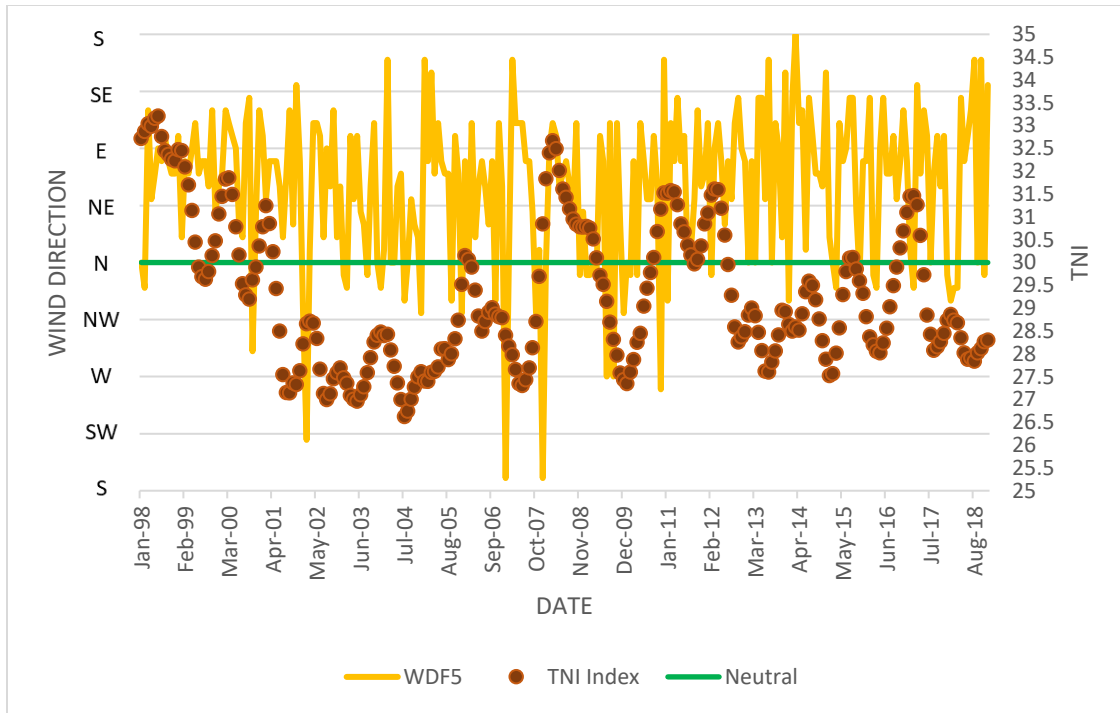


Figure 3.13. Hilo WD5 from 1998-2018 shows the wind direction in comparison with the index. The primary y-axis (left) shows wind direction values and the secondary y-axis (right) shows the TNI index values while the date is shown on the x-axis. The Neutral threshold is at 30 according to the index value.

Wind direction observations from 2-minute recordings in Kona were plotted and compared to various teleconnection index values and thresholds in Figures 3.14-3.17 (Niño3.4, PNA, ONI, and TNI respectively). Results for other teleconnections (PDO, WP, BEST, MEI V2, and Niño4) are presented in Appendix B.

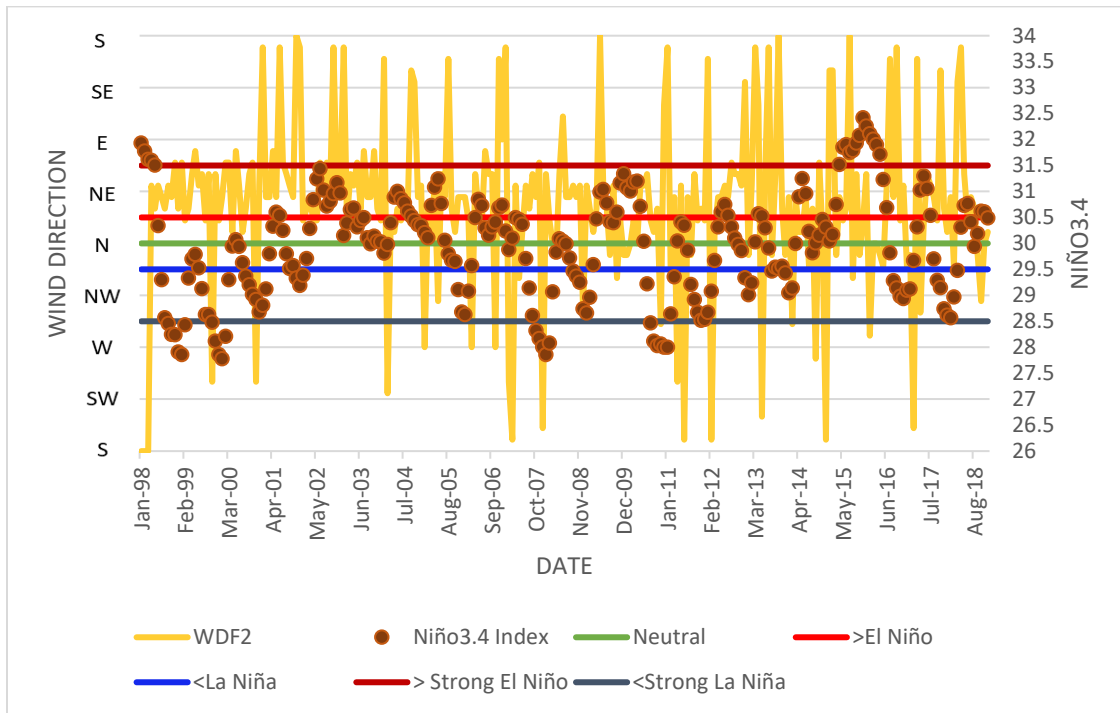


Figure 3.14. Kona WD2 from 1998-2018 shows the wind direction in comparison with the index. The primary y-axis (left) shows wind direction values and the secondary y-axis (right) shows the Niño3.4 index values while the date is shown on the x-axis. The Neutral threshold is at 30 according to the index value.

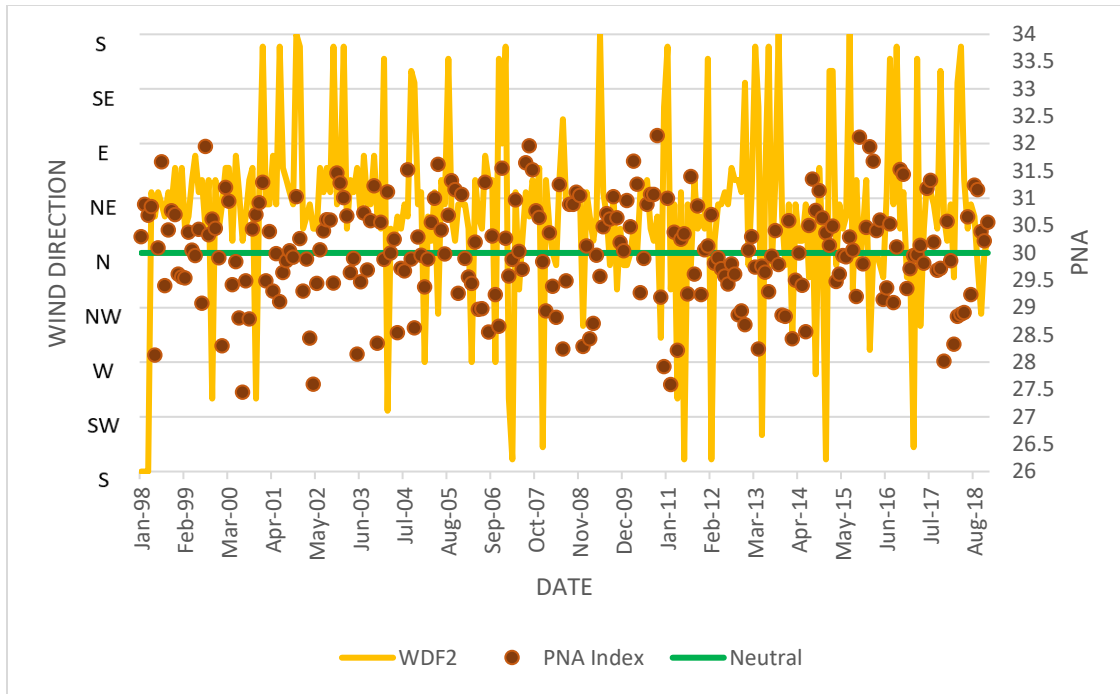


Figure 3.15. Kona WD2 from 1998-2018 shows the wind direction in comparison with the index. The primary y-axis (left) shows wind direction values and the secondary y-axis (right) shows the PNA index values while the date is shown on the x-axis. The Neutral threshold is at 30 according to the index value.

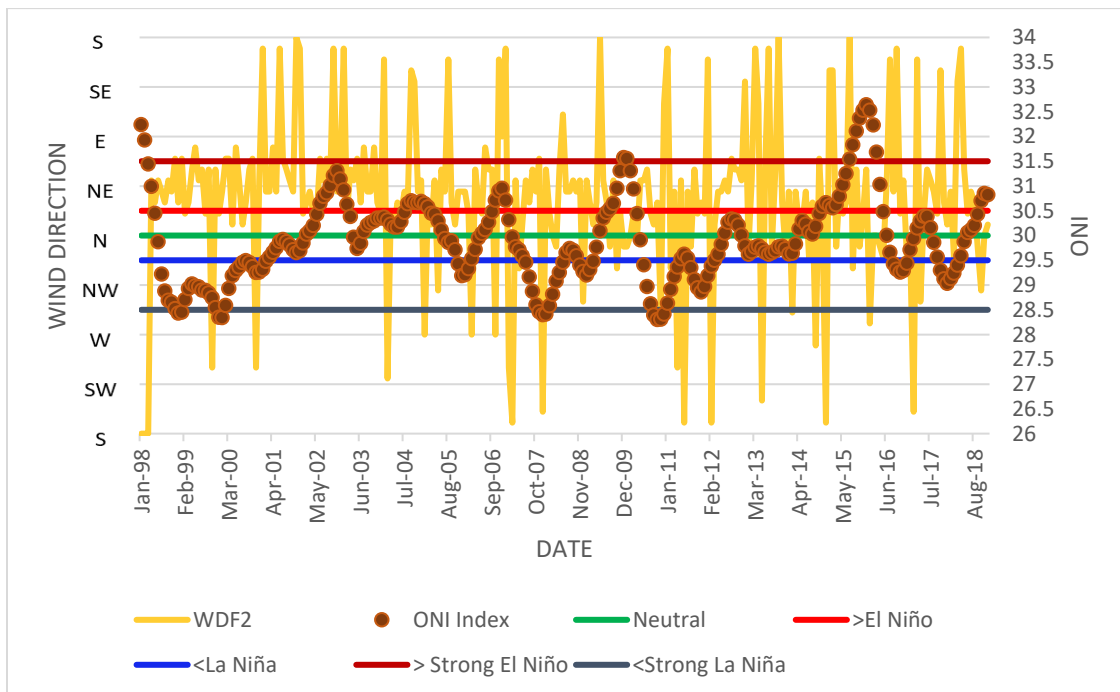


Figure 3.16. Kona WD2 from 1998-2018 shows the wind direction in comparison with the index. The primary y-axis (left) shows wind direction values and the secondary y-axis (right) shows the ONI index values while the date is shown on the x-axis. The Neutral threshold is at 30 according to the index value.

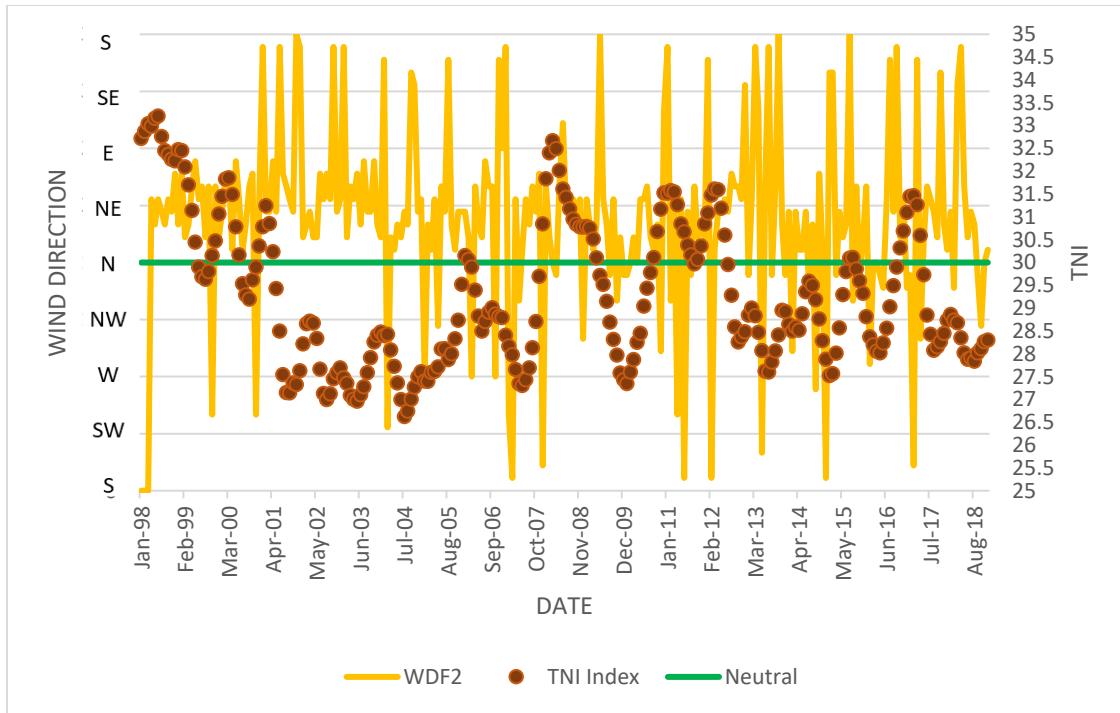


Figure 3.17. Kona WD2 from 1998-2018 shows the wind direction in comparison with the index. The primary y-axis (left) shows wind direction values and the secondary y-axis (right) shows the TNI index values while the date is shown on the x-axis. The Neutral threshold is at 30 according to the index value.

Wind direction observations from 5-second recordings in Kona were plotted and compared to various teleconnection index values and thresholds in Figures 3.18-3.21 (Niño3.4, PNA, ONI, and TNI respectively). Results for other teleconnections (PDO, WP, BEST, MEI V2, and Niño4) are presented in Appendix B.

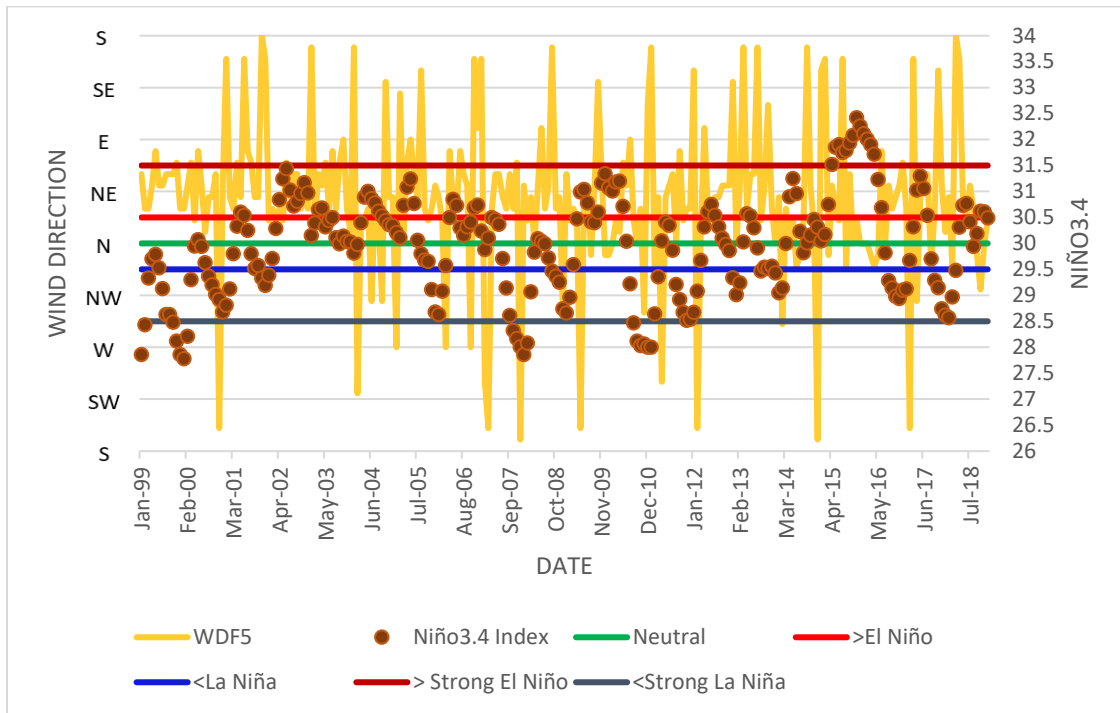


Figure 3.18. Kona WD5 from 1998-2018 shows the wind direction in comparison with the index. The primary y-axis (left) shows wind direction values and the secondary y-axis (right) shows the Niño3.4 index values while the date is shown on the x-axis. The Neutral threshold is at 30 according to the index value.

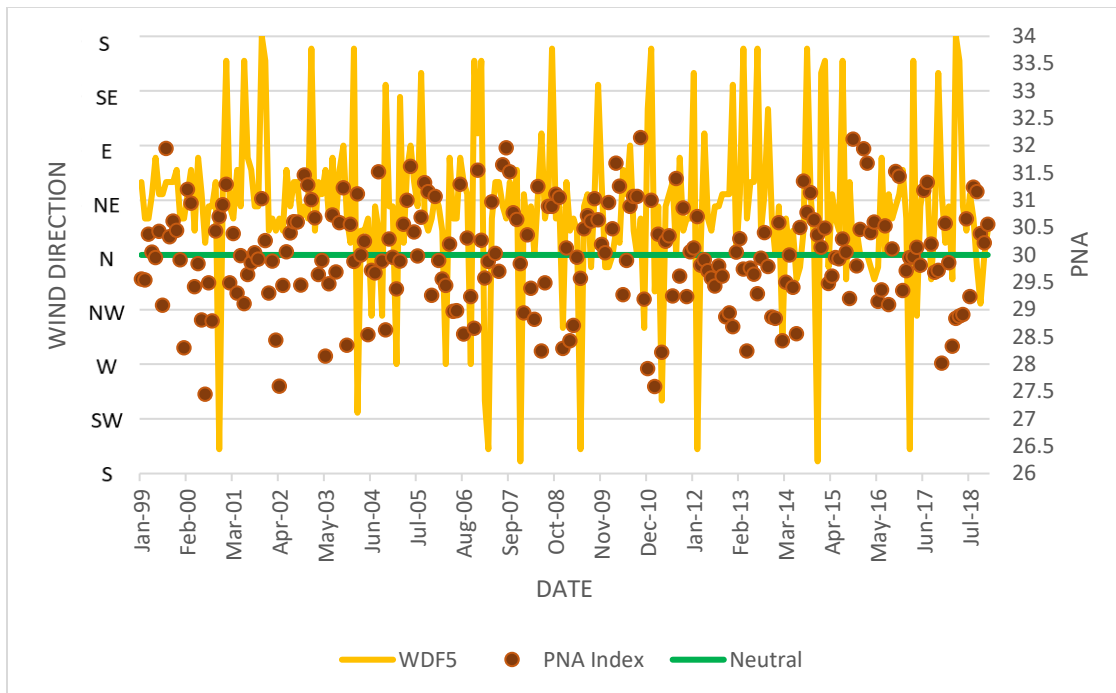


Figure 3.19. Kona WD5 from 1998-2018 shows the wind direction in comparison with the index. The primary y-axis (left) shows wind direction values and the secondary y-axis (right) shows the PNA index values while the date is shown on the x-axis. The Neutral threshold is at 30 according to the index value.

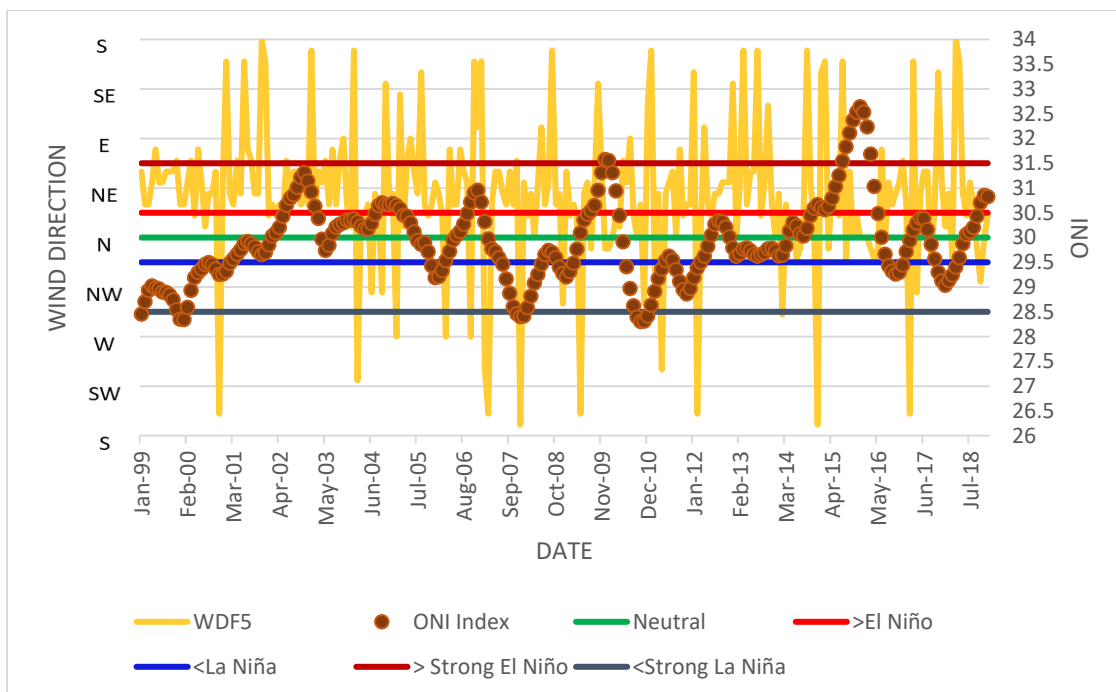


Figure 3.20. Kona WD5 from 1998-2018 shows the wind direction in comparison with the index. The primary y-axis (left) shows wind direction values and the secondary y-axis (right) shows the ONI index values while the date is shown on the x-axis. The Neutral threshold is at 30 according to the index value.

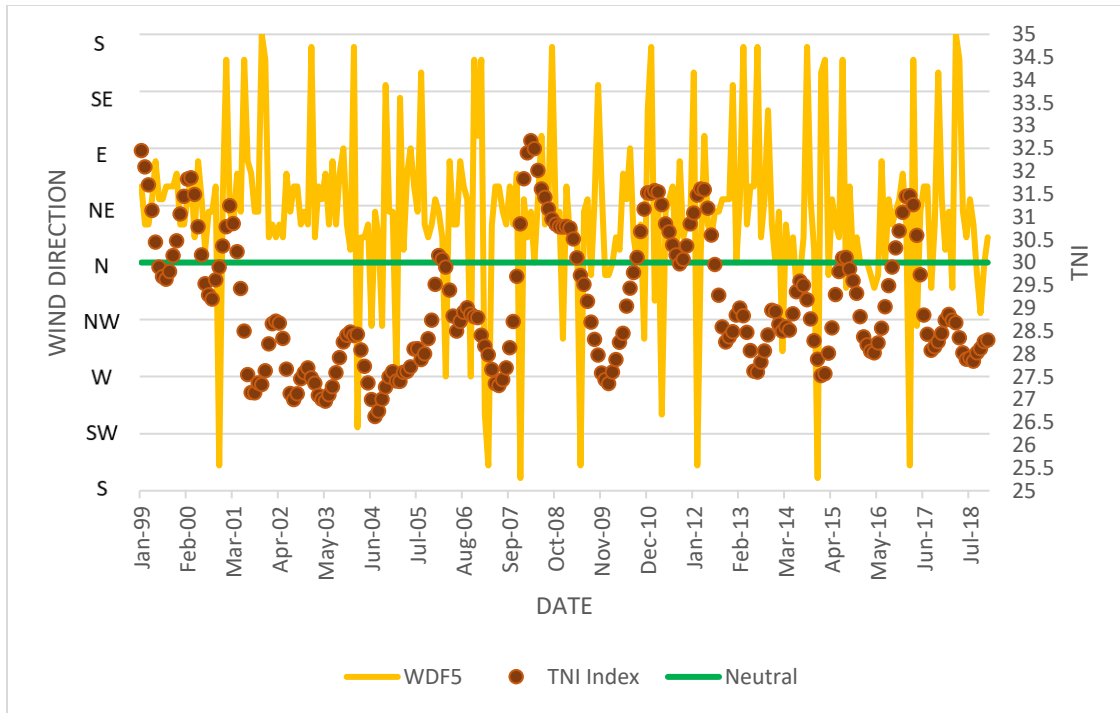


Figure 3.21. Kona WD5 from 1998-2018 shows the wind direction in comparison with the index. The primary y-axis (left) shows wind direction values and the secondary y-axis (right) shows the TNI index values while the date is shown on the x-axis. The Neutral threshold is at 30 according to the index value.

The wind speed time series graphs (Figures 3.22-3.25) display the OLSOLS regression results of wind speed (y, dependent variable) versus time (x, independent variable). Positive and statistically significant coefficients in the regression equations indicate a significant increase in WS throughout the years. The smallest increase in WS is from Hilo WS1+2, while the largest increase in WS is from Kona WS5. There is a peak in WS in all graphs for the year 2014, while in Kona WS2 displays a major peak for the year 2016.

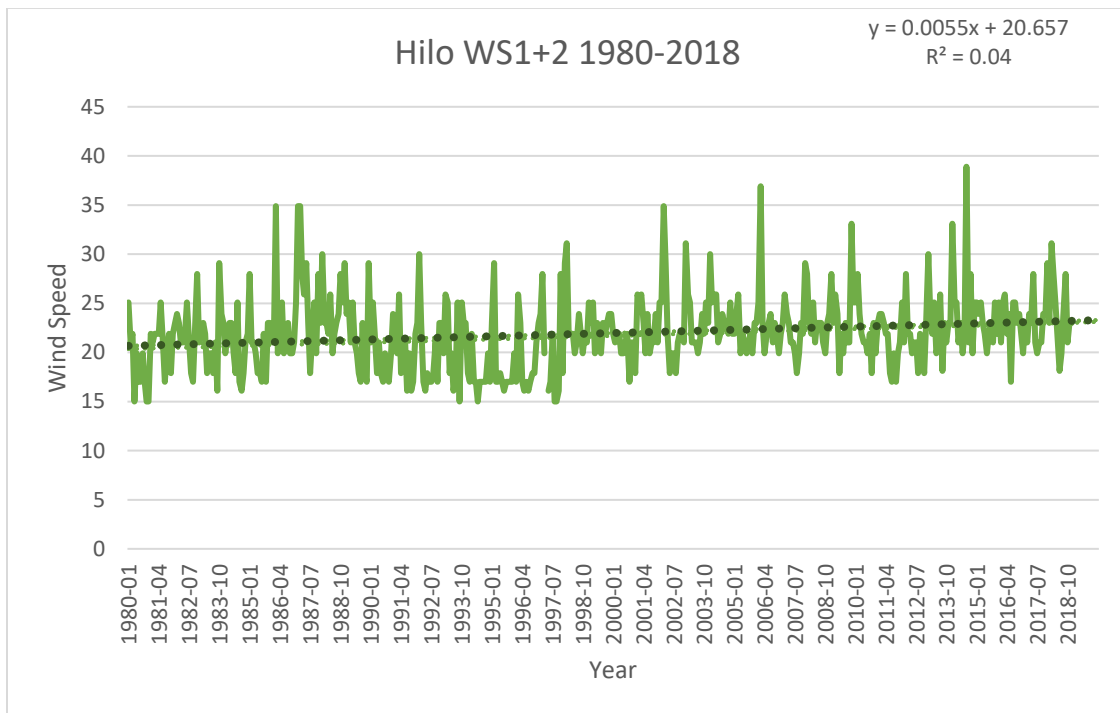


Figure 3.22. Graph for Hilo WS1+2 from 1980-2018 shows wind speed in miles per hour (mph) with linear trendline and R-square in the upper right corner.

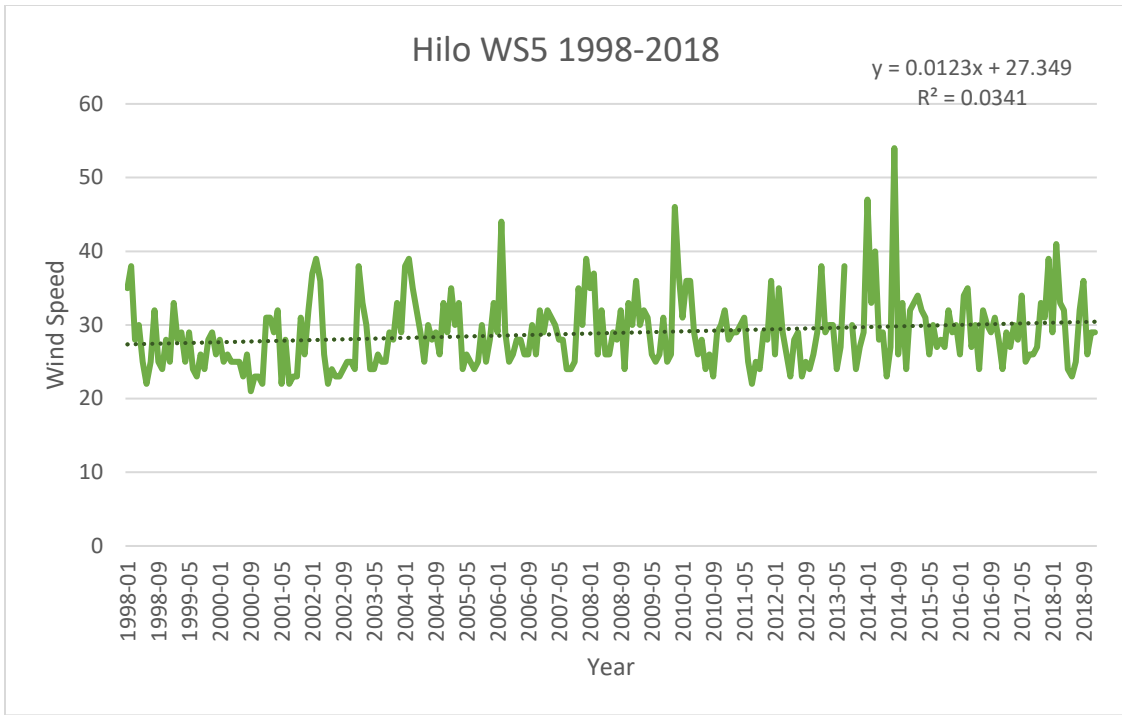


Figure 3.23. Graph for Hilo WS5 from 1998-2018 shows wind speed in miles per hour (mph) with linear trendline and R-square in the upper right corner.

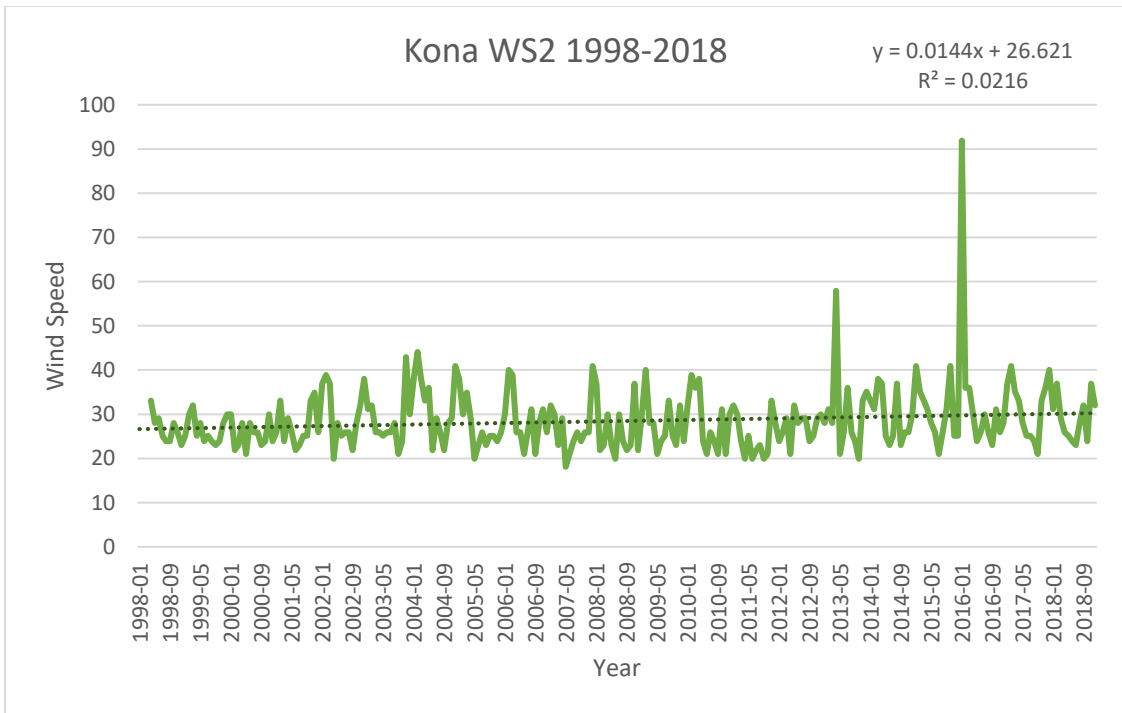


Figure 3.24. Graph for Kona WS2 from 1998-2018 shows wind speed in miles per hour (mph) with linear trendline and R-square in the upper right corner.

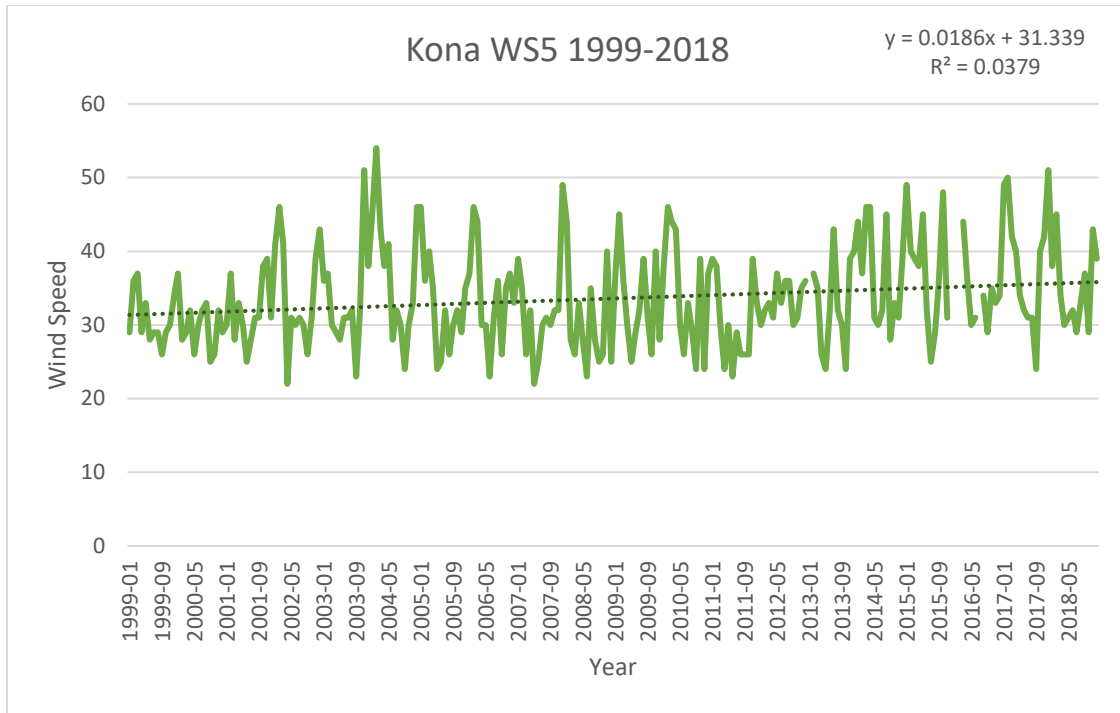


Figure 3.25. Graph for Kona WS5 from 1999-2018 shows wind speed in miles per hour (mph) with linear trendline and R-square in the upper right corner.

CHAPTER 4. DISCUSSION

Results clearly indicate that trade wind dynamics over Hawai'i have changed over time, corroborating previous findings from Garza et al. (2012). This thesis also finds that the trend has continued since 2010. Data from land-based weather stations located at Hilo and Kona allowed for surface-level analysis of wind speeds and directions, revealing variability especially in recent decades. Compared to Garza et al. (2012), however, there are differences with the amount of data and the locations where data were collected. Garza et al. (2012) used a weather station on each of the Hawaiian Islands and four ocean buoy stations. The weather stations and islands included Kauai with the Lihue station, Oahu with the Honolulu station, Maui with the Kahului station, and Hawaii with the Hilo station, while this thesis focuses only on Hawai'i Island and used two weather stations - Hilo on the east side and Kona on the west side of the island to primarily examine low-level emissions from Kilauea.

The 5-year interval wind roses from Hilo show dominant prevailing east winds with the second-most prevalent winds being from the north, confirming that generally north and east 'trade' winds drive weather patterns in the region. However, wind directions on the Island of Hawai'i are influenced and altered by topography. According to Garza et al. (2012), Hilo experiences katabatic flows due to the location of Mauna Kea, which also forces the NE trade winds to flow split and move around the island. Figures 3.2 to 3.3 the wind flow from the East is easily identified. Another important factor is that with the presence of the trade wind inversion the vog particles dispersed to the east of Mauna Loa can drift out away from the island when above 2 km but when these particles are low enough (below 2 km) they are then blown back by the trade winds and then dispersed in multiple directions by the flow splitting that occurs in and around Hilo.

The Kona 5-year interval wind roses, in contrast to Hilo, have a distinct northeast dominant wind pattern. Kona is not as affected by flow splitting as Hilo, however the resulting flow splitting from Mauna Loa and Mauna Kea cause the windward trade winds under 2 km to move around the volcanoes. In the north, the wind passes over the Kohala Mountains located over northern Hawaii, which are below the trade wind inversion, and then flow “south” towards the Kona region. This wind flow, when combined with the Kona leeward side winds, forms one of the counter-rotating vortices in the northwestern area, which are more prominent when trades winds are stronger. The other counter-rotating vortex is fueled by winds passing in the area below 2 km south of Mauna Kea. These south winds can in turn pick-up vog particles from Kīlauea and spread them to the southern areas of the island.

The wind roses confirm that Hilo is dominated by easterly winds which is expected. These easterly winds encounter flow-splitting and katabatic flows that are common on the east side of the island. Moreover, the flow of the trade winds towards the islands tends to be “trapped” due to higher elevations and the trade wind inversion layer, which causes this area of the island to experience more precipitation. Topography impacts the climate and related hazards on the Island of Hawai’i more than the other Hawaiian Islands, where almost all mountain elevations are below 2 km.

In addition to the changes in wind direction, wind speeds have gradually increased throughout the years, which was alluded to by Garza et al. (2012). Statistical analysis with the OLS Regression indicated that these changes are significant ($p < 0.05$), which reinforce the results for the R^2 in the Figures 3.22-25. These results indicate small increase in WS for Hilo and Kona stations (for both minutes and second data) with highly significant values in correspondence to the years. In accordance with wind speed and teleconnection relationships, the teleconnections is

seems that the changes can be attributed primarily to four indices overall. Similar to the results for WD, the ENSO fluctuations (Niño3.4, Niño 4, and ONI) have a more noticeable impact on wind variations. The PDO teleconnection also shows a high impact on wind speed. These teleconnection results are statistically significant with Niño3.4 and Niño 4 being related to a slight decrease in wind speed, while ONI and PDO indicates a slight increase in wind speed.

An overall gradual decline, which can be seen in the annual results, is observed in the NE trade winds and, especially for the Kona weather station in Table 4.1. A slight increase of NE winds is seen from 2000-2009 in Kona with a more prominent decrease afterwards; this change is minimal when observed in Hilo. For Hilo 1- and 2-minute wind direction observations, a low presence for NE winds is observed throughout the studied years but a trend is observed with a gradual increase from 1980 to 1994, a short-term decrease from 1995 to 1999, followed by a minimal increase from 2000-2009, and finally a decrease from 2010-2018. This general trend is observed using 2-minute wind direction observations at both Hilo and Kona and 5-second wind direction observations at Kona as well from 1998-2018. Using 5-year intervals, these fluctuations in NE winds are easier to identify Table 4.5.

According to Garza et al., (2012) there is a decrease in northeast winds and an increase in east winds. They attribute this to shift in location of the subtropical high-pressure zone and to teleconnections like the ENSO. They give an example of Honolulu, which had the most noticeable decrease in NE trade winds since 1973 when they typically experienced 291 days of NE trade winds per year (79%), but by 2009 the trade winds transpired for only 210 days per year (57%). They mention that Lihue and Kahului also experienced decreases in annual NE trade winds and that Hilo did not reveal significant change in regards to wind frequency. Nevertheless, in this research if we compare the frequency of NE trade winds for the years 1999, 2009, and

2018 in Kona and Hilo the results show a difference between the east and west side of the main island (Table 4.1). In Hilo, located on the east side of Hawai'i, the NE trade winds occurrence from 1999 had an average of 60 days per year (17%), for 2009 they had an average of 60 days per year (17%) as well, and for 2018 they had a 0 days per year (0%). In contrast, for Kona which is situated on the west side of Hawai'i the NE trade winds occurrence for 1999 had an average of 243 days per year (67%), for 2009 they had an average of 181 days per year (50%), and for 2018 they experienced 124 days (34%). Statistical analysis using with the OLS Regression for Hilo 5-secondseconds, Kona 2-minute, and Kona 5-seconds winds indicate a statistically significant decrease of yearly NE trade winds of approximately 2-4 days per year. However, the observed decrease in NE trade winds was not statistically significant for Hilo 1Hilo1- and 2-minute winds.

In relation to the teleconnections, the changes in wind direction are likely attributed to ENSO fluctuations (based on the Niño 3.4, ONI and TNI); however, this can be related to the PNA and WP patterns as well. The results for the correlations between all teleconnections indicate that the TNI has a moderate negative correlation to all other indices, which is indicative that when another teleconnection is active the TNI does not strengthen it. This could be because the time-series takes into account the influence of teleconnection patterns over larger areas (tropical equatorial Pacific). Multiple weather observation records were correlated to teleconnection indices for both Kona and Hilo. The PNA and WP also influence local patterns in Hawaii since those patterns displace the jet stream in certain directions depending on the phase they exhibit (positive or negative). Moreover, WD and vog dispersal are further influenced by weather patterns and this research found that Niño 3.4, ONI, TNI, and PNA indices have noticeable impact on these factors. For example during the years that ENSO (El Niño) is active

(Table 4.2) the NE trades winds are more constant over the island and can disperse vog more efficiently compared to years where the ENSO is neutral (Table 4.4), which shows that NE trade winds are less constant and dispersal of vog is more variable. Another important factor is that when La Niña is active (Table 4.3) the NE trade winds are stronger than when El Niño is active and can spread vog across a wider distance.

The decline in NE trade winds can be slightly associated to a shift in the PDO from positive to negative. The PDO is a long-term teleconnection often remaining within a cold or warm mode for 20-30 years and it is fairly different compared to the other studied weather patterns in this thesis because of its prolonged length. Even though this index is not shown to be as significant as other teleconnections, it is known to impact the location of the Pacific jet stream and associated weather patterns.

Table 4.1. Results of Yearly Wind Direction for Hilo and Kona with predominant NE Direction Winds showing their days and percent. Red years showed an active El Niño event while blue years showed an active La Niña event. Light yellow highlights show 50% or more of predominant NE Winds in Kona. Dark yellow highlights show 30% or more of predominant NE Winds in Hilo.

NE TRADE WINDS YEARLY								
	HILO WD1+2		HILO WD5		KONA WD2		KONA WD5	
	Days	Percent	Days	Percent	Days	Percent	Days	Percent
1980	0	0%						
1981	31	8%						
1982	0	0%						
1983	31	8%						
1984	31	8%						
1985	30	8%						
1986	60	16%						
1987	60	16%						
1988	92	25%						
1989	91	25%						
1990	31	8%						
1991	60	16%						
1992	154	42%						
1993	61	17%						
1994	150	41%						
1995	0	0%						
1996	0	0%						
1997	30	8%						
1998	0	0%	30	8%	245	67%		
1999	30	8%	91	25%	182	50%	304	83%
2000	62	17%	60	16%	153	42%	212	58%
2001	58	16%	89	24%	182	50%	151	41%
2002	123	34%	61	17%	181	50%	242	66%
2003	92	25%	121	33%	182	50%	152	42%
2004	61	17%	92	25%	154	42%	123	34%
2005	61	17%	0	0%	210	58%	152	42%
2006	61	17%	124	34%	153	42%	153	42%
2007	92	25%	30	8%	153	42%	214	59%
2008	0	0%	123	34%	215	59%	216	59%
2009	91	25%	30	8%	180	49%	183	50%
2010	92	25%	93	25%	123	34%	61	17%
2011	91	25%	60	16%	153	42%	184	50%
2012	31	8%	61	17%	213	58%	184	50%
2013	30	8%	30	8%	118	32%	179	49%
2014	30	8%	30	8%	123	34%	92	25%
2015	0	0%	30	8%	121	33%	91	25%
2016	90	25%	30	8%	91	25%	122	33%
2017	31	8%	31	8%	122	33%	183	50%
2018	0	0%	0	0%	124	34%	124	34%

Table 4.2. Results of Wind Direction in the active El Niño event years for Hilo and Kona with predominant NE Direction Winds showing their days and percent. Light yellow highlights show 50% or more of predominant NE Winds in Kona. Dark yellow highlights show 30% or more of predominant NE Winds in Hilo.

NE TRADE WINDS YEARLY								
	HILO WD1+2		HILO WD5		KONA WD2		KONA WD5	
	Days	Percent	Days	Percent	Days	Percent	Days	Percent
1980	0	0%						
1983	31	8%						
1987	60	16%						
1988	92	25%						
1992	154	42%						
1995	0	0%						
1998	0	0%	30	8%	245	67%		
2003	92	25%	121	33%	182	50%	152	42%
2007	92	25%	30	8%	153	42%	214	59%
2010	92	25%	93	25%	123	34%	61	17%
2016	90	25%	30	8%	91	25%	122	33%

Table 4.3. Results of Wind Direction in the active La Niña event years for Hilo and Kona with predominant NE Direction Winds showing their days and percent. Light yellow highlights show 50% or more of predominant NE Winds in Kona. Dark yellow highlights show 30% or more of predominant NE Winds in Hilo.

NE TRADE WINDS YEARLY								
	HILO WD1+2		HILO WD5		KONA WD2		KONA WD5	
	Days	Percent	Days	Percent	Days	Percent	Days	Percent
1989	91	25%						
1996	0	0%						
1999	30	8%	91	25%	182	50%	304	83%
2000	62	17%	60	16%	153	42%	212	58%
2008	0	0%	123	34%	215	59%	216	59%
2011	91	25%	60	16%	153	42%	184	50%
2012	31	8%	61	17%	213	58%	184	50%

Table 4.4. Results of Wind Direction in the neutral ENSO years for Hilo and Kona with predominant NE Direction Winds showing their days and percent. Light yellow highlights show 50% or more of predominant NE Winds in Kona. Dark yellow highlights show 30% or more of predominant NE Winds in Hilo.

NE TRADE WINDS YEARLY								
	HILO WD1+2		HILO WD5		KONA WD2		KONA WD5	
	Days	Percent	Days	Percent	Days	Percent	Days	Percent
1981	31	8%						
1982	0	0%						
1984	31	8%						
1985	30	8%						
1986	60	16%						
1990	31	8%						
1991	60	16%						
1993	61	17%						
1994	150	41%						
1997	30	8%						
2001	58	16%	89	24%	182	50%	151	41%
2002	123	34%	61	17%	181	50%	242	66%
2004	61	17%	92	25%	154	42%	123	34%
2005	61	17%	0	0%	210	58%	152	42%
2006	61	17%	124	34%	153	42%	153	42%
2009	91	25%	30	8%	180	49%	183	50%
2013	30	8%	30	8%	118	32%	179	49%
2014	30	8%	30	8%	123	34%	92	25%
2015	0	0%	30	8%	121	33%	91	25%
2017	31	8%	31	8%	122	33%	183	50%
2018	0	0%	0	0%	124	34%	124	34%

Table 4.5. Results of 5-Year Interval Wind Direction for Hilo and Kona with prevailing NE Direction Winds.

NE TRADE WINDS – 5YR INTERVALS										
YEARS	HILO WD1+2		YEARS	HILO WD5		KONA WD2		YEARS	KONA WD5	
	Days	Percent		Days	Percent	Days	Percent		Days	Percent
1980-84	31	8%								
1985-89	121	33%								
1990-94	92	25%								
1995-99	0	0%	1998-99	125	34%	306	84%	1999	304	83%
2000-04	61	17%	2000-04	150	41%	303	83%	2000-04	334	92%
2005-09	91	25%	2005-09	61	17%	334	92%	2005-09	307	84%
2010-14	61	17%	2010-14	122	33%	242	66%	2010-14	273	75%
2015-18	30	8%	2015-18	61	17%	183	50%	2015-18	275	75%

CHAPTER 5. CONCLUSIONS AND FUTURE RESEARCH

The wind variation results for Hawai'i display a difference throughout the years. Specifically, these results just consider the island of Hawai'i compared to previous research (e.g., Garza et al., 2012), which generalizes the region. The results for the weather stations in the east (Hilo) and west (Kona) sides of the island indicate that there has been a reduction in the numbers of days that NE trade winds were experienced. Kona in 1999 had an occurrence average of 243 days per year (67%), but in 2018 it had only a 124 days per year (34%) occurrence. Hilo displayed similar results but with less general dominance by one wind direction; therefore, the occurrence for 1999 had an average of 60 days per year (17%) but for 2018 Hilo experienced 0 days per year (0%) occurrence of NE trade winds, however easterly winds were dominant.

Overall, several outcomes have been identified for the predominant trade winds over Hawaii. In general, the decrease in NE trade winds is visible yearly and in 5-year intervals, however, this decrease is not as substantial when considering only land-based weather stations. The changes in these trends can be attributed to several teleconnections but this research concludes that the ENSO time-series (ONI, Niño 3.4, TNI) and the PNA are the most relevant patterns for these changes. A possible shift of these teleconnections may be the source of decreasing trade winds and the gradual increase of WS over the tropical/central Pacific.

For future research, wind variations above and below the 2 km inversion layer in Hawai'i should be explored more. This would allow researchers to further investigate the dispersion of vog more accurately in relation to different elevations in Hawai'i. The addition of more weather stations throughout the main island, especially in the southern, central, and northern areas, may provide new insights to the wind direction dynamics on the island. Ground weather stations and buoy stations close to the island can be studied separately and then compared to examine trade

wind dominance. Another aspect that would be beneficial to research is cloud cover considering the decrease of NE trade winds and the slight increase of Kona winds this can affect the cloud cover over the islands. Additionally, with the high demand for electricity (more specifically air conditioners) in recent years due to a more humid climate (also related to Kona winds and wind direction changes) residents are opting to install solar panels; and cloud coverage as well as acid rain are factors that need to be kept in mind. The cloud coverage can be studied as well throughout the years to corroborate the change of wind directions over Hawai'i.

REFERENCES

- Allan, R., Nicholls, N., Jones, P., Butterworth, I. (1991). A Further Extension of the Tahiti-Darwin SOI, Early ENSO Events and Darwin Pressure. *Journal of Climate*, 4(7), pp.743-749.
- Barnston, A. and Livezey, R. (1987). Classification, Seasonality and Persistence of Low-Frequency Atmospheric Circulation Patterns. *Monthly Weather Review*, 115(6), pp.1083-1126.
- Burstyn, H. L., (1966). The deflecting force and Coriolis. *Bulletin of the American Meteorological Society*, 47(11), pp.890-891.
- Camara, J. and Lagunzad, J. (2011). Ocular Findings in Volcanic Fog Induced Conjunctivitis. *Hawai'i Medical Journal*, 70(12), pp.262-265.
- Cardone, V. J., Greenwood, J. G., Cane, M., (1990). On Trends in Historical Marine Wind Data. *Journal of Climate*, 3(1), pp.113-127.
- Casanueva-Vicente, A., Rodríguez-Puebla, C., Frías-Domínguez, M., González-Reviriego, N. (2014). Variability of extreme precipitation over Europe and its relationships with teleconnection patterns. *Hydrology and Earth System Sciences*, 18(2), pp.709-725.
- Chen, Y. and Feng, J., 2001. Numerical Simulations of Airflow and Cloud Distributions over the Windward Side of the Island of Hawaii. Part I: The Effects of Trade Wind Inversion*. *Monthly Weather Review*, 129(5), pp.1117-1134.
- Chen, Y., and Nash, A., (1994). Diurnal Variation of Surface Airflow and Rainfall Frequencies on the Island of Hawaii. *Monthly Weather Review*, 122(1), pp.34-56.

- Chiew, F. H. S., Piechota, T. C., Dracup, J. A., McMahon, T. A. (1998). El Nino/Southern Oscillation and Australian rainfall, streamflow and drought: Links and potential for forecasting. *Journal of Hydrology*, 204(1-4), pp.138-149.
- Chow, D., Grandinetti, A., Fernandez, E., Sutton, A., Elias, T., Brooks, B., Tam, E. (2010). Is volcanic air pollution associated with decreased heart-rate variability?. *Heart Asia*, 2(1), pp.36-41.
- Chu, P. and Chen, H. (2005). Interannual and Interdecadal Rainfall Variations in the Hawaiian Islands. *Journal of Climate*, 18(22), pp.4796-4813.
- Daingerfield, L. (1921). KONA STORMS. *Monthly Weather Review*, 49(6), pp.327-329.
- Deser, C., Phillips, A., Tomas, R., Okumura, Y., Alexander, M., Capotondi, A., Scott, J., Kwon, Y., Ohba, M. (2012). ENSO and Pacific Decadal Variability in the Community Climate System Model Version 4. *Journal of Climate*, 25(8), pp.2622-2651.
- Deser, C., Trenberth, K., National Center for Atmospheric Research Staff (Eds). Last modified 06 Jan 2016 (2020). *Pacific Decadal Oscillation (PDO): Definition and Indices* | NCAR - *Climate Data Guide*. [online] climatedataguide.ucar.edu. Available at: <https://climatedataguide.ucar.edu/climate-data/pacific-decadal-oscillation-pdo-definition-and-indices> [Accessed 14 Jan. 2020].
- Elias, T. and Sutton, A. J., (2017). Volcanic air pollution hazards in Hawaii: U.S. Geological Survey Fact Sheet 2017–3017, 4 p.
- Feng, J., and Chen, Y. L., (2001). Numerical Simulations of Airflow and Cloud Distributions over the Windward Side of the Island of Hawaii. Part II: Nocturnal Flow Regime*. *Monthly Weather Review*, 129(5), pp.1135-1147.

- Franzke, C., Feldstein, S. and Lee, S. (2011). Synoptic analysis of the Pacific-North American teleconnection pattern. *Quarterly Journal of the Royal Meteorological Society*, 137(655), pp.329-346.
- Garza, J., Chu, P., Norton, C., Schroeder, T. (2012). Changes of the prevailing trade winds over the islands of Hawaii and the North Pacific. *Journal of Geophysical Research: Atmospheres*, 117(D11), p.n/a-n/a.
- Global Volcanism Program (2013a). Kilauea (332010) in *Volcanoes of the World*, v. 4.8.5. Venzke, E (ed.). Smithsonian Institution. Downloaded 06 Feb 2020 (<https://volcano.si.edu/volcano.cfm?vn=332010>). <https://doi.org/10.5479/si.GVP.VOTW4-2013>
- Global Volcanism Program (2013b). Mauna Kea (332030) in *Volcanoes of the World*, v. 4.8.5. Venzke, E (ed.). Smithsonian Institution. Downloaded 06 Feb 2020 (<https://volcano.si.edu/volcano.cfm?vn=332030>). <https://doi.org/10.5479/si.GVP.VOTW4-2013>
- Global Volcanism Program (2013c). Mauna Loa (332020) in *Volcanoes of the World*, v. 4.8.5. Venzke, E (ed.). Smithsonian Institution. Downloaded 06 Feb 2020 (<https://volcano.si.edu/volcano.cfm?vn=332020>). <https://doi.org/10.5479/si.GVP.VOTW4-2013>
- Global Volcanism Program (2013d). *Volcanoes of the World*, v. 4.8.5. Venzke, E (ed.). Smithsonian Institution. Downloaded 06 Feb 2020. <https://doi.org/10.5479/si.GVP.VOTW4-2013>
- Grimm, A. and Tedeschi, R. (2009). ENSO and Extreme Rainfall Events in South America. *Journal of Climate*, 22(7), pp.1589-1609.

- Halliday, T., Lynham, J., de Paula, Á. (2018). Vog: Using Volcanic Eruptions to Estimate the Health Costs of Particulates. *The Economic Journal*, 129(620), pp.1782-1816.
- Hansen, J. and Mavromatis, T. (2001). Correcting low-frequency variability bias in stochastic weather generators. *Agricultural and Forest Meteorology*, 109(4), pp.297-310.
- Hardy, J. and Henderson, K. (2013). Cold Front Variability in the Southern United States and the Influence of Atmospheric Teleconnection Patterns. *Physical Geography*, 24(2), pp.120-137.
- Herceg Bulić, I. and Kucharski, F. (2011). Delayed ENSO impact on spring precipitation over North/Atlantic European region. *Climate Dynamics*, 38(11-12), pp.2593-2612.
- IBM Corp. Released 2017. IBM SPSS Statistics for Windows, Version 25.0. Armonk, NY: IBM Corp.
- Kauahikaua, J. P. and Tilling, R. I. (2014). Natural Hazards and Risk Reduction in Hawai‘i, in *Characteristics of Hawaiian volcanoes*, edited by Poland, M. P., Takahashi, T. J., Landowski, C. M., pp.398-427, U.S. Geological Survey, Reston, VA.
- Kousky, V. and Higgins, R. (2007). An Alert Classification System for Monitoring and Assessing the ENSO Cycle. *Weather and Forecasting*, 22(2), pp.353-371.
- Leopold, L. B., (1949). The Interaction of Trade Wind and Sea Breeze, Hawaii. *Journal of Meteorology*, 6(5), pp.312-320.
- Longo, B. M., Rossignol, A., Green, J. B. (2008). Cardiorespiratory health effects associated with sulphurous volcanic air pollution. *Public Health*, 122(8), pp.809-820.
- Lyons, C. J., (1899). VOLCANIC ERUPTIONS IN HAWAII. *Monthly Weather Review*, 27(7), pp.298-299.

- Mantua, N. J. and Hare, S. (2002). Pacific-Decadal Oscillation (PDO). *Encyclopedia of global environmental change, 1*, pp.592-594.
- Mantua, N., Hare, S., Zhang, Y., Wallace, J., Francis, R. (1997). A Pacific Interdecadal Climate Oscillation with Impacts on Salmon Production. *Bulletin of the American Meteorological Society*, 78(6), pp.1069-1079.
- Ncdc.noaa.gov. (2020). *Climate Data Online (CDO) - The National Climatic Data Center's (NCDC) Climate Data Online (CDO) provides free access to NCDC's archive of historical weather and climate data in addition to station history information. | National Climatic Data Center (NCDC)*. [online] Available at: <https://www.ncdc.noaa.gov/cdo-web/> [Accessed 3 Feb. 2020].
- Ncdc.noaa.gov. (2020). *Teleconnections | National Centers for Environmental Information (NCEI)*. [online] Available at: <https://www.ncdc.noaa.gov/teleconnections/> [Accessed 6 Jan. 2020].
- Poland, M. P., Takahashi, T. J., Landowski, C. M. (2014). *Characteristics of Hawaiian volcanoes, PP-1801*. Reston, VA: U.S. Geological Survey, p.442.
- Ralph, F., Neiman, P., Kingsmill, D., Persson, P., White, A., Strem, E., Andrews, E., Antweiler, R. (2003). The Impact of a Prominent Rain Shadow on Flooding in California's Santa Cruz Mountains: A CALJET Case Study and Sensitivity to the ENSO Cycle. *Journal of Hydrometeorology*, 4(6), pp.1243-1264.
- Rasmusson, E. and Carpenter, T. (1982). Variations in Tropical Sea Surface Temperature and Surface Wind Fields Associated with the Southern Oscillation/El Niño. *Monthly Weather Review*, 110(5), pp.354-384.

- Rayner, N. A., Parker, D. E., Horton, E. B., Folland, C. K., Alexander, L. V., Rowell, D. P., Kent, E. C., Kaplan, A. (2003). Global analyses of sea surface temperature, sea ice, and night marine air temperature since the late nineteenth century. *Journal of Geophysical Research*, 108(D14).
- Ropelewski, C. and Jones, P. (1987). An Extension of the Tahiti–Darwin Southern Oscillation Index. *Monthly Weather Review*, 115(9), pp.2161-2165.
- Sanderson, M. (1993a). *Prevailing trade winds*. Honolulu: University of Hawaii Press.
- Sanderson, M. (1993b). Introduction, in *Prevailing Trade Winds: Weather and Climate in Hawaii*, edited by M. Sanderson, pp. 1–11, Univ. of Hawai'i Press, Honolulu.
- Schmid, R. (1981). Descriptive nomenclature and classification of pyroclastic deposits and fragments: Recommendations of the IUGS Subcommittee on the Systematics of Igneous Rocks. *Geology*, 9(1), p.41.
- Schroeder, T. A. (1993). Climate controls, in *Prevailing Trade Winds: Weather and Climate in Hawaii*, edited by M. Sanderson, pp. 12–36, Univ. of Hawai'i Press, Honolulu.
- Smith, C. A. and Sardeshmukh, P. (2000). The effect of ENSO on the intraseasonal variance of surface temperatures in winter. *International Journal of Climatology*, 20(13), pp.1543-1557.
- Smith, S., Brolley, J., O'Brien, J., Tartaglione, C. (2007). ENSO's Impact on Regional U.S. Hurricane Activity. *Journal of Climate*, 20(7), pp.1404-1414.
- Statistics.laerd.com. (2020). *How to perform a Multinomial Logistic Regression in SPSS Statistics / Laerd Statistics*. [online] Available at: <https://statistics.laerd.com/spss-tutorials/multinomial-logistic-regression-using-spss-statistics.php> [Accessed 5 Feb. 2020].

- Statistics.laerd.com. (2020). *Linear Regression Analysis in SPSS Statistics - Procedure, assumptions and reporting the output.* [online] Available at:
<https://statistics.laerd.com/spss-tutorials/linear-regression-using-spss-statistics.php>
[Accessed 1 Feb. 2020].
- Sutton, J., Elias, T., Hendley, J. W., Stauffer, P. H., (2000). *Volcanic air pollution: a hazard in Hawaii*: U.S. Geological Survey Fact Sheet 169–97, 2 p.
- Swanson, D., Fiske, D., Rose, T., Houghton, B., Mastin, L., (2011). *Kīlauea—an explosive volcano in Hawai‘i*: U.S. Geological Survey Fact Sheet 2011–3064, 4 p.
- Tedeschi, R., Grimm, A., Cavalcanti, I. (2016). Influence of Central and East ENSO on extreme events of precipitation in South America during austral spring and summer. *International Journal of Climatology*, 35(8), pp.2045-2064.
- Trenberth, K. (1997). The Definition of El Niño. *Bulletin of the American Meteorological Society*, 78(12), pp.2771-2777.
- Trenberth, K. and Stepaniak, D. (2001). Indices of El Niño Evolution. *Journal of Climate*, 14(8), pp.1697-1701.
- Wallace, J. and Gutzler, D. (1981). Teleconnections in the Geopotential Height Field during the Northern Hemisphere Winter. *Monthly Weather Review*, 109(4), pp.784-812.
- Wang, G. and Hendon, H. (2007). Sensitivity of Australian Rainfall to Inter–El Niño Variations. *Journal of Climate*, 20(16), pp.4211-4226.
- Whan, K. and Zwiers, F. (2017). The impact of ENSO and the NAO on extreme winter precipitation in North America in observations and regional climate models. *Climate Dynamics*, 48(5-6), pp.1401-1411.

- Wolter, K. and Timlin, M. S. (1998). Measuring the strength of ENSO events: How does 1997/98 rank? *Weather*, 53(9), pp.315-324.
- Wolter, K., and Timlin, M. S. (1993). Monitoring ENSO in COADS with a seasonally adjusted principal component index. *Proc. of the 17th Climate Diagnostics Workshop*, Norman, OK, NOAA/NMC/CAC, NSSL, Oklahoma Clim. Survey, CIMMS and the School of Meteor., Univ. of Oklahoma; Norman, OK, pp.52-57.
- Wunsch, C. (2002). OCEANOGRAPHY: What Is the Thermohaline Circulation?. *Science*, 298(5596), pp.1179-1181.
- Yang, Y., Chen, Y. and Fujioka, F. (2008). Effects of Trade-Wind Strength and Direction on the Leeward Circulations and Rainfall of the Island of Hawaii. *Monthly Weather Review*, 136(12), pp.4799-4818.
- Zhu, Z. and Li, T. (2016). A New Paradigm for Continental U.S. Summer Rainfall Variability: Asia–North America Teleconnection. *Journal of Climate*, 29(20), pp.7313-7327.

APPENDICES

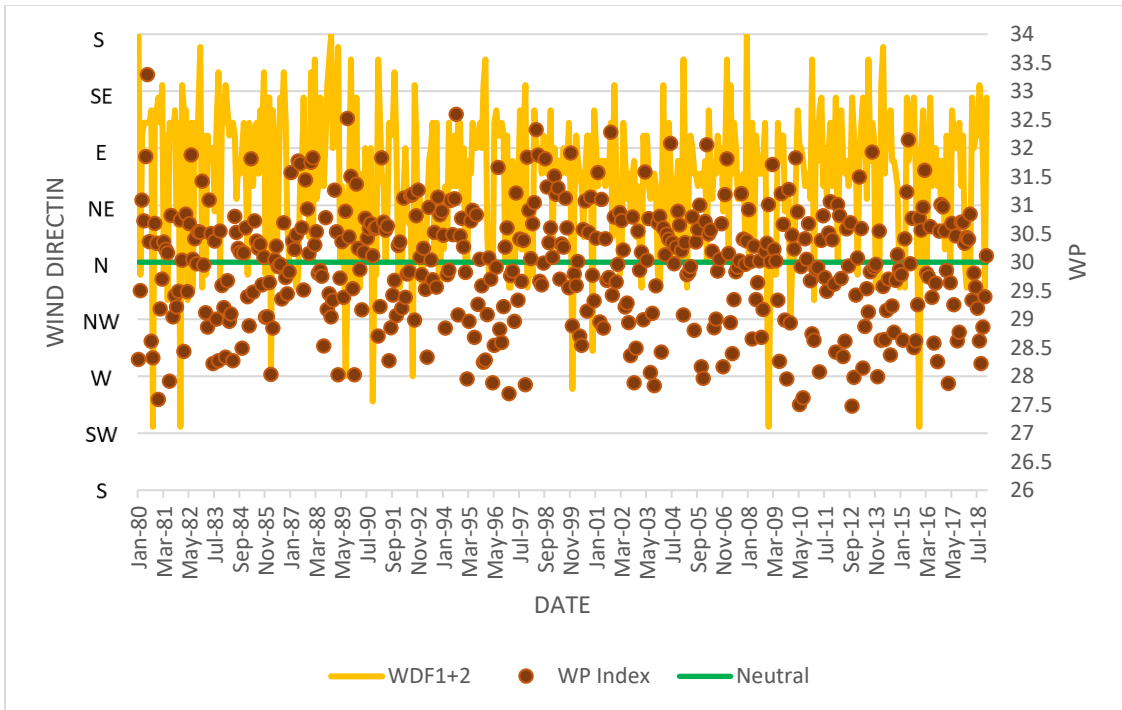
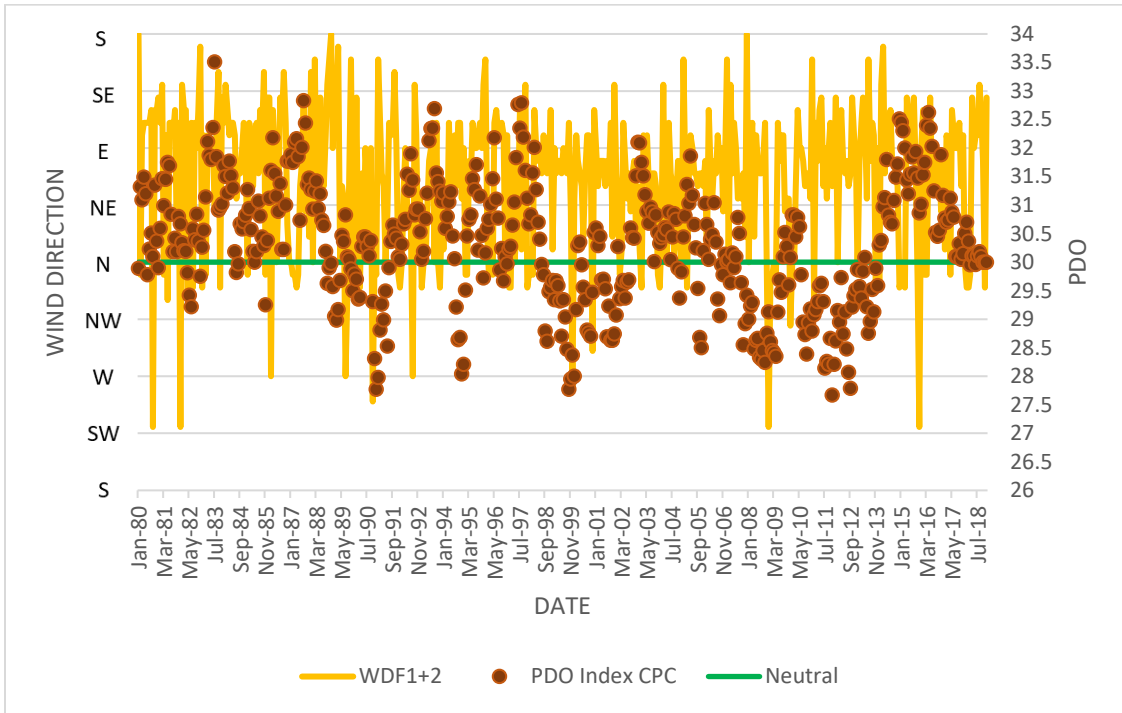
Appendix A: Acronyms

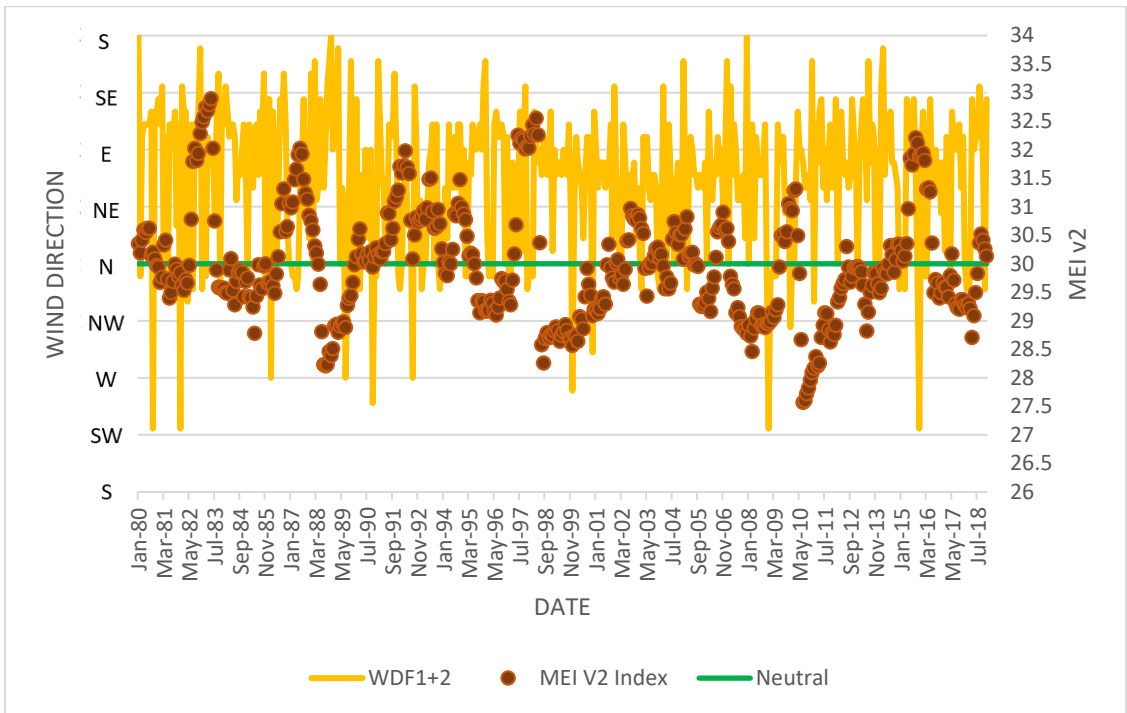
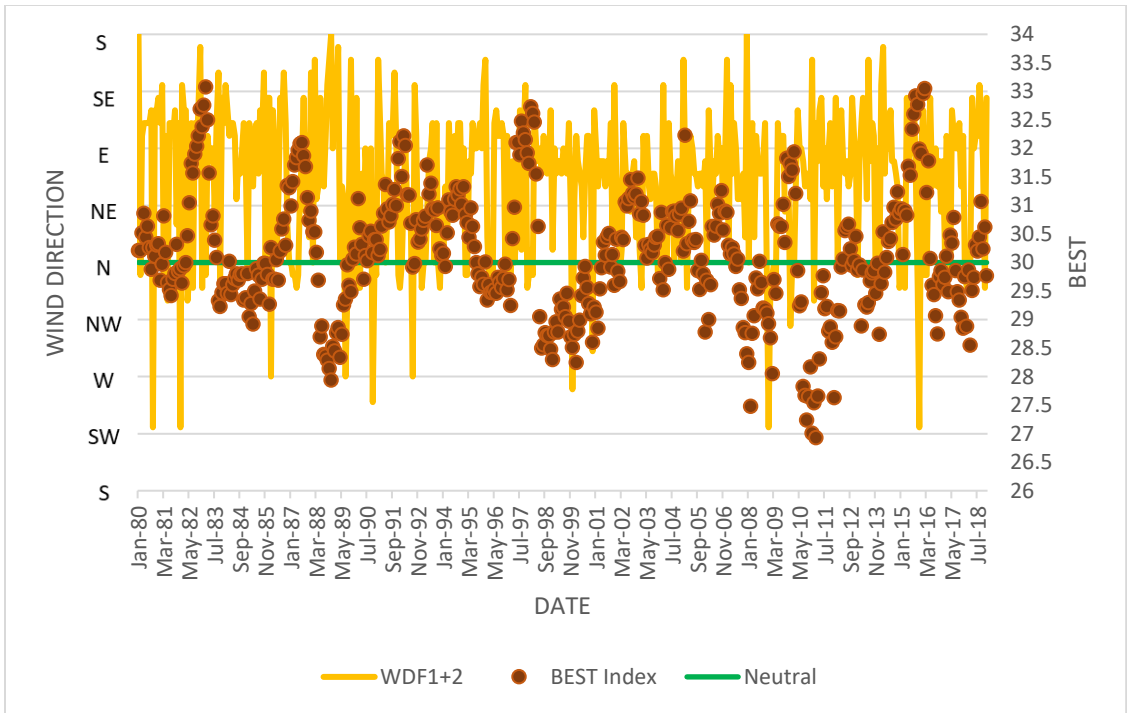
- volcanic fog (vog)
- El Niño-Southern Oscillation (ENSO)
- Pacific Decadal Oscillation (PDO)
- Pacific/North American (PNA)
- West Pacific (WP)
- International Comprehensive Ocean-Atmosphere Data Set (ICOADS)
- National Center for Environmental Prediction (NCEP)
- National Center of Atmospheric Research (NCAR)
- Reanalysis 1 (R1)
- sea surface temperature (SST)
- Hadley Center sea ice and sea surface temperature (HadISST)
- National Oceanic and Atmospheric Administration (NOAA)
- Physical Science Division (PSD)
- Climate Prediction Center (CPC)
- Southern Oscillation Index (SOI)
- Hadley Center sea ice and sea surface temperature version 1 (HadISST1)
- East Central Tropical Pacific SST (Niño3.4)
- Central Tropical Pacific SST (Niño4)
- Transitional “Trans” Niño Index (TNI)
- Oceanic Niño Index (ONI)
- Optimum Interpolation (OI)
- Bivariate ENSO Time-series (BEST)
- Multivariate ENSO Index Version 2 (MEI v2)
- sea-level pressure (SLP)
- surface zonal winds (U)
- meridional winds (V)
- Outgoing Longwave Radiation (OLR)
- Comprehensive Ocean-Atmosphere Data Set (COADS)
- Rotated Principal Component Analysis (RCPA)
- North Atlantic Oscillation (NAO)
- millibar (mb)
- Climate Data Assimilation System (CDAS)
- Northeast (NE)
- Southeast (SE)
- knots (kn)
- miles per hour (mph)
- meters per second (m s^{-1})

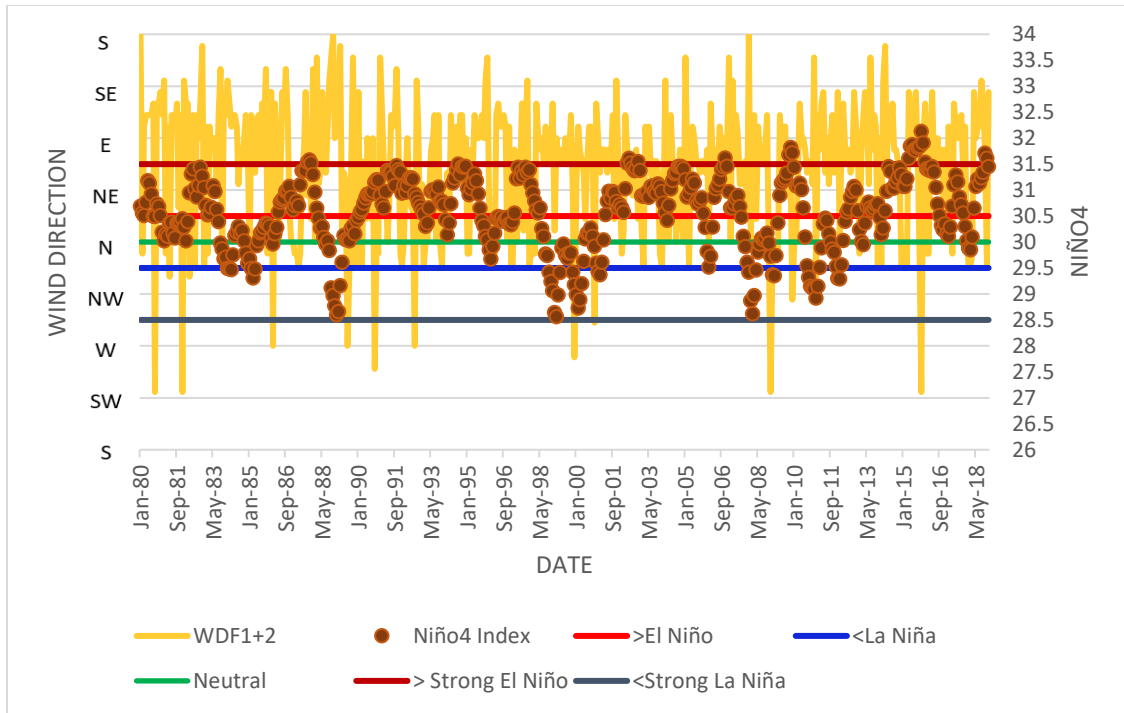
- above sea level (ASL)
- kilometer (km)
- feet (ft)
- meters (m)
- millimeters (mm)
- micrometers (μm)
- particulate matter (PM)
- water vapor (H_2O)
- carbon dioxide (CO_2)
- sulphur dioxide (SO_2)
- Climate Data Online (CDO)
- Global Summary of the Month (GSOM)
- wind speed (WS)
- wind direction (WD)
- mean sea level (MSL)
- wind speed 1 minute (WS1)
- wind direction 1 minute (WD1)
- wind speed 2 minutes (WS2)
- wind direction 2 minutes (WD2)
- wind speed 5 seconds (WS5)
- wind direction 5 seconds (WD5)
- Celsius ($^{\circ}\text{C}$)
- Statistical Product and Service Solutions (SPSS)
- Ordinary Least Square (OLS) Regression
- Multinomial Logistic Regression (MLR)
- R-square (R^2)

Appendix B: Supplemental Figures

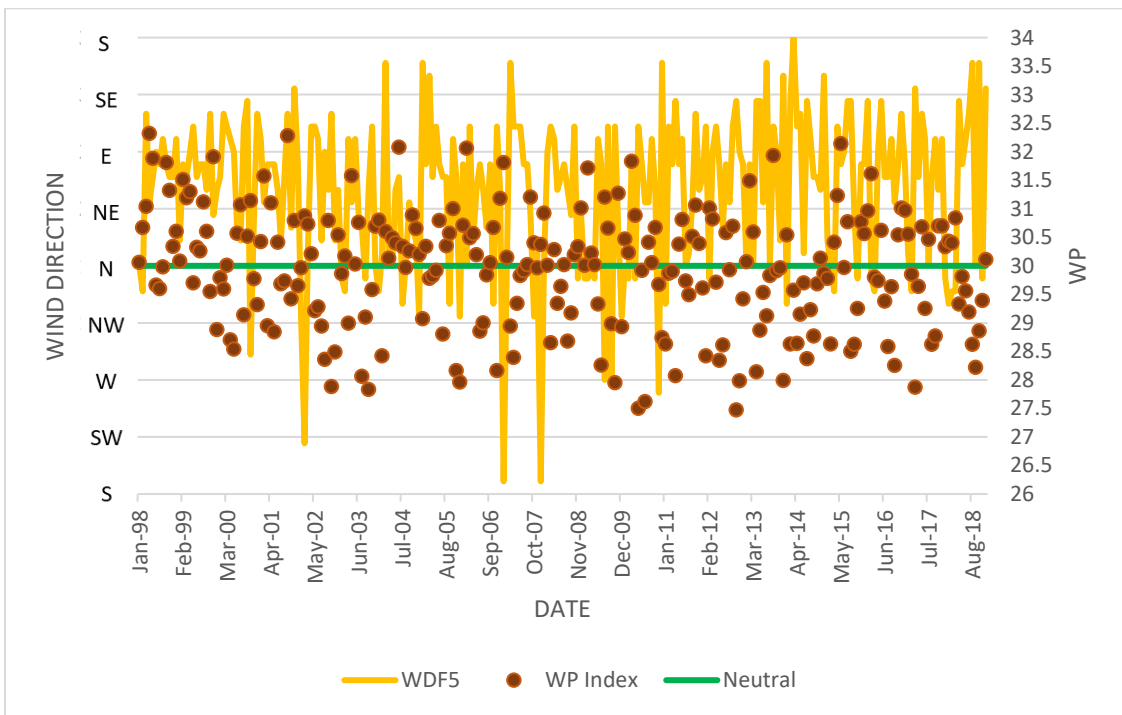
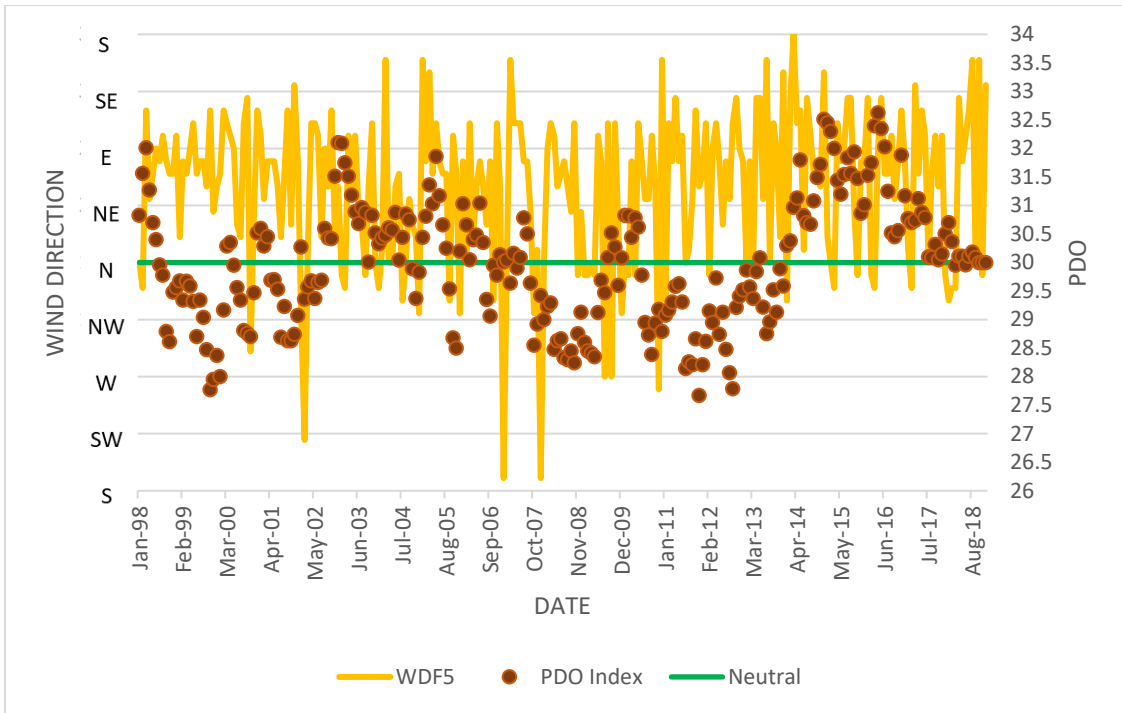
HILO WD1+2

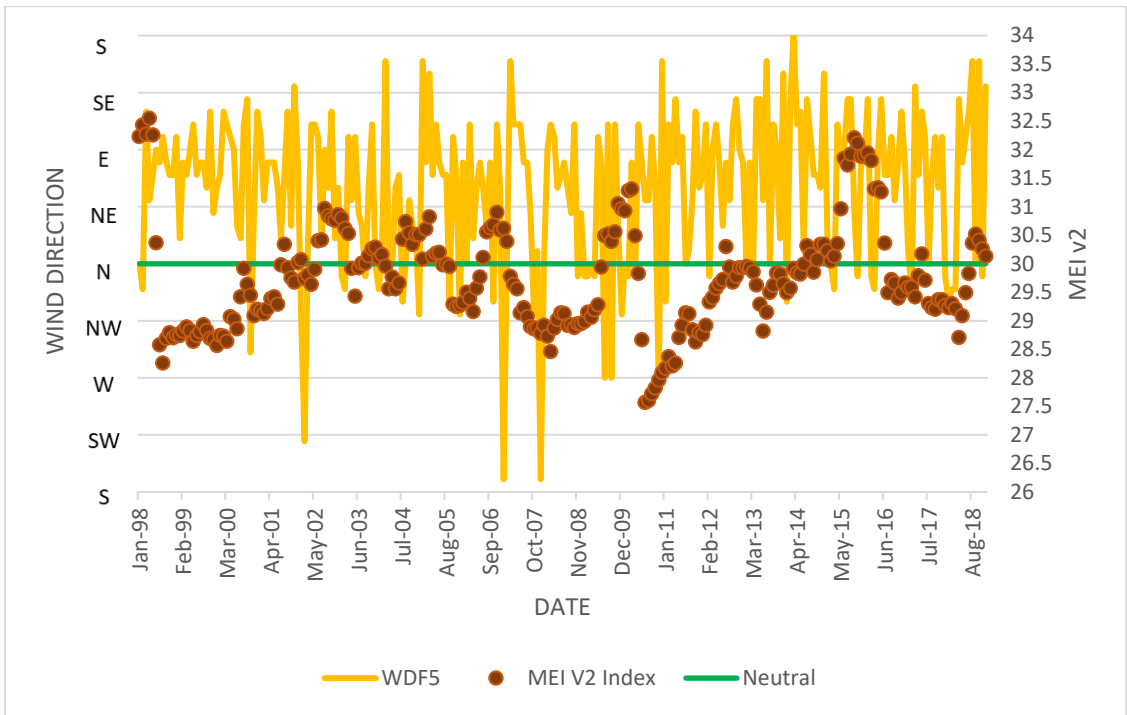
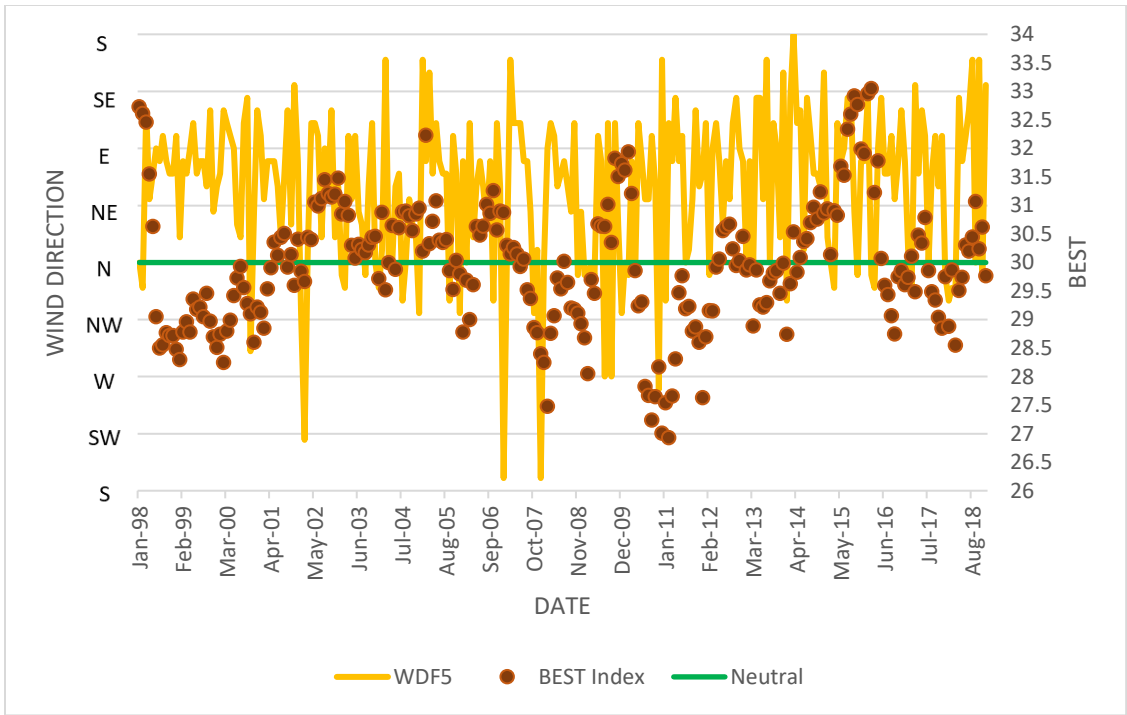


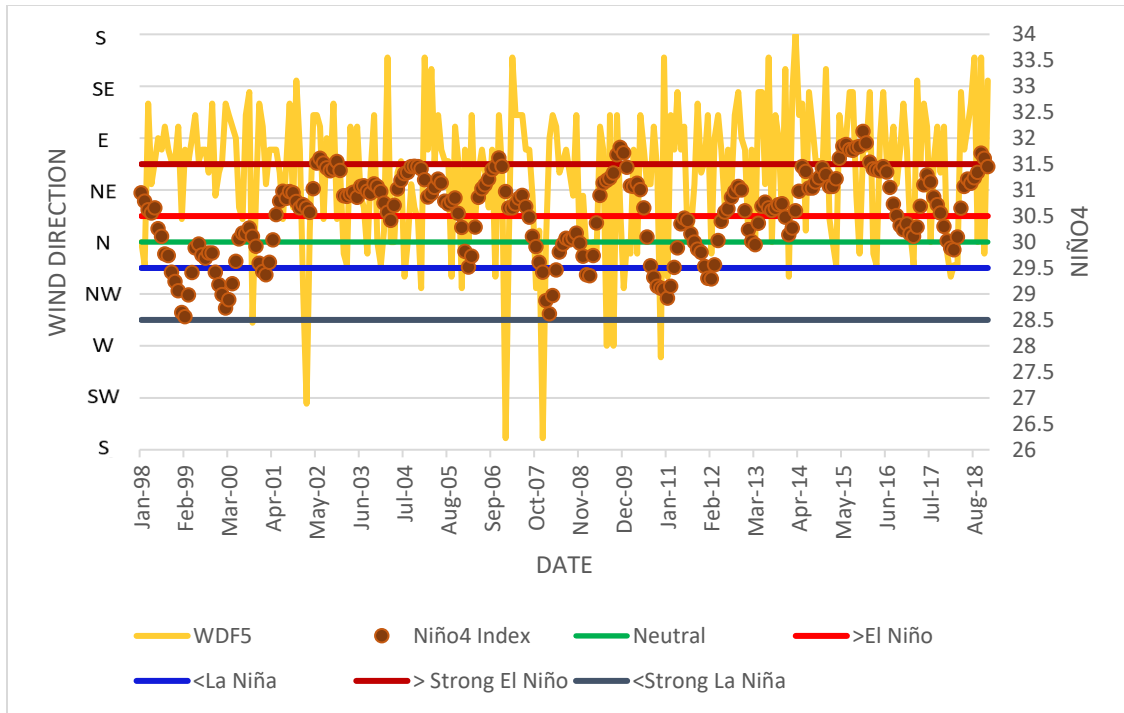




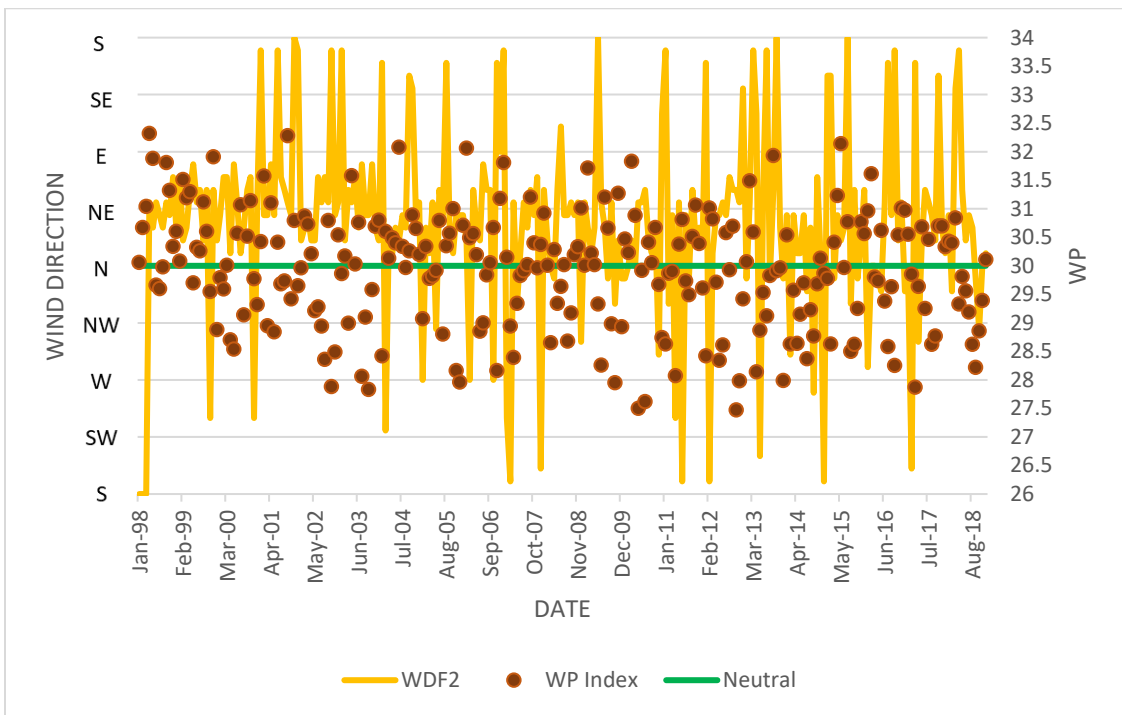
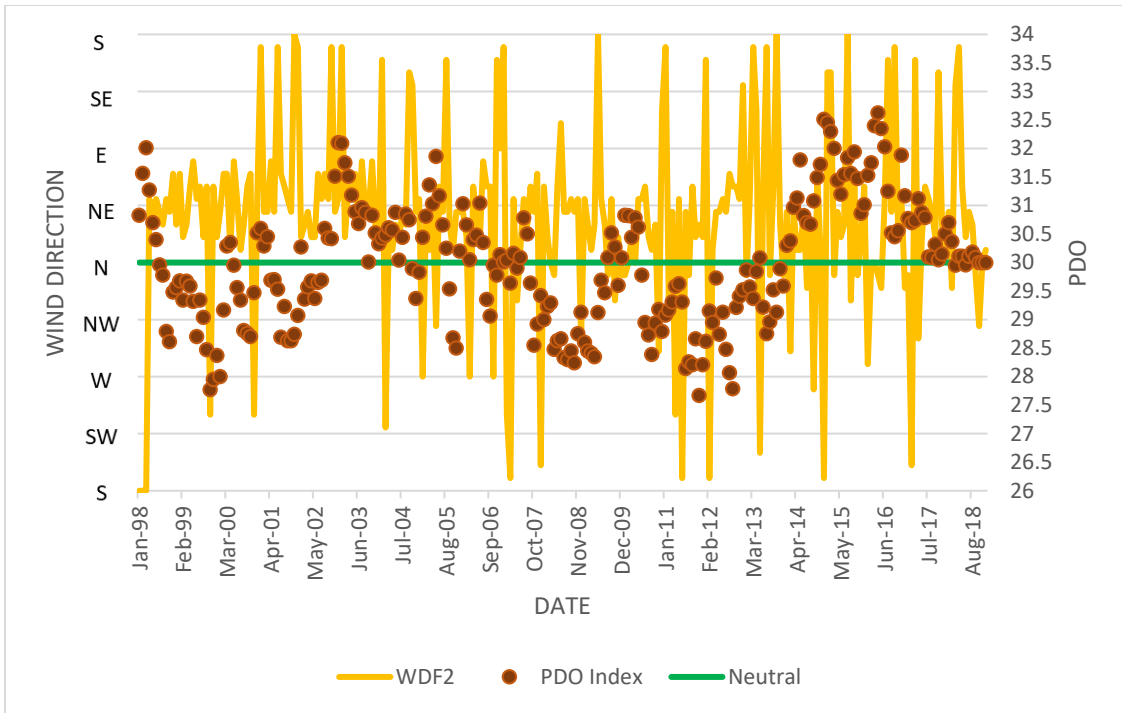
HILO WD5

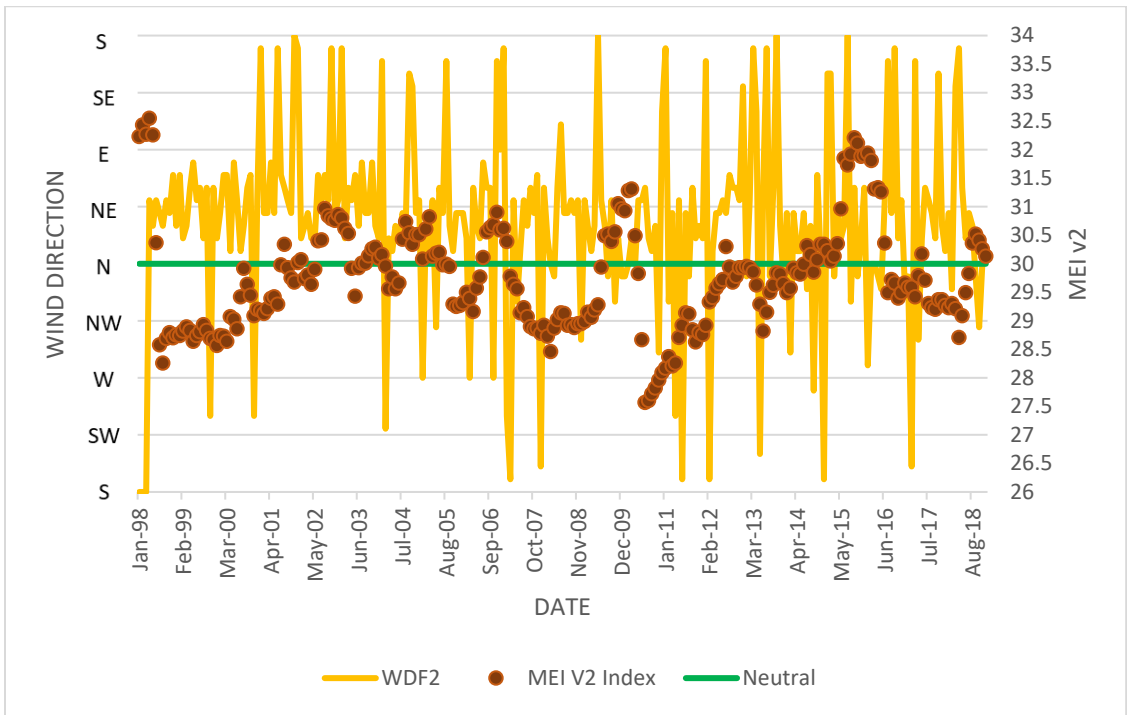
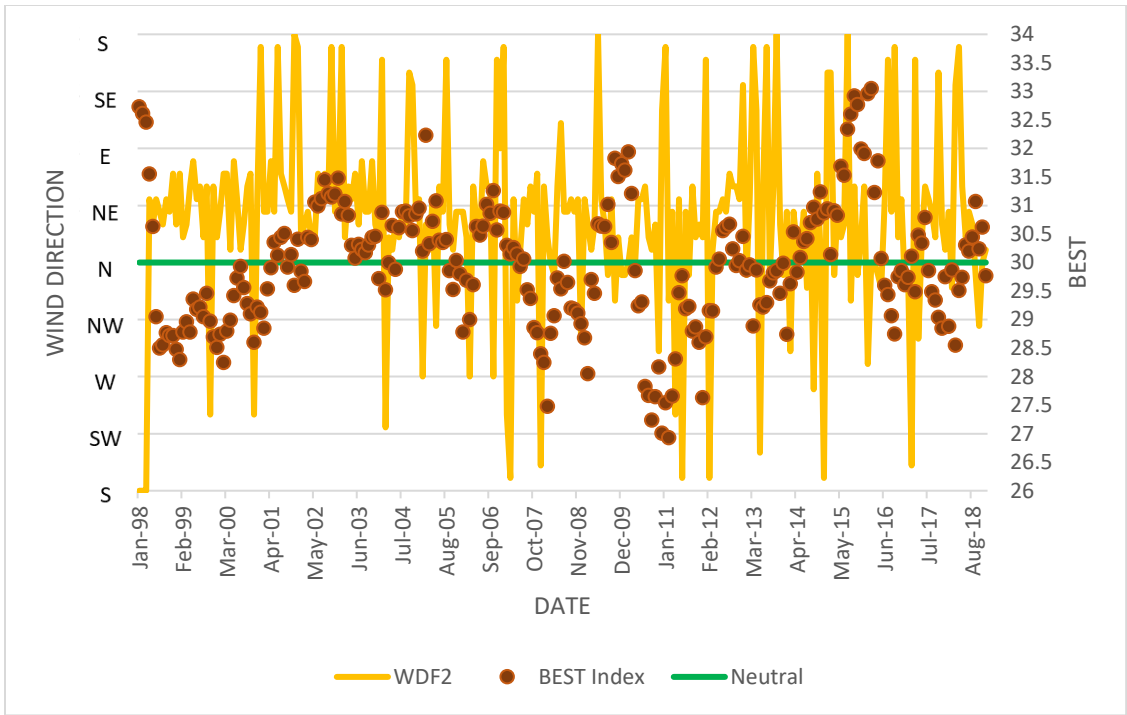


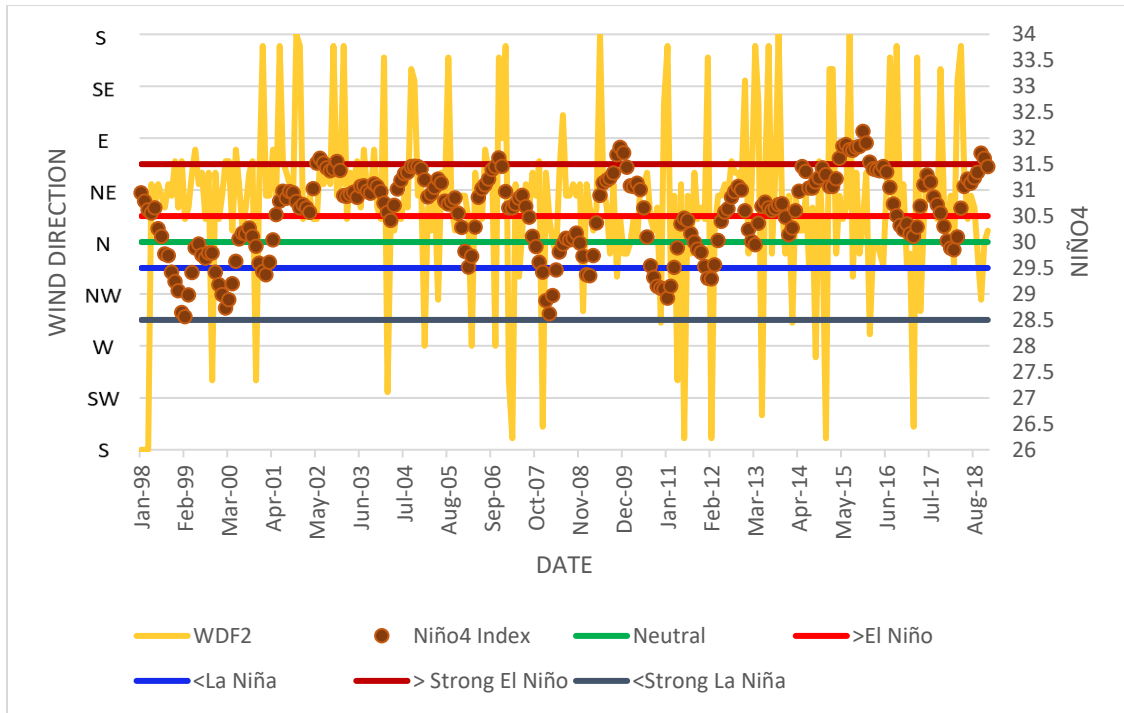




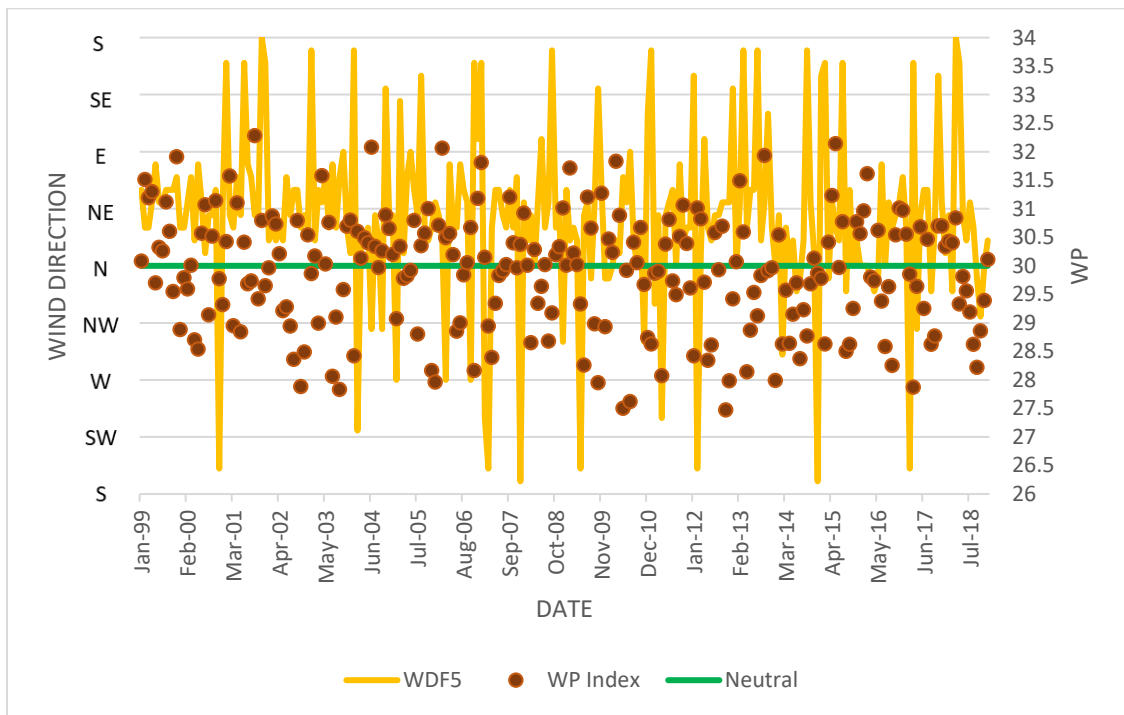
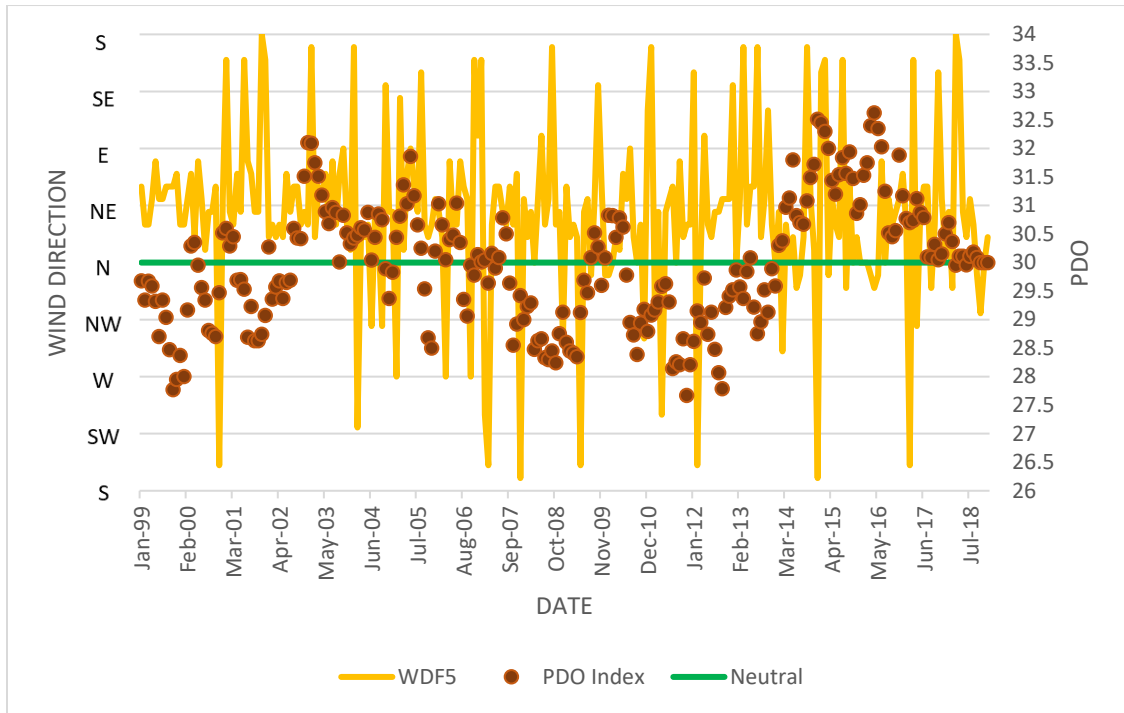
KONA WD2

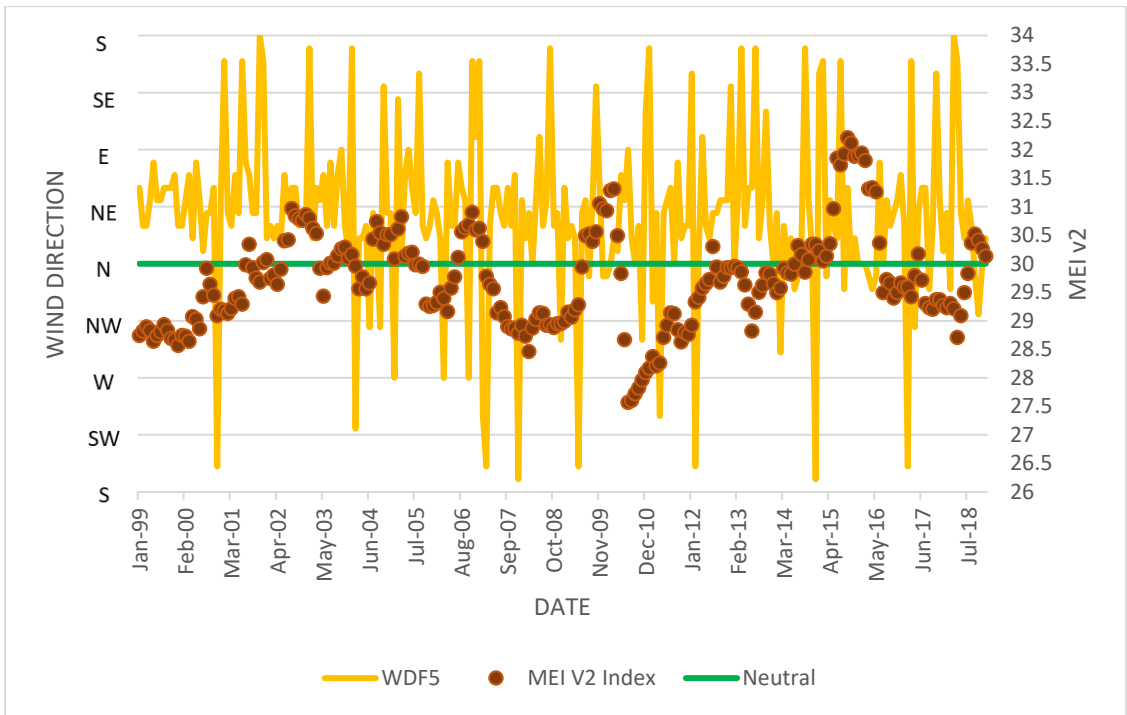
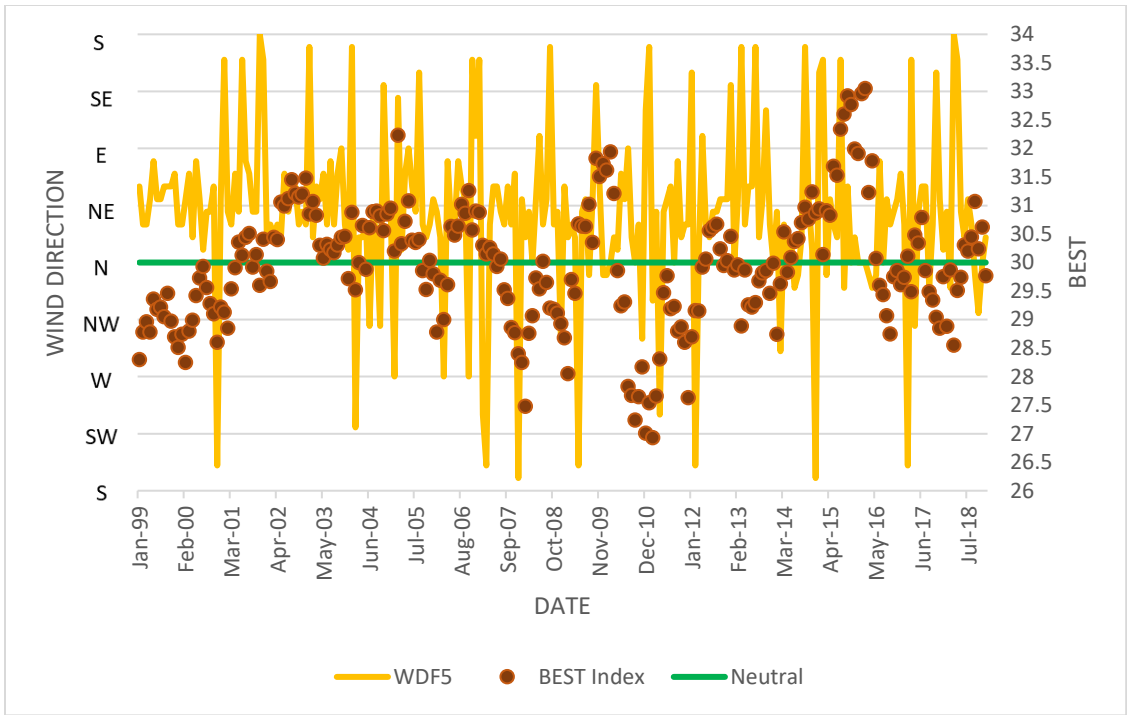


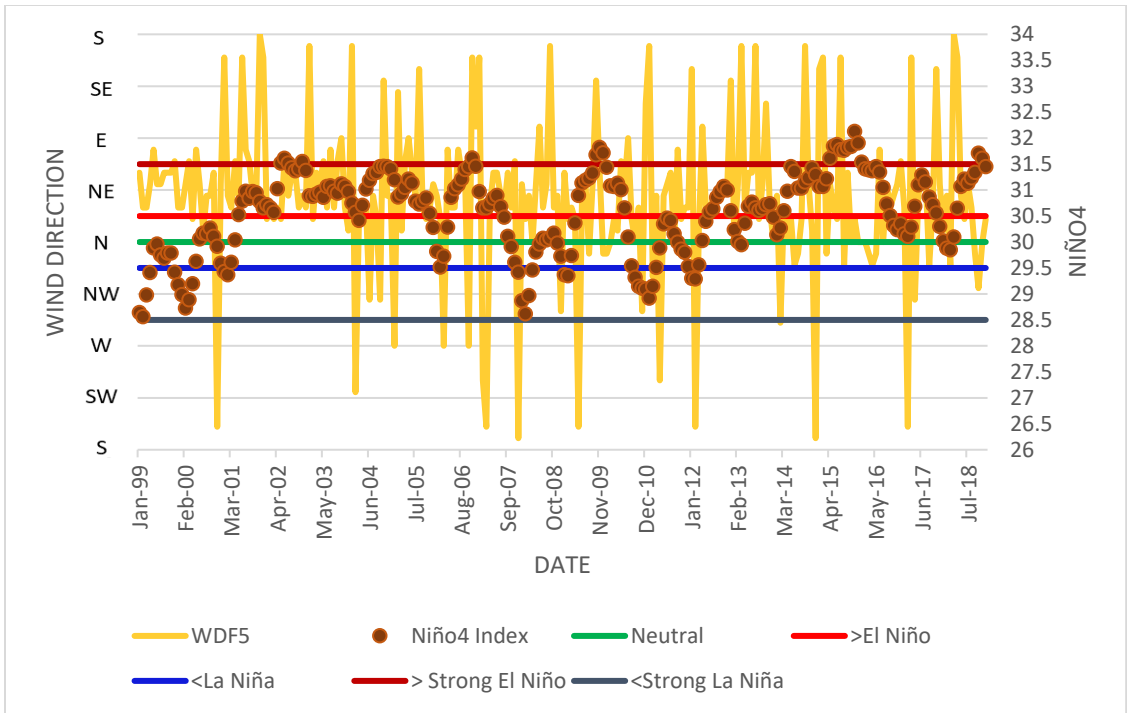




KONA WD5







VITA

MÓNICA Y. AYALA DÍAZ

- Education: M.S. Geosciences, East Tennessee State University, Johnson
City, Tennessee, May 2020
- B.A. Geology, University of Puerto Rico, Campus Mayagüez, PR,
USA, July 2017
- Highschool Diploma, Academia Santa Teresita, Naranjito, PR,
USA, May 2011
- Professional Experience: Graduate Assistant, East Tennessee State University, College of
Arts and Sciences, August 2018- May 2020
- GIS Specialist, East Tennessee State University, Facilities
Management, August 2019- May 2020
- GIS HelpDesk Manager, East Tennessee State University,
Department of Geosciences, August 2019- May 2020